Kinetics and mechanisms of alcohol dehydration on metal oxide catalysts

A DISSERTATION

SUBMITTED TO THE FACULTY OF

UNIVERSITY OF MINNESOTA

BY

Minje Kang

IN PARTIAL FULFILLMENT OF THE REQUIREMENTS

FOR THE DEGREE OF

DOCTOR OF PHILOSOPHY

Advisor : Aditya Bhan

December 2016

Acknowledgements

First of all, I want to show my gratitude to my advisor, Aditya Bhan. I really appreciate his careful advice, patience, and rigorous training. He has led me to explore the tremendous world of science thoroughly and critically. I thank Dr. Joseph DeWilde for his huge helps. Discussions we had guide me to investigate important studies. Other current and former Bhan group members have given a lot of supports to me: Dr. Cha-Jung Chen, Dr. Rachit Khare, Mark Sullivan, Udit Gupta, Andrew Hwang, Anurag Kumar, Linh Bui, Sukaran Arora, Jake Miller, Brandon Foley, Dr. Mark Bachrach, Dr. Praveen Bollini, Dr. Jeremy Bedard, Dr. Do-Young Hong, Dr. Wen-Sheng Lee, Dr. Hsu Chiang, Dr. Ian Hill, Dr. Srinivas Rangarajan, Dr. Elizabeth Mallon, Dr. Samia Ilias, Dr. Dario Prieto-Centurion, Dr. Mark Mazar, Dr. Samuel Blass, and Dr. Dongxia Liu. I would not be able to go through PhD course without them.

I also appreciate devoted supports from my parents in Korea, Koo Hong Kang and Eun-Sik Shin. They have always inspired courage in me to endure difficulties and solve problems. I thank other relatives in Korea who preyed for me. My friends in US and Korea give me a lot of joy. Their careful hands balance my tough graduate school life.

I really have enjoyed my five years at the CEMS department in the University of Minnesota – Twin Cities. The department has provided stable environments for me to focus on studying. I will not forget the time I spent in Minneapolis.

Abstract

Alcohol dehydration on metal oxide catalysts produces valuable chemicals, olefins and ethers. The surface characteristics of the metal oxide formulation under reaction environments are important to understand the versatile deoxygenation, dehydrogenation, and carbon-chain growth reactions that occur in parallel. In this dissertation, I studied the kinetics, mechanisms, and site requirements of alcohol dehydration on metal oxides including alumina polymorphs (alpha, gamma, and eta), zirconia, and chlorinated alumina, to probe the evolution and function of these metal oxides under reaction environments.

Steady state rates of ether formation from alcohols (1-propanol, 2-propanol, and isobutanol) on γ-Al_2O_3 at 488 K increase at low alcohol pressure (0.1-4.2 kPa) but asymptotically converge to different values, inversely proportional to water pressure, at high alcohol pressure (4.2-7.2 kPa). This observed inhibition of etherification rates for C_2-C_4 alcohols on γ-Al_2O_3 by water is mechanistically explained by the presence of surface mutlimers composed of two alcohol molecules and one water molecule under reaction conditions. Mono-alcohol dehydration of C_3-C_4 alcohols follows the same mechanism as that for ethanol and involves inhibition by dimers. The amount of adsorbed pyridine estimated by in-situ titration to completely inhibit ether formation on γ-Al_2O_3 shows that the number of sites available for di-alcohol dehydration reactions is the same for different alcohols, irrespective of the carbon chain length and substitution. 2-Propanol has the highest rate constant for mono-alcohol dehydration among studied alcohols, demonstrating that stability of the carbocation-like transition state is the primary factor in determining rates of mono-alcohol dehydration which concomitantly results in high selectivity to the olefin. 1-Propanol and isobutanol have higher olefin formation rate constants than ethanol indicating that olefin formation is also affected by carbon chain length. Isobutanol has the lowest rate constant for di-alcohol dehydration because of steric factors.

The steady state rates of ethene and diethyl ether formation in parallel ethanol dehydration reactions at 573 and 623 K are mechanistically and kinetically described by the same rate expression on different alumina materials (α-, γ-, and η-Al_2O_3), implying that

alumina materials have similar surface sites under reaction environments. In-situ chemical titration using pyridine as a titrant elucidates similar site densities (~0.12 sites nm^{-2} and ~0.07 sites nm^{-2} for ethene formation and ~0.14 sites nm^{-2} and ~0.09 sites nm^{-2} for diethyl ether formation on γ- and η-Al_2O_3, respectively) on γ- and η-Al_2O_3 indicating that similar surface features exist on both γ- and η-Al_2O_3. Pyridine-ethanol co-feed experiments show that pyridine inhibited the formation of ethene to a greater extent than diethyl ether suggesting that the two parallel dehydration reactions are not catalyzed by a common active site.

The mechanisms and rate expressions that describe the kinetics of mono- and di-alcohol dehydration by alumina polymorphs are also valid for other solid acid catalysts such as ZrO_2 and Cl-Al_2O_3. A comparison of the rates (per g) for alumina polymorphs, ZrO_2, and Cl-Al_2O_3 reveals that rates are lower for ZrO_2 and higher for Cl-Al_2O_3. ZrO_2 formulations show ~50% carbon selectivity to ethene at 573 K with 2.2 kPa of ethanol and 1.1 kPa of water partial pressure while the selectivity to ethene at these process conditions on γ-Al_2O_3 is ~30%. Chlorinated alumina and γ-Al_2O_3 show same selectivity to ethene at 488 K when water pressure is negligible.

Table of Contents

List of Tables

List of Figures

List of Schemes

1. Introduction

1.1. Motivation and background

Metal oxides are commonly used as catalysts and catalyst supports for condensation, dehydration, dehydrogenation, hydroprocessing, and oxidation reactions of petroleum-derived and oxygen-containing hydrocarbons due to their thermal stability and their acid -basic and redox characteristics[1–12]. The surface structure, coordination of surface atoms, and chemical composition impart this functionality and stability to metal oxides[3]. An understanding of how metal oxides catalyze reactions that selectively activate C-C, C-H, and C-O bonds requires us to investigate their surface properties. Spectroscopic studies, ultra-high vacuum surface studies, and computational-chemistry of specific reactions have been done to elucidate the surface properties of metal oxides[13]. In most cases however, these studies are done at temperature and pressure conditions that are not prevalent during steady state catalysis. I investigated surface properties of metal oxides - alumina and zirconia - using alcohol dehydration as a probe reaction to probe the surface properties of these oxides under reaction environments.

Alcohol dehydration occurs via two parallel pathways - mono-alcohol dehydration producing olefins and di-alcohol dehydration producing ethers - and both pathways result in water as a byproduct. Olefins, which are used as building blocks for polymers, and ethers, which are used as solvents and fuels, are valuable chemicals[14–17]. Alcohols are recently available from biomass resources as well as fossil fuels, so alcohol dehydration

produces high value products from low value reactants[15].

The surface characteristics of oxidic catalysts such as alumina and zirconia depend on reaction environments necessitating their investigation under conditions prevalent during reaction. For example, the number of hydroxyl groups on the surface of γ-Al_2O_3 changes depending on temperature and/or the presence of water in the reaction environment[18–20]. Mechanistic and chemical titration studies described in this research allow us to study surface properties of these oxides under reaction environments.

Previous studies reported that metal oxides catalyze alcohol dehydration reaction via acid-mediated pathways[21–28]. In this work, I detail the kinetics, mechanism, and site requirements of alcohol dehydration on different alumina polymorphs and on amphoteric zirconia. Rate expressions that describe the observed dependence of reaction rates on the partial pressure of alcohol and water are presented and rate and equilibrium parameters in these rate expressions are evaluated using Bayesian-statistics-based parameter estimation methods to fit experimental data at different temperatures (488-623 K) and pressures (0.08-23 kPa for alcohol and 0.31-2.3 kPa for water). The mechanisms of alcohol dehydration reactions were inferred from dominant surface species represented in rate expressions and kinetic isotope effects with deuterated alcohol reactants. In-situ chemical titration methods were employed to investigate the site requirements of alcohol dehydration on metal oxides. The effects of carbon chain length and substitution of reactant C_2-C_4 alcohols on alcohol dehydration on γ-Al_2O_3 are reported in Chapter 2. Chapter 3 discusses the consequences of alumina morphology/topology on the rate and selectivity of parallel ethanol dehydration reactions. The kinetics, mechanism, and site requirements of ethanol dehydration on

zirconia are reported in Chapter 4. Chapter 5 deals with the effects of surface dopants on metal-oxide-mediated dehydration pathways, specifically, Cl-Al_2O_3.

2. Kinetics and mechanism of alcohol dehydration on gamma-alumina: Effects of carbon chain length and substitution*

2.1. Introduction

Gamma-alumina (γ-Al_2O_3) is a widely used heterogeneous catalyst and catalyst support because of its thermal stability and high surface area[5,9,29,30]. Infrared (IR) and nuclear magnetic resonance (NMR) spectroscopic studies have implicated the existence of Lewis acid sites on γ-Al_2O_3 and their involvement in catalysis[21,31,32]. Temperature programmed desorption (TPD) of 2-propanamine on γ-Al_2O_3 resulted in the amine desorbing molecularly intact and not fragmenting to form ammonia and propene, demonstrating that Brønsted acid sites are not present on the γ-Al_2O_3 surface[33]. Periodic density functional theory (DFT) calculations using a PW91 functional and projected augment wave (PAW) methods also show that Lewis acid sites on γ-Al_2O_3(100) adsorb ethanol and water stronger than surface hydroxyl groups[34].

Early work from Knözinger and Ratnasamy[35] presented structural models for surface structure and site configurations on γ-Al_2O_3 which has subsequently been refined on the basis of more recent computational chemistry studies to elucidate a variety of coordination and hydration states for surface alumina[19,36]. Experimental studies from Wischert et al.[37] also note that thermal treatment of γ-Al_2O_3 resulted in a change in the adsorption energy of N_2 and in the observed activation energy of σ-bonds in H_2 and CH_4 and attribute this to

a change in the speciation and number of hydroxyl groups on the alumina surface. The implications of this diversity in coordination and hydration of surface species for catalysis are two-fold, (i) it is likely that under catalytic conditions only a fraction of these Al centers are involved[38–41], and (ii) parallel reactions may be catalyzed by distinct Al centers. We demonstrate in this research that active sites for mono-alcohol and di-alcohol dehydration of C_2-C_4 alcohols are distinct; however, our studies do not probe the structure of the active sites involved.

Knözinger and coworkers[21,42] proposed an E2 type mechanism for uni-alcohol dehydration on γ-Al_2O_3 that involves concurrent cleavage of C_α-O and C_β-H bonds based on the observed kinetic isotope effect (KIE). For di-alcohol dehydration to form ethers, these authors proposed an S_N2 type mechanism involving the reaction of a surface-absorbed alcohol with a surface bound alkoxide intermediate[43]. Shi and Davis[44] investigated ether formation kinetics on γ-Al_2O_3 at 493 K using 84% S-(+)/16% R-(-) 2-butanol and observed that the enantiomer ratio of the ether product was 13% of (R,R), 13% of (S,S), and 74% of (S,R), demonstrating that di-alcohol dehydration occurs via an S_N2 pathway. Christiansen et al.[34] in their periodic DFT study of ethanol dehydration on γ-Al_2O_3(100) calculated a lower energy barrier for E2 and S_N2 type mechanisms in comparison with E1 and sequential pathways for mono- and di-alcohol dehydration, respectively. The mechanistic role of water involves not only the change in coordination/hydration of surface species that consequently results in a change in the number of active centers, but also a kinetic role in inhibiting measured rates of dehydration.

An empirical description postulating rates of dehydration to vary with $\propto \frac{P_{Alcohol}^{1/2}}{P_{Alcohol}^{1/2} + b\, P_{Water}}$ was proposed by Knözinger et al.[45], however, the underlying mechanistic basis for this empirical equation remains unclear. Our submission provides a mechanistic basis for the inhibition of observed rates by water and ascribes it to the involvement of dimeric and trimeric surface adsorbate complexes at these low temperatures. The mechanisms that we present are shown to describe the observed pressure dependences of rate for mono- and di-alcohol dehydration of ethanol, 1-propanol, 2-propanol, and isobutanol at varying alcohol and water pressures. The resulting rate expressions provide a quantitative assessment of rate and equilibrium parameters involved and from this description we infer the role of carbon chain length and substitution in determining selectivity and rates for mono- and di-alcohol dehydration pathways. The first part of this paper reports the similarity of the kinetics and mechanism of parallel mono- and di-alcohol dehydration C_3-C_4 alcohol dehydration to ethanol dehydration. The subsequent discussion compares the assessed rate and equilibrium parameters for different alcohols to show the effects of carbon chain length and substitution on the kinetics of mono- and di-alcohol dehydration dehydration.

2.2. Materials and methods

2.2.1. Catalyst preparation

γ-Al_2O_3 powder (Sasol Catalox 18 HPA-150, BET surface area 141 $m^2\ g^{-1}$, pore volume 0.790 $cm^3\ g^{-1}$) was pressed and sieved to obtain catalyst particles between 180 and 425 μm (40-80 mesh). The reactor bed was formed by mixing the catalyst (0.01-0.2 g) and acid-washed (1 M HNO_3) quartz sand (1.0-1.1 g, 152-422 μm particle size, Acros

Organics). The reactor bed was heated while flowing dry air (1.67 cm^3 s^{-1} at NTP conditions, Ind. Grade, Matheson Trigas) from ambient temperature to 723 K at 0.0148 K s^{-1} and held at 723 K for 4 h. The bed was subsequently cooled to the reaction temperature (488 K) in flowing dry air (1.67 cm^3 s^{-1}). The catalyst was pretreated before reaction in 2.2 kPa of deionized water diluted with the carrier gas, helium (1.7 cm^3 s^{-1} at NTP conditions, Grade 4.7, Minneapolis Oxygen Company), for 1 h. The bed was regenerated after kinetic experiments using the same procedure as above to remove any remaining alcohol and water in the bed.

2.2.2. Steady state kinetic measurements of alcohol dehydration on γ-Al_2O_3

Steady state dehydration reactions were carried out in a quartz tube packed bed reactor (10mm inner diameter) under atmospheric pressure and differential conversion conditions (< 10%). A type K thermocouple located on the external surface of the reactor was used to measure the bed temperature, which was retained at reaction temperature (488 K) using a tube furnace (National Electric Furnace FA120 type) and a Watlow temperature controller (96 series).

Liquid pyridine (>99%, Sigma-Aldrich), 1-propanol (≥99.9%, Sigma-Aldrich, 1-PrOH), 1-propanol-OD (99 at.% D, Isotec Inc.), 1-propanol-d_8 (98 at.% D, Sigma-Aldrich), 2-propanol (≥99.5%, Mallinckrodt Chemicals, 2-PrOH), 2-propanol-d_8 (99.5 at.% D, Aldrich), 2-propanol-OD (98 at.% D, Aldrich), isobutanol (99.9%, Fisher Scientific, iBuOH), isobutanol-d_9 (C_4D_9OH, 99 at.% D, C/D/N Isotopes Inc.), isobutanol-OD (99.1 at.% D, C/D/N Isotopes Inc.), deuterium oxide (99.9 at.% D, Cambridge Isotope

Laboratories, Inc., D_2O), and deionized water components were introduced to heated reactant transfer lines using two separate infusion syringe pumps (KD scientific, KDS100). Alcohol and water mixtures were vaporized at 393 K into a stream of He (1.7-3.2 $cm^3\ s^{-1}$ at NTP conditions) and an internal standard mixture for analysis comprising of Ar/CH_4 (10.0% CH_4 and Ar balance, 0.017 $cm^3\ s^{-1}$ at NTP conditions, Minneapolis oxygen). Partial pressures of components in the feed ($P_{pyridine}$ = 0.02-0.05 kPa, $P_{alcohol}$ = 0.08-7.2 kPa, P_{water} = 0.31-2.2 kPa) were controlled by changing the syringe pump flow rates. Gas lines were resistively heated to maintain temperatures above 343 K and avoid condensation. The reactor effluent was connected via heated transfer lines to an online mass spectrometer (MKS Cirrus 200 Quadrupole) and a gas chromatograph (Agilent 6890 N, GC) which was used for all chemical analysis. The GC was equipped with a methyl-siloxane capillary column (Agilent HP-5, 50.0 m x 320 μm x 0.52 μm) to separate gaseous species before detection with a flame ionization detector and a packed column (SUPELCO HAYESEP R 80/100 mesh packed column, 12 ft) before a thermal conductivity detector. Error bars reported in figures below represent 95% confidence intervals using successive GC injections under the same experimental conditions.

2.2.3. In-situ pyridine titration of catalytic ether formation sites

C_2-C_3 alcohols (~2.2 kPa) were co-fed with water (1.1 kPa) and isobutanol (~5.0 kPa) was fed to the catalyst bed (0.05, 0.10, and 0.20 g of catalyst) at 488 K. Pyridine (0.02 and 0.05 kPa) was introduced to the reactant flow after steady-state rates of dehydration were observed. The effluent composition was monitored with time-on-stream after introduction

of pyridine as a co-feed using an online mass spectrometer. The amount of pyridine to completely deactivate ether synthesis was estimated by linearly extrapolating the initial slope of the deactivation profile, as described in our previous report[43].

2.2.4. Parameter estimation techniques for kinetic modeling

The Athena Visual Studio (v14.2, W.E. Stewart and M. Caracotsios) statistical software package with Bayesian statistical estimation techniques was used to optimize kinetic parameters. Replicates are defined as experimental measurements obtained when the alcohol and water pressures are the same. These measurements represent a collection of independent experiments that involved keeping either the alcohol or water pressure constant while varying the other, as discussed in Section 2.3.3.

2.3. Results and Discussion

2.3.1. Effects of water pretreatment of γ-Al_2O_3 on C_3-C_4 alcohol dehydration rates

The synthesis rates of olefin and ether from 1-PrOH, 2-PrOH, and iBuOH dehydration at 488 K on water-exposed γ-Al_2O_3 (2.2 kPa of water at 488 K for 1 h) samples were lower than the rates on non-exposed γ-Al_2O_3 samples; catalytic rates for samples exposed to water could be regenerated after thermal treatment (1.67 cm^3 s^{-1} of dry air at 723 K for 4 h) as shown in Table 2.1. These effects of water reflect the hydration/coordination of surface alumina as discussed in section 2.1. A decrease in rates and regeneration upon thermal treatment were also observed for ethanol (EtOH) dehydration[43] and show that water molecules irreversibly adsorb onto a fraction of the

catalytic sites, which causes deactivation with time-on-stream at this reaction temperature. Catalyst samples, therefore, were pretreated with water before introduction of alcohol reactants to deactivate this fraction of sites and run under steady state conditions.

Table 2.1 Olefin and ether synthesis rates for 1-PrOH, 2-PrOH, and iBuOH dehydration with 2.5 kPa alcohol partial pressures at 488 K on γ-Al_2O_3 (0.02 g for 1-PrOH and 2-PrOH and 0.01 g for iBuOH) under total gas flowrate of 3.4 cm^3 s^{-1} for a catalyst sample which was not pretreated with water, a catalyst sample which was pretreated with 2.2 kPa of water for 1 h, and a regenerated water-pretreated sample with drying air (1.67 cm^3 s^{-1}) at 723 K for 4 h

Catalyst sample	Olefin synthesis rate (/10^{-6} mol g_{cat}^{-1} s^{-1})			Ether synthesis rate (/10^{-6} mol g_{cat}^{-1} s^{-1})		
	1-PrOH	2-PrOH	iBuOH	1-PrOH	2-PrOH	iBuOH
No water pretreated	4.99	31.4	5.48	5.12	2.54	0.170
Water pretreated	1.97	21.5	2.59	3.77	1.75	0.121
Regenerated	5.30	37.8	5.61	5.72	2.94	0.176

2.3.2. Kinetic isotope effects for C_3-C_4 alcohol dehydration

Kinetic isotope effects (KIE) probing the involvement of C-H and O-H bonds in kinetically relevant steps for mono- and di-alcohol dehydration of 1-PrOH, 2-PrOH, and iBuOH were measured. The rates of mono- and di-alcohol dehydration using protium-form C_3-C_4 alcohols relative to the rates of dehydration using deuterated reactants such as C_3D_7OD (1-PrOH-d_8), C_3H_7OD (1-propanol-OD), $CD_3CD(OD)CD_3$ (2-PrOH-d_8), $CH_3CH(OD)CH_3$ (2-propanol-OD), C_4D_9OH (iBuOH-d_9), and C_4H_9OD (isobutanol-OD) (r_H/r_D) at 488 K are presented in Tables 2.2-4.

No significant effect (Tables 2.2-4) on the rate of di-alcohol dehydration is observed using any deuterated reactant, demonstrating that the rate-determining step (RDS) of di-alcohol dehydration does not involve the cleavage of a C-H or O-H bond, similar to what has previously been reported for EtOH dehydration[43]. The RDS for dipropyl ether (DPE), diisopropyl ether (DiPE), and diisobutyl ether (DiBE) formation, therefore, involves C_α-O or Al-O bond breakage. The rates of mono-alcohol dehydration using 1-propanol-OD, 2-propanol-OD, and isobutanol-OD as reactants are not significantly different (Tables 2.2-4) suggesting that O-H bond cleavage is not the kinetically relevant step in olefin formation. A primary kinetic isotope effect was observed for olefin formation when using 1-PrOH-d_8, 2-PrOH-d_8, and iBuOH-d_9 as reactants, confirming that C_β-H bond cleavage is the RDS for mono-alcohol dehydration. These observations and conclusions are in agreement with prior reports by Knözinger and Scheglila[42] for 2-butanol, tert-butanol, and iBuOH dehydration at temperatures similar to those used in this research (393-483 K) and by Shi et al.[46] for tert-butanol dehydration on γ-Al_2O_3 over the temperature range 458-493 K.

2.3.3. Kinetics and mechanism of alcohol dehydration

The rates and selectivity of 1-PrOH, 2-PrOH, and iBuOH dehydration were measured at varying alcohol and water partial pressures to assess the kinetics of parallel mono- and di-alcohol dehydration mechanisms.

Table 2.2 Measured kinetic isotope effects for propene and DPE synthesis at 488 K for the dehydration of 1-PrOH-d_8 and 1-propanol-OD over γ-Al_2O_3 with 0.7 kPa of alcohols and 0.5 kPa of water (H_2O for 1-PrOH and D_2O for 1-PrOH-d_8 and 1-propanol-OD) at 3.4 cm^3 s^{-1} of total flow rate

Reactant / Product	1-PrOH-d_8	1-propanol-OD
Propene KIE (r_H/r_D)	2.03 ± 0.25	0.90 ± 0.09
DPE KIE (r_H/r_D)	0.86 ± 0.08	0.88 ± 0.05

Table 2.3 Measured kinetic isotope effects for propene and DiPE synthesis at 488 K for the dehydration of 2-PrOH-d_8 and 2-propanol-OD over γ-Al_2O_3 with 0.6 kPa of alcohols and 0.7 kPa of water (H_2O for 2-PrOH and D_2O for 2-PrOH-d_8 and 2-propanol-OD) at 3.4 cm^3 s^{-1} of total flow rate

Reactant / Product	2-PrOH-d_8	2-propanol-OD
Propene KIE (r_H/r_D)	2.18 ± 0.12	1.17 ± 0.04
DiPE KIE (r_H/r_D)	0.82 ± 0.02	1.06 ± 0.02

Table 2.4 Measured kinetic isotope effects for isobutene and DiBE synthesis at 488 K for the dehydration of iBuOH-d_9 and isobutanol-OD over γ-Al_2O_3 with 0.7 kPa of alcohols and 0.3 kPa of water (H_2O for iBuOH and D_2O for iBuOH-d_9 and isobutanol-OD) at 3.4 cm^3 s^{-1} of total flow rate

Reactant / Product	iBuOH-d_9	isobutanol-OD
Isobutene KIE (r_H/r_D)	1.97 ± 0.11	1.09 ± 0.06
DiBE KIE (r_H/r_D)	1.00 ± 0.06	1.05 ± 0.06

2.3.3.1. Kinetics and mechanism of mono-alcohol dehydration

2.3.3.1.1. Kinetics and mechanism of 1-PrOH mono-alcohol dehydration

The propene formation rate when co-feeding 1-PrOH and water at 488 K showed negative order dependencies on 1-PrOH and water pressure as shown in Figure 2.1 (1-PrOH partial pressure = 0.4-7.3 kPa and water partial pressure = 0.3-2.2 kPa). The reaction order in 1-PrOH (between -0.2 and 0) changes with water pressure and asymptotically lines out to zero at high water pressure (~1.1 kPa) suggesting that inhibition of mono-alcohol dehydration rates by water is a consequence of 1-PrOH/water dimers on the surface. Propene synthesis rate was observed to have a water pressure dependence less than negative one (-1.3) at low 1-PrOH partial pressure (~0.70 kPa) and high water partial pressure (>2 kPa) as shown in Figure 2.5, suggesting the existence of water dimers on the surface that inhibit mono-alcohol dehydration rates. The negative order in 1-PrOH reveals that 1-PrOH dimers exist on the surface and also inhibit the formation of propene. 1-PrOH monomers are expected to be prominent on the catalyst surface as they are involved in the RDS for mono-alcohol 1-PrOH dehydration. A kinetic model that considers 1-PrOH monomers, 1-PrOH dimers, 1-PrOH/water dimers, water monomers, and water dimers as surface species that competitively occupy surface sites can consistently describe these observations as discussed below.

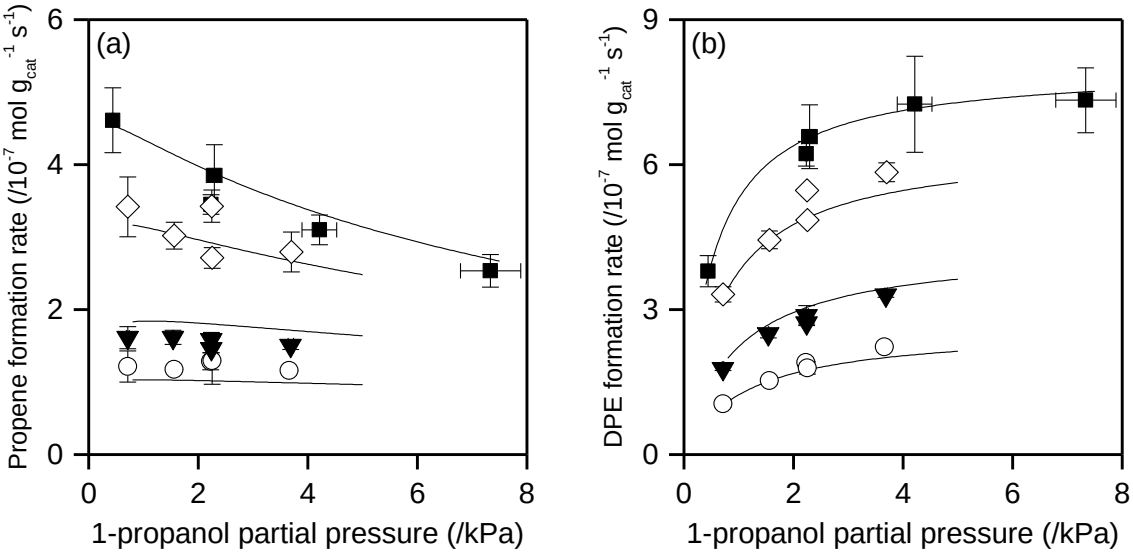

Figure 2.1 (a) Propene and (b) DPE formation rate for 1-PrOH dehydration at 488K on γ-Al_2O_3 as a function of 1-PrOH partial pressure with 0.32 (■), 0.55 (◇), 1.1 (▼), and 2.2 (○) kPa water co-feeds (total gas flowrate = 3.4 cm^3 s^{-1}). The solid line represents the model fits to Equation 2.2 and 2.4 for (a) and (b), respectively.

The alcohol monomer involved in the RDS of olefin formation can be either a physisorbed molecular-complex[34] or a chemisorbed alkoxide. Pines and Haag[47] observed that both 1-butanol dehydration and 1-butene double-bond isomerization showed a nearly identical cis/trans ratio (~2) for 2-butene synthesis on alumina, indicating that alcohol dehydration is accompanied by fast adsorption and isomerization of the olefin. The cis/trans ratio for 2-butanol dehydration and 2-butene isomerization on alumina was also observed to be identical (~4.3). These results suggest that the intermediates for alcohol dehydration and olefin double bond isomerization are the same and that desorption of these intermediates is the rate-limiting step. Macht et al.[48] also observed that the cis/trans ratio of 2-butene is nearly identical for 2-butanol dehydration and 1-butene isomerization on

polyoxometalate catalysts. The authors concluded that surface alkoxide species dissociated from alcohols are common intermediates between the two reactions. When γ-Al_2O_3 was exposed to EtOH (308-573 K), IR spectra of the alumina contained a band similar to $Al(OCH_2CH_3)_3$, suggesting the existence of alkoxide species[49]. Chemical shifts representing alkoxide species were also observed in ^{13}C solid state NMR measurements of γ-Al_2O_3 exposed to ^{13}C labeled propene, n-butene, and isobutene (63 and 79 ppm, 69 and 74 ppm, and 67 ppm, respectively)[50]. Knözinger and Scheglila[42] considered concurrent C-H and C-OH bond cleavage in an adsorbed alcohol on γ-Al_2O_3 and postulated a mechanism that does not consider surface alkoxide species. Recent density functional theory calculations reported by Christiansen et al.[34], also show that molecularly intact alcohol precursors mediate mono-alcohol dehydration on the (100) surface of γ-Al_2O_3 with a lower barrier than alkoxide precursors. Kinetically these two postulates are indistinguishable except the appearance of an equilibrium parameter for alcohol dissociation, K_d, (Step 2, Scheme 2.1) in the rate expression. K_d cannot be explicitly assessed from the kinetic studies that we report and always appears in the rate expression accompanied with other equilibrium constants. We postulate the existence of alkoxide species (Scheme 2.1) and the RDS to involve C-H bond cleavage in this surface intermediate, however, as pointed out above, an equivalent model considering C-H bond cleavage from molecular alcohol precursors to be the RDS would result in a kinetically indistinguishable model. The mechanism proposed in Scheme 2.1 comprising of surface propoxide species, water and 1-PrOH monomers and dimers, and 1-PrOH/water dimers can explain the measured kinetic dependencies for propene synthesis. All intermediates are considered to be in quasi-

equilibrium before the RDS. A 1-PrOH molecule adsorbs onto γ-Al_2O_3 (Step 1, Scheme 2.1) and subsequently dissociates to form a 1-propoxide species and an adsorbed hydrogen atom (Step 2, Scheme 2.1). The 1-propoxide species desorbs from the surface by β-hydrogen elimination and is converted to a propene molecule and a hydroxyl group in the RDS (Step 3, Scheme 2.1). The hydroxyl group and a hydrogen atom on the surface desorb to form a water molecule, which completes the catalytic cycle and regenerates the catalytic surface (Step 4, Scheme 2.1). The adsorption of a water molecule (Step 5, Scheme 2.1) and the subsequent adsorption of a second water molecule or a 1-PrOH molecule forming either a water dimer (Step 6, Scheme 2.1) or a 1-PrOH/water dimer (Step 7a, Scheme 2.1), respectively, can inhibit the catalytic rate. A water molecule can also adsorb onto a surface bound 1-PrOH molecule to form the 1-PrOH/water dimer (Step 7b, Scheme 2.1). Steps 7a and Step 7b which both form a 1-PrOH/water dimer, however, cannot be kinetically distinguished. The 1-PrOH dimer species formed from the adsorption of an additional 1-PrOH molecule onto the 1-PrOH adsorbed site can also inhibit propene formation (Step 8, Scheme 2.1).

The propene formation rate (r_{olefin}) derived from the mechanism depicted in Scheme 2.1 is shown in Equation 2.1.

$$r_{olefin} = \frac{k_{olefin} K_d K_{A1} P_{alcohol}}{1+K_d K_{A1} P_{alcohol}+K_{W1} P_{water}+(K_{W1} K_{AWa}+K_{A1} K_{AWb}) P_{alcohol} P_{water}+K_{A1} K_{A2} P_{alcohol}^2+K_{W1} K_{W2} P_{water}^2} \quad (2.1)$$

k_{olefin} is the rate constant of the RDS while K_d, K_{A1}, K_{A2}, K_{W1}, K_{W2}, and K_{AW} are equilibrium constants for the dissociation of adsorbed 1-PrOH to form 1-propoxide species, formation of adsorbed 1-PrOH, 1-PrOH dimer, adsorbed water, water dimer, and 1-

PrOH/water dimer, respectively, on the surface. K_{AWa} and K_{AWb} are equilibrium constants for the two indistinguishable routes to form a 1-PrOH/water dimer.

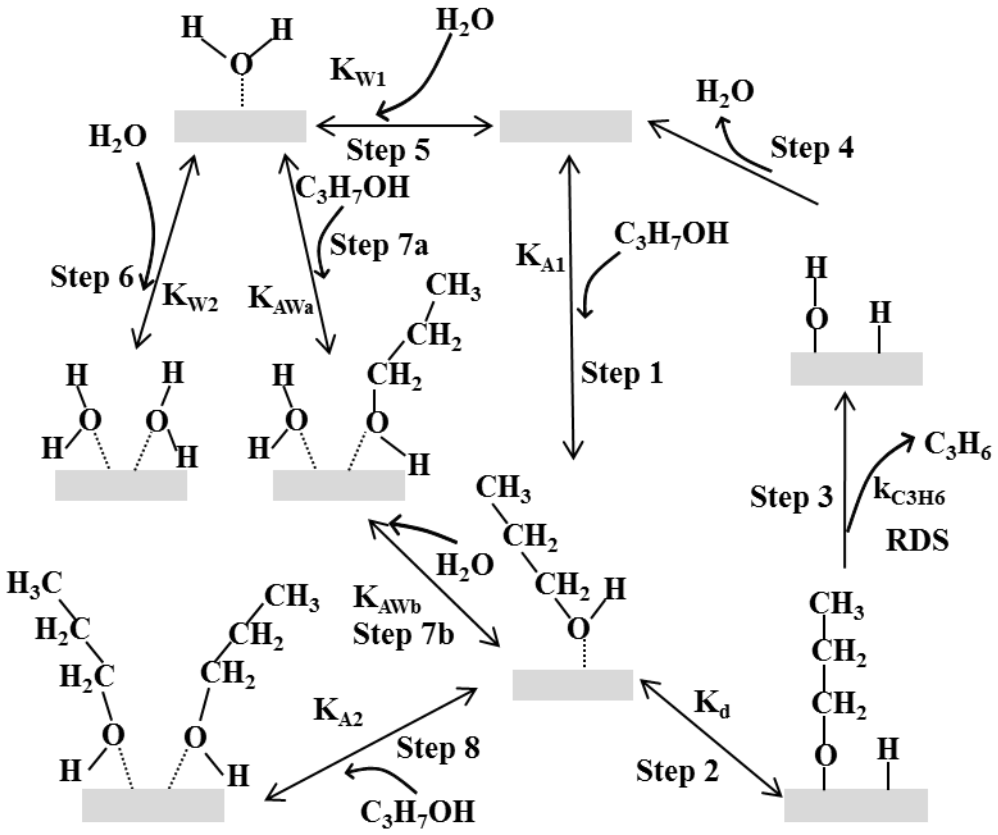

Scheme 2.1 1-Propoxide desorption limited mechanism for propene formation from 1-PrOH dehydration

The observed negative order dependence of propene formation rates on water and 1-PrOH pressures and the observed kinetic isotope effect implying the involvement of alkoxide species in the RDS indicate that the 1-propoxide group, 1-PrOH/water dimers, 1-

PrOH dimers, and water dimers are the dominant surface species and a simplified rate expression shown in Equation 2.2 can be derived from Equation 2.1.

$$r_{olefin} = \frac{k_{olefin} P_{alcohol}}{P_{alcohol} + \frac{K'_{AW}}{K_{A1} K_d} P_{alcohol} P_{water} + \frac{K_{A1} K_{A2}}{K_{A1} K_d} P^2_{alcohol} + \frac{K_{W1} K_{W2}}{K_{A1} K_d} P^2_{water}} \quad (2.2)$$

K'_{AW} represents the sum of the equilibrium constants for two indistinguishable routes for the formation of 1-PrOH/water dimer species (K'_{AW} = $K_{W1}K_{AWa}$ + $K_{A1}K_{AWb}$). Based on Equation 2.2, a non-linear parameter estimation of the propene formation rate data was performed using Athena Visual Studio (v14.2, W.E. Stewart and M. Caracotsios) to determine rate and equilibrium parameters shown in Equation 2.2. The optimized parameters are shown in Table 2.5 and the model fits to Equation 2.2 are shown in Figure 2.1. Analysis of residual error in the kinetic model is reported in Section 2.5, Figure 2.7-9.

Table 2.5 Estimated kinetic parameters for mono-alcohol dehydration of 1-PrOH on γ-Al_2O_3 at 488 K using the model presented in Equation 2.2 and data from Figure 2.1

Parameter	$k_{C_3H_6}$ (/10^{-6} mol_{C3H6} g_{cat}^{-1} s^{-1})	$\frac{K'_{AW}}{K_{A1}K_d}$ (/kPa^{-1})	$\frac{K_{A1}K_{A2}}{K_{A1}K_d}$ (/kPa^{-1})	$\frac{K_{W1}K_{W2}}{K_{A1}K_d}$ (/kPa^{-1})
Estimated Value	1.20 ± 0.34	4.49 ± 1.85	0.271 ± 0.117	0.292 ± 0.461

The much larger value of $\frac{K'_{AW}}{K_{A1}K_d}$, 4.49, compared to $\frac{K_{A1}K_{A2}}{K_{A1}K_d}$, 0.271, and $\frac{K_{W1}K_{W2}}{K_{A1}K_d}$, 0.292, suggests that 1-PrOH/water dimers predominantly occupy the surface at the alcohol and water pressures used in this study and that the concentrations of 1-PrOH dimers and water dimers are low. This model consistently explains the negative order dependence of the

reaction rate on $P_{1\text{-PrOH}}$ (between -0.2 and 0) and the asymptotic convergence of the order in $P_{1\text{-PrOH}}$ to zero as P_{water} increases.

2.3.3.1.2. Kinetics and mechanism of 2-PrOH mono-alcohol dehydration

The propene formation rate from 2-PrOH and water co-fed at 488 K showed zero order dependence on 2-PrOH partial pressure and negative order dependence on water partial pressure as shown in Figure 2.2 (2-PrOH partial pressure = 2.2-7.2 kPa; and water partial pressure = 0.33-2.1 kPa). A slight positive dependence on 2-PrOH at low partial pressures ($\leq$ 2 kPa) was observed. These observations corroborate the inference that water and 2-PrOH/water dimers inhibit mono-alcohol dehydration. The less than negative one dependence of propene formation rates on water partial pressures at low 2-PrOH partial pressure (~0.65 kPa) and high water partial pressure (>2 kPa) ($r_{C3H6} \propto P_{H2O}^{-1.34}$) as shown in Figure 2.5, confirms the existence of water dimers on the surface. The reaction order in 2-PrOH is slightly negative at high 2-PrOH pressure ($\geq$ 2 kPa) and low water pressure (~0.33 kPa), which suggests inhibition of mono-alcohol dehydration rates by 2-PrOH dimers on the surface. 2-PrOH monomers are expected to exist in the RDS because the olefin is formed from mono-alcohol dehydration. The model for 1-PrOH, Scheme 2.1, and Equation 2.1 can also explain the mechanism of 2-PrOH mono-alcohol dehydration. The 2-propoxide species, 2-PrOH/water dimers, 2-PrOH dimers, and water dimers are identified as dominant surface species from experimental rate dependences and, therefore, a surrogate of Equation 2.1 for 2-PrOH can be simplified to Equation 2.2. The parameters and the model fit of this equation are shown in Table 2.6 and Figure 2.2, respectively.

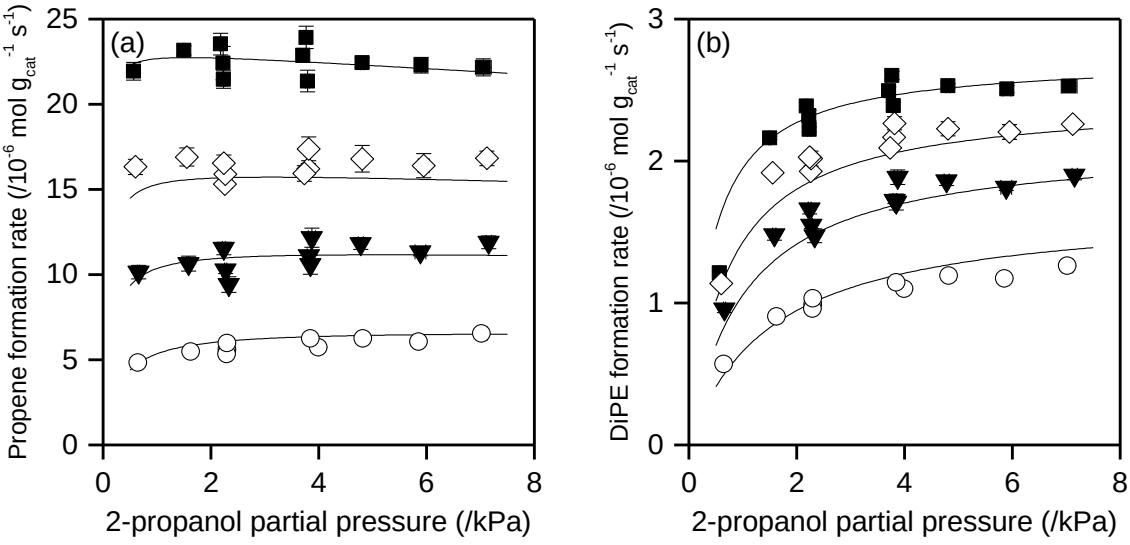

Figure 2.2 (a) Propene and (b) DiPE formation rate for 2-PrOH dehydration at 488K on γ-Al_2O_3 as a function of 2-PrOH partial pressure with 0.33 (■), 0.65 (◇), 1.1 (▼), and 2.1 (○) kPa water co-feeds (total gas flowrate = 3.4 $cm^3\ s^{-1}$). The solid line represents the model fits to Equations 2.2 and 2.4 for (a) and (b), respectively.

Table 2.6 Estimated kinetic parameters for mono-alcohol dehydration of 2-PrOH on γ-Al_2O_3 at 488 K using the model presented in Equation 2.2 and data from Figure 2.2

Parameter	$k_{C_3H_6}$ ($/10^{-5}$ mol_{C3H6} g_{cat}^{-1} s^{-1})	$\frac{K'_{AW}}{K_{A1}K_d}$ ($/kPa^{-1}$)	$\frac{K_{A1}K_{A2}}{K_{A1}K_d}$ ($/kPa^{-1}$)	$\frac{K_{W1}K_{W2}}{K_{A1}K_d}$ ($/kPa^{-1}$)
Estimated Value	4.13 ± 0.34	2.33 ± 0.33	0.0163 ± 0.0184	0.371 ± 0.184

The high value of $\frac{K'_{AW}}{K_{A1}K_d}$, 2.33, compared to $\frac{K_{A1}K_{A2}}{K_{A1}K_d}$, 0.0163, and $\frac{K_{W1}K_{W2}}{K_{A1}K_d}$, 0.371, shows that 2-PrOH/water dimers are the dominant surface species under the reaction conditions employed, similar to the observation noted above for 1-PrOH/water dimers

being dominant for 1-PrOH dehydration. The much smaller value of $\frac{K_{A1}K_{A2}}{K_{A1}K_d}$ in reference to other adsorption parameters suggests that 2-PrOH dimers are scarce and explains the weaker negative dependence on alcohol partial pressure for 2-PrOH compared to 1-PrOH. This model explains the mono-alcohol dehydration rate dependences on 2-PrOH and water partial pressures. The rate constant of propene formation for 2-PrOH dehydration is 4.13×10^{-5} $mol_{propene}$ g_{cat}^{-1} s^{-1} which is an order of magnitude larger than the rate constant for 1-PrOH dehydration, 1.20×10^{-6} $mol_{propene}$ g_{cat}^{-1} s^{-1}. The increased rate constant with C_α substitution as noted for 2-PrOH in comparison with 1-PrOH, and thus, carbocation stability is indicative of a carbocation-like transition state[22,33]. The difference in reaction rate constants among different alcohols will be discussed further in Section 2.3.5.

2.3.3.1.3. Kinetics and mechanism of iBuOH mono-alcohol dehydration

The isobutene formation rate when feeding iBuOH and water mixtures at 488 K is shown in Figure 2.3 (iBuOH partial pressure = 0.08-7.3 kPa and water partial pressure = 0.34-4.5 kPa). The isobutene synthesis rate decreased as water partial pressure increased. At low iBuOH partial pressure (≤1 kPa), the isobutene synthesis rate shows positive dependence on iBuOH pressure. At higher iBuOH partial pressures (>1 kPa), the reaction order in iBuOH is negative at low water pressure (~0.34 kPa) and asymptotically lines out to zero as water pressure increases (>1.1 kPa). These observations show that water and iBuOH/water dimers inhibit isobutene formation. The observed negative dependence of mono-alcohol dehydration rates on iBuOH confirms inhibition by iBuOH dimers on the surface. Similar to 1- and 2-PrOH, water pressure dependences less than negative one were

observed at high water and low iBuOH partial pressures, suggesting that water dimers are formed and inhibit mono-alcohol dehydration. iBuOH monomers are involved in the RDS as observed in other mono-alcohol C_2-C_3 alcohol dehydration mechanisms. The dimer inhibition model proposed by DeWilde et al.[43], therefore, rigorously describes the observed reaction order dependences not only for EtOH but also for longer and more substituted C_3-C_4 alcohols. Equation 2.1 was modified to Equation 2.2 with dominant isobutoxide species, iBuOH/water dimers, iBuOH dimers, and water dimers. The estimated parameters are shown in Table 2.7 and the model fit is shown in Figure 2.3.

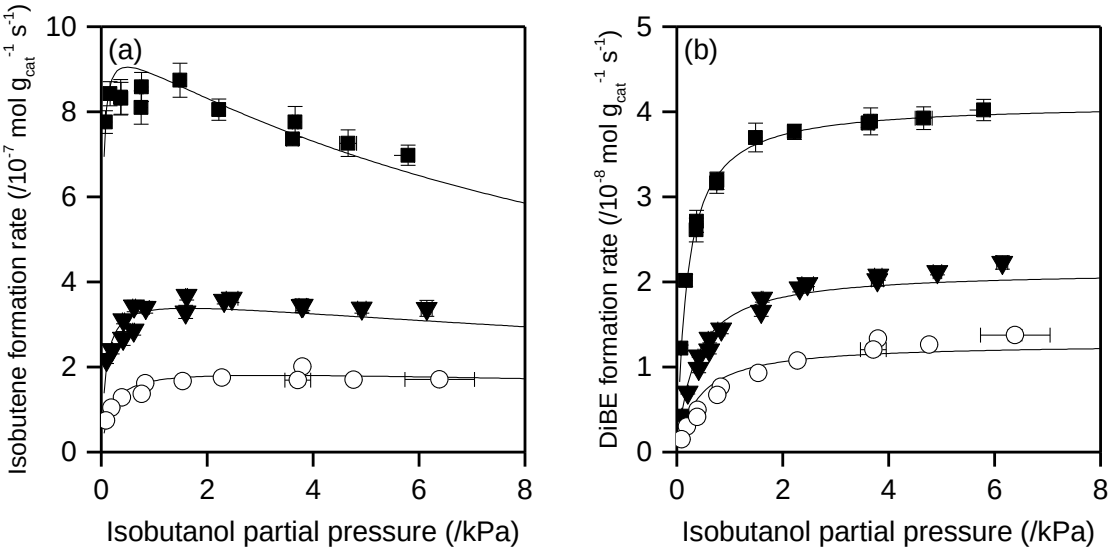

Figure 2.3 (a) Isobutene and (b) DiBE formation rate for iBuOH dehydration at 488K on γ-Al_2O_3 as a function of iBuOH partial pressure with 0.34 (■), 1.1 (▼), and 2.3 (○) kPa water co-feeds (total gas flowrate = 3.4 cm^3 s^{-1}). The solid line represents the model fits to Equation 2.2 and 2.4 for (a) and (b), respectively.

Table 2.7 Estimated kinetic parameters for mono-alcohol dehydration of iBuOH on γ-Al_2O_3 at 488 K using the model presented in Equation 2.2 and data from Figure 2.3

Parameter	$k_{C_4H_8}$ ($/10^{-6}$ mol_{C4H8} g_{cat}^{-1} s^{-1})	$\frac{K'_{AW}}{K_{A1}K_d}$ ($/kPa^{-1}$)	$\frac{K_{A1}K_{A2}}{K_{A1}K_d}$ ($/kPa^{-1}$)	$\frac{K_{W1}K_{W2}}{K_{A1}K_d}$ ($/kPa^{-1}$)
Estimated Value	3.29 ± 0.76	6.86 ± 2.05	0.282 ± 0.101	0.577 ± 0.243

iBuOH/water dimer dominates the γ-Al_2O_3 surface at the conditions employed as inferred from the assessed values of adsorption parameters: $\frac{K'_{AW}}{K_{A1}K_d}$, 6.86, $\frac{K_{A1}K_{A2}}{K_{A1}K_d}$, 0.282, and $\frac{K_{W1}K_{W2}}{K_{A1}K_d}$, 0.577. iBuOH dimers are nearly absent from the surface at these conditions. The isobutene formation rate dependences on iBuOH and water partial pressures are explained by this model. The rate constant of isobutene formation is $3.29x10^{-6}$ $mol_{isobutene}$ g_{cat}^{-1} s^{-1}; this value is similar to the rate constant of propene formation from 1-PrOH because both alcohols have primary C_α. The electron donating methyl groups of iBuOH will stabilize the carbocation-like transition state to a greater degree than those of 1-PrOH, which results in a slightly larger rate constant for isobutene formation. The comparison of reaction rate constants among different alcohols will be discussed in Section 2.3.5.

2.3.3.2. Kinetics and mechanism of di-alcohol dehydration

2.3.3.2.1. Kinetics and mechanism of 1-PrOH di-alcohol dehydration

The measured rates of DPE formation increase with increasing 1-PrOH pressure and asymptotically line out at high 1-PrOH pressure (~4.2 kPa) at 488K as shown in Figure 2.1 (1-PrOH partial pressure = 0.4-7.3 kPa and water partial pressure = 0.3-2.2 kPa). Ether

formation occurs via an S_N2 type di-alcohol dehydration step[21,44] as discussed in Section 2.1, so 1-PrOH dimers on the surface are considered to be involved in the RDS. The DPE synthesis rate asymptotically lined out and showed negative order (nearly -1) for water at high 1-PrOH pressure (~4.2 kPa), which can be explained by the inhibition of 1-PrOH dimer/water monomer trimers on the surface of γ-Al_2O_3; the involvement of trimers is inferred from the formation rates of DPE asymptotically lining out to different values at high 1-PrOH pressures depending on the water pressure (Figure 2.1). The inhibition of water and positive dependence on 1-PrOH pressure at low partial pressures of 1-PrOH (<2.3 kPa) can be explained by the existence of 1-PrOH/water dimers. A kinetic model, similar to that for propene formation discussed above, with 1-PrOH monomers, 1-PrOH dimers, water monomers, water dimers, 1-PrOH/water dimers, and 1-PrOH dimer/water monomer trimers is proposed and discussed below.

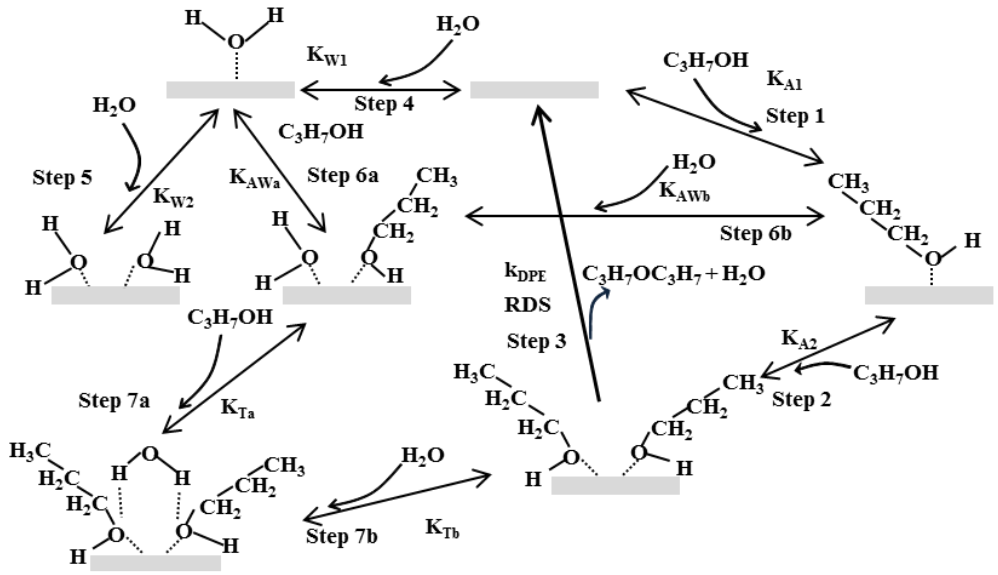

Scheme 2.2 1-PrOH dimer/water monomer trimer inhibition mechanism for DPE formation from 1-PrOH dehydration

A 1-PrOH molecule adsorbs on the γ-Al_2O_3 surface (Step 1, Scheme 2.2) followed by co-adsorption of another 1-PrOH molecule (Step 2, Scheme 2.2). Subsequent dehydration of the 1-PrOH dimer forms DPE and water while regenerating the catalytic site in the RDS (Step 3, Scheme 2.2). This step, however, is assumed to be comprised of several fundamental steps; some of which are not kinetically observable. A water molecule can non-dissociatively adsorb on the active site (Step 4, Scheme 2.2) and following adsorption of a second water molecule or a 1-PrOH molecule forms either a water dimer (Step 5, Scheme 2.2) or a 1-PrOH/water dimer (Step 6a, Scheme 2.2), respectively, capable of inhibiting DPE synthesis. The co-adsorption of a water molecule with an adsorbed 1-PrOH species could also form 1-PrOH/water dimers as discussed in Section 2.3.3.1 (Step 6b, Scheme 2.2). The existence of only monomeric and dimeric 1-PrOH and water species is, however, inconsistent with the asymptotic behavior of ether synthesis rates at high alcohol pressures. A mechanism that considers only 1-PrOH/water and water dimers to inhibit rates would predict that DPE synthesis rates at high 1-PrOH pressures rates asymptotically converge to a single value, independent of water pressure. Experimental observations contradict this model (for 1-PrOH, 2-PrOH, and iBuOH as shown below) and lead us to postulate another inhibiting species, a 1-PrOH dimer/water monomer trimer which is formed by addition of 1-PrOH to 1-PrOH/water dimer (Step 7a, Scheme 2.2) or water to 1-PrOH dimer (Step 7b, Scheme 2.2). A trimeric species as postulated above does not require each of the three species to interact with the active site; instead, it may involve, for example, the interaction/adsorption of water with a surface adsorbed alcohol dimer via hydrogen bonding. This surface-bound complex comprising two molecules of the alcohol

and a water molecule would therefore be unreactive for di-alcohol dehydration and would describe the observed inhibition of reaction rates by water.

Equation 2.3 represents the DPE formation rate equation (r_{ether}) derived from the proposed mechanism in Scheme 2.2 with k_{ether} as the rate constant of the RDS.

$$r_{ether} = k_{ether}K_{A1}K_{A2}P_{alcohol}^2/\left[1 + K_{A1}P_{alcohol} + K_{W1}P_{water} + (K_{W1}K_{AWa} + K_{A1}K_{AWb})P_{alcohol}P_{water} + K_{A1}K_{A2}P_{alcohol}^2 + K_{W1}K_{W2}P_{water}^2 + \{(K_{W1}K_{AWa} + K_{A1}K_{AWb})K_{Ta} + K_{A1}K_{A2}K_{Tb}\}P_{alcohol}^2P_{water}\right] \quad (2.3)$$

The 1-PrOH dimer/water monomer trimer term in the denominator explains the concurrent zero order dependence on 1-PrOH pressure and the inverse order dependence on water pressure observed experimentally at high 1-PrOH partial pressures (>4.2 kPa). The positive order in 1-PrOH and the negative order dependence on water pressures observed at low 1-PrOH pressures (<2.3 kPa) mandates the existence of 1-PrOH/water dimers. Equation 2.3 was simplified to Equation 2.4 based on the observed pressure dependences of DPE synthesis rates on 1-PrOH and water pressures to include only 1-PrOH dimers, 1-PrOH/water dimers, and 1-PrOH dimer/water monomer trimers as the prominent surface species.

$$r_{ether} = \frac{k_{ether}P_{alcohol}^2}{P_{alcohol}^2 + \frac{K'_{AW}}{K_{A1}K_{A2}}P_{alcohol}P_{water} + \frac{K'_{T}}{K_{A1}K_{A2}}P_{alcohol}^2P_{water}} \quad (2.4)$$

K'_{AW} and K'_{T} represent the sum of the equilibrium constants of two indistinguishable routes for the formation of 1-PrOH/water dimers and 1-PrOH dimer/water monomer trimers ($K'_{AW} = K_{W1}K_{AWa} + K_{A1}K_{AWb}$ and $K'_{T} = (K_{W1}K_{Awa}+K_{A1}K_{AWb})K_{Ta} + K_{A1}K_{A2}K_{Tb}$).

Non-linear parameter estimation of the DPE synthesis rate data to calculate rate and equilibrium parameters shown in Equation 2.4 resulted in the optimized parameters shown in Table 2.8 and a fit of the data shown in Figure 2.1. The similar values of $\frac{K'_{AW}}{K_{A1}K_{A2}}$, and $\frac{K'_{T}}{K_{A1}K_{A2}}$, imply that DPE synthesis rates are independent of 1-PrOH pressure at high 1-PrOH pressure (Figure 2.1).

Table 2.8 Estimated kinetic parameters of DPE formation from 1-PrOH on γ-Al_2O_3 at 488 K using the model presented in Equation 2.4 and data from Figure 2.1

Parameter	k_{DPE} ($/10^{-6}$ mol_{DPE} g_{cat}^{-1} s^{-1})	$\frac{K'_{AW}}{K_{A1}K_{A2}}$	$\frac{K'_{T}}{K_{A1}K_{A2}}$ ($/kPa^{-1}$)
Estimated Value	1.27 ± 0.09	2.50 ± 0.29	1.79 ± 0.34

Table 2.9 Estimated kinetic parameters of DiPE formation from 2-PrOH on γ-Al_2O_3 at 488 K using the model presented in Equation 2.4 and data from Figure 2.2

Parameter	k_{DiPE} ($/10^{-6}$ mol_{DiPE} g_{cat}^{-1} s^{-1})	$\frac{K'_{AW}}{K_{A1}K_{A2}}$	$\frac{K'_{T}}{K_{A1}K_{A2}}$ ($/kPa^{-1}$)
Estimated Value	3.08 ± 0.16	1.36 ± 0.23	0.403 ± 0.108

Table 2.10 Estimated kinetic parameters of DiBE formation from iBuOH on γ-Al_2O_3 at 488 K using the model presented in Equation 2.4 and data from Figure 2.3

Parameter	k_{DiBE} ($/10^{-8}$ mol_{DiBE} g_{cat}^{-1} s^{-1})	$\frac{K'_{AW}}{K_{A1}K_{A2}}$	$\frac{K'_{T}}{K_{A1}K_{A2}}$ ($/kPa^{-1}$)
Estimated Value	6.82 ± 0.41	0.962 ± 0.121	1.93 ± 0.22

2.3.3.2.2. Kinetics and mechanism of 2-PrOH and iBuOH di-alcohol dehydration

DiPE and DiBE synthesis rates show similar trends as DPE synthesis. Ether formation rates asymptotically converge to different values at high alcohol pressure (>4 kPa) and concurrently show a negative order dependence (nearly -1) on the water partial pressure. A positive dependence on alcohol pressure and negative dependence on water pressure at low alcohol pressures (<2 kPa) is also observed. The mechanism in Scheme 2.2 and the rate equation derived for di-alcohol dehydration (Equation 2.4) thus, accurately describes ether synthesis for 1-PrOH, 2-PrOH, and iBuOH. The optimized parameters for DiPE and DiBE are shown in Tables 2.9 and 2.10, respectively. The significantly lower rate constant for DiBE formation (6.82×10^{-8} mol_{DiBE} g_{cat}^{-1} s^{-1}) compared to that for DPE (1.27×10^{-6} mol_{DPE} g_{cat}^{-1} s^{-1}), or DiPE formation (3.08×10^{-6} mol_{DiPE} g_{cat}^{-1} s^{-1},) suggests that the bulky alkyl group in iBuOH causes steric hindrance during S_N2 ether formation reactions. The consequences of this difference in di-alcohol dehydration reaction rate constants on olefin and ether selectivity will be discussed in Section 2.3.5.

Rep et al.[51] measured IR spectra of adsorbed methanol on sodium-exchanged zeolite X (Na-X, silicon/aluminum ratio of 1.3) at 308 K and observed maxima at 3485 and 3354 cm^{-1}. These observations led the authors to postulate the existence of hydrogen-bonding-networks between hydroxyl groups in methanol and oxygen atoms in the zeolite structure (3485 cm^{-1}) and between adsorbed methanol molecules on adjacent Na cations. They proposed that methanol molecules in the Faujasite cage form complexes with more than three molecules stabilized by hydrogen bonding with other alcohols and zeolite surface

oxygen atoms and by interactions between Na cations and the oxygen atom in methanol. Schenkel et al.[52] measured IR spectra of adsorbed C_2-C_4 alcohols (EtOH, 1-PrOH, 1-butanol) on Na-X at 308 K and also observed bands at ~3350 cm^{-1}, similar to what was observed by Rep et al. for methanol adsorption, which led the authors to suggest that trimeric or larger complexes are formed upon adsorption of C_1-C_4 alcohols on to acidic zeolites at low temperatures. Inelastic neutron scattering spectra in this study showed a broad band for the vibrational mode of the alcohol hydroxyl group (a maximum at 715 cm^{-1} for EtOH and 690 cm^{-1} for 1-PrOH and 1-butanol) also indicating the formation of a hydrogen-bond-network. Wang et al.[53] calculated trajectories of water, methanol, and EtOH in bulk solution and microporous silicalite-1 using configurational-bias Monte Carlo in the Gibbs ensemble at 298 K and molecular dynamics at 300-350 K and inferred from these trajectories, that clusters of water, methanol, and EtOH are formed in the zeolite framework. On the same lines, we postulate that alcohol dimer/water monomer trimers exist on γ-Al_2O_3 at these low temperature conditions.

Equation 2.4 can be rewritten in the form of equation 2.5 which considers the surface to comprise of two distinct sites (Scheme 2.3): one site which is predominantly occupied by the alcohol and the other site being occupied by alcohol, water, and alcohol/water dimers.

$$r_{ether} = \frac{k_{ether} P_{alcohol}}{P_{alcohol} + \frac{K_{W1}}{K_{A1}} P_{water} + \frac{K'_{AW}}{K_{A1}} P_{alcohol} P_{water}} \times \frac{P_{alcohol}}{P_{alcohol}} \quad (2.5)$$

Adsorbed water and alcohol/water dimers inhibit observed di-alcohol dehydration rates for this model. Shi and Davis[44] when studying the dehydration of secondary alcohols on γ-

Al_2O_3 proposed that one alcohol molecule should be in alkoxide form and act as a nucleophile while the other alcohol molecule is physisorbed and acts as an electrophile for the S_N2 reaction to form an ether, which requires two adjacent sites. Following Shi and Davis, a two-site model consistent with the observed asymptotic behavior of ether synthesis rates would involve the formation of alkoxide species on one site and the competitive adsorption of alcohol/water monomers and dimers on the other site. The postulate of surface alkoxides being involved in ether synthesis does not contradict the mechanism for olefin synthesis because the sites involved in mono- and di-alcohol dehydration on γ-Al_2O_3 are distinct[43,54]. The two site model and the trimer inhibition model that involves a single site are kinetically indistinguishable and experimentally we cannot establish the involvement of alkoxide and physisorbed species under reaction conditions. Therefore, we discuss both models with the understanding that each of these models results in the correct asymptotic behavior of ether synthesis rates at high alcohol pressures which cannot be correctly explained by a model that considers only monomers and dimers adsorbed on to a single type of catalytic center.

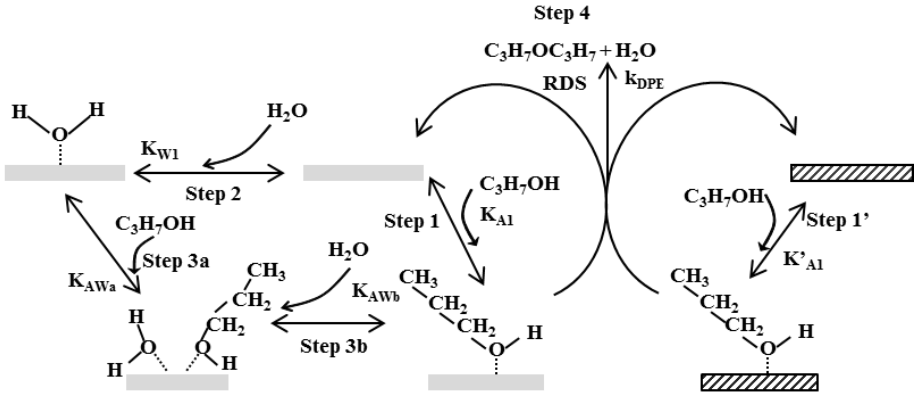

Scheme 2.3 Two distinct sites mechanism for DPE formation from 1-PrOH dehydration

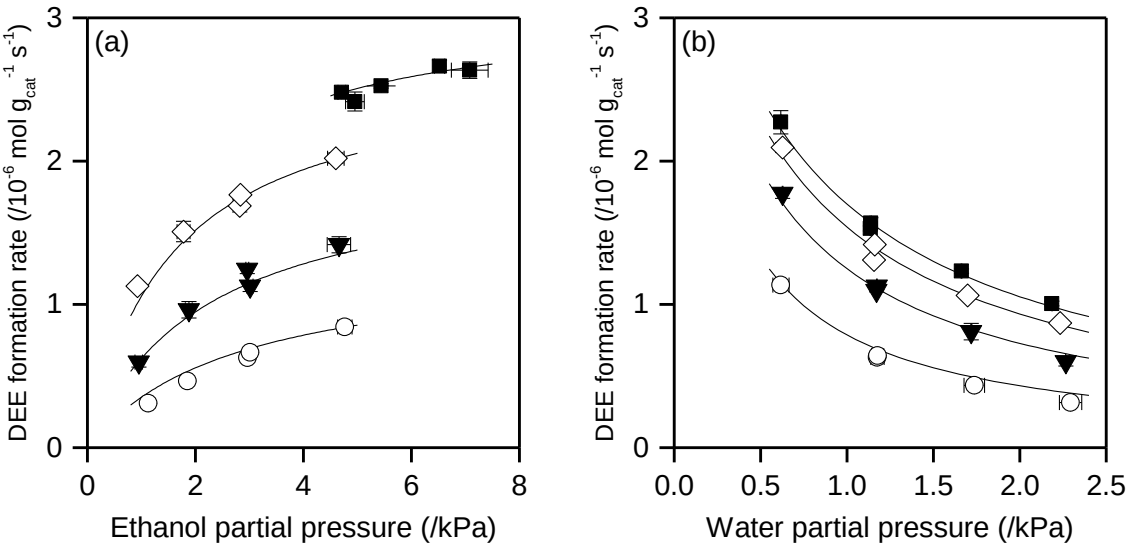

Figure 2.4 DEE formation rate for EtOH dehydration at 488K on γ-Al_2O_3 (a) as a function of EtOH partial pressure with 0.41 (■), 0.62 (◇), 1.2 (▼), and 2.3 (○) kPa water co-feeds and (b) as a function of water partial pressure with 7.1 (■), 4.8 (◇), 2.7 (▼), and 1.1 (○) kPa EtOH co-feeds (total gas flowrate = 3.4 cm^3 s^{-1}). The solid line represents the model fits to Equation 2.4.

Table 2.11 Estimated kinetic parameters of DEE formation from EtOH on γ-Al_2O_3 at 488 K using the model presented in Equation 2.4 and data from Figure 2.4

Parameter	k_{DEE} (/10^{-6} mol$_{DEE}$ g$_{cat}^{-1}$ s^{-1})	$\frac{K'_{AW}}{K_{A1}K_{A2}}$	$\frac{K'_T}{K_{A1}K_{A2}}$ (/kPa^{-1})
Estimated Value	4.40 ± 0.24	4.04 ± 0.35	1.02 ± 0.16

Previously, we reported a model for diethyl ether (DEE) synthesis from EtOH that did not consider the involvement of alcohol dimer/water monomer trimers[43]. We have reassessed these data with the trimer model for ether formation proposed above (Equation 2.4) and note from the results shown in Figure 2.4 and the parameters presented in Table

2.11 that this model fits the experimental results within error and both qualitatively and quantitatively describes the data better than the dimer model that we had postulated previously[43].

The existence of di- and tri-meric surface species on solid acids at these low temperature conditions has been noted spectroscopically as discussed and indirectly inferred from measured rate dependences for a variety of reaction systems involving polar molecules. These examples include inhibition of esterification and dehydration rates on medium and large pore zeolites[55,56] as well as formation of water clusters[53,57]. The existence of multi-meric surface adsorbates therefore is a general phenomenon for polar molecules at low temperatures and their catalytic role is to inhibit the activation and conversion of the monomer/dimer surface adsorbate by competitive adsorption. Specifically, a more complete kinetic rate expression for di-alcohol dehydration reactions discussed above should include terms corresponding to water trimers, alcohol trimers, alcohol monomer/water dimers, however, the conditions used in this research and the observed pressure dependences are such that they allow us to exclude these terms.

2.3.4. Pyridine titration of active sites for di-alcohol dehydration

Pyridine is reversibly adsorbed on Lewis acidic sites of γ-Al_2O_3 and inhibits both mono- and di-alcohol dehydration rates[43,54]. The number of active sites for ether formation was inferred by considering each adsorbed pyridine molecule to titrate one site and linearly extrapolating the initial slope of measured ether synthesis rates (see Figure 2 in DeWilde et al.[43]). In-situ pyridine titration for EtOH, 1-PrOH, 2-PrOH, and iBuOH di-alcohol

dehydration on γ-Al_2O_3 at different pyridine pressures (0.02 and 0.05 kPa) and different catalyst weights (0.05, 0.1, and 0.2 g) resulted in similar pyridine uptakes for the different alcohols as shown in Table 2.12, implying that the active sites for ether formation are independent of alcohol carbon number and branching. The numbers reported in Table 2.12 are in line with density functional theory calculations from Digne et al.[18] that report ~0.4 nm^{-2} surface densities of hydroxyl group free Al surface Lewis acid sites at 450 K.

Table 2.12 Average number of sites for di-alcohol dehydration assessed using in-situ pyridine titration at 488K[a]

	EtOH	1-PrOH	2-PrOH	iBuOH
Number of adsorbed pyridine ($/10^{-5}$ mol g_{cat}^{-1})	6.3±1.9	5.4±0.7	7.2±0.4	8.0±0.2

[a]The 95% confidence intervals were determined based on independent titrations.

Previously, we have used in-situ pyridine titration to show that the number of active sites for di-alcohol dehydration exceed those for mono-alcohol dehydration at 623 K[58]. The distinct site requirements for mono- and di-alcohol dehydration can also be indirectly inferred from the observation that the rate expressions have different denominator terms, an unphysical scenario if the active sites were common. Given the diversity of coordination and hydration of Al and O species on γ-Al_2O_3 surfaces, this is unsurprising, however, this distinction is often overlooked in mechanistic and computational chemistry studies. The number of active centers available for catalysis is expected to be a strong function of the temperature and reaction environment, particularly the presence of water, and can be rigorously probed by in-situ methods such as pyridine titration that we describe above.

2.3.5. Effects of substitution and carbon chain length on olefin selectivity

Table 2.13 Rate constants of olefin and ether formation and selectivity to the olefin product for different alcohols on γ-Al_2O_3 with 2.4 kPa of alcohol and 1.0 kPa of water partial pressure at 488 K

	EtOH	1-PrOH	2-PrOH	iBuOH
Rate constant of olefin formation (/mol_{olefin} g_{cat}^{-1} s^{-1})	3.40 x 10^{-7}	1.20 x 10^{-6}	4.13 x 10^{-5}	3.29 x 10^{-6}
Rate constant of ether formation (/mol_{ether} g_{cat}^{-1} s^{-1})	4.40 x 10^{-6}	1.27 x 10^{-6}	3.08 x 10^{-6}	6.82 x 10^{-8}
Selectivity to olefin[a] (/%)	2.38	22.4	78.9	90.1

[a] Considering the stoichiometry, selectivity reported above is calculated as $\frac{r_{olefin}}{r_{olefin}+2\,r_{ether}}$. The synthesis rates r_{olefin} and r_{ether} are calculated from the model equations for each alcohol species.

EtOH, 1-PrOH, 2-PrOH, and iBuOH show different olefin formation rates and selectivity. A comparison of the rate constants and selectivity of olefin formation is represented in Table 2.13 (The rate constant for EtOH mono-alcohol dehydration is from data in Section 2.5, Table 2.14 and Figure 2.6). EtOH has the lowest rate constant of olefin formation, 3.40 x 10^{-7} mol_{C2H4} g_{cat}^{-1} s^{-1}, the constants for 1-PrOH and iBuOH are similar in magnitude, 1.20 x 10^{-6} mol_{C3H6} g_{cat}^{-1} s^{-1} and 3.29 x 10^{-6} mol_{C4H8} g_{cat}^{-1} s^{-1}, respectively, and 2-PrOH has the highest rate constant, 4.13 x 10^{-5} mol_{C3H6} g_{cat}^{-1} s^{-1}. Olefin formation involves an E2 type mechanism wherein the C-O and C-H bonds on C_β are broken[22,33,42].

Knözinger and coworkers[22,42] postulated the transition state for mono-alcohol dehydration to involve C-O bond elongation resulting in positive charge ($\delta+$) on C_α to explain the trans-elimination of water and the cis-preference in olefinic products, as shown in Scheme 2.4. Roy et al.[33] proposed the same transition state for mono-alcohol EtOH dehydration using cluster based density functional theory calculations. Additional alkyl groups on C_α enhance stability of the carbocationic transition state because of electron donation. Kosteskyy et al.[17] compared dehydration barriers of C_2-C_4 alcohols on Al_2O_3, TiO_2, and ZrO_2 via a concerted E2 mechanism using cluster based DFT calculations in Gaussian (B3LYP/6-311G*) and noted that the barrier for dehydration decreased with increasing substitution of C_α. The maximum in temperature programmed desorption profiles of C_2-C_4 alcohols dosed at sub-monolayer coverages on TiO_2 shifted to lower temperatures as substitution of the C_α increased[59], consistent with an increase in rate constants for mono-alcohol dehydration that we assess. Olefin formation rate constants are of similar magnitude for alcohols with similar C_α substitution and increase dramatically (>10-fold) for 2-PrOH in reference to primary alcohols (see Table 2.13). The degree of substitution of C_β also affects the stability of the transition state because of inductive effects; however, because positive charge is predominantly on C_α and not on C_β, the effect of substituents on C_β is weaker than it is on C_α. The increased substitution on larger alcohols implies 1-PrOH and iBuOH have higher olefin synthesis rate constants than EtOH (see Table 2.13). The preferential selectivity to more substituted olefins (Zaitsev products) in C_4-C_6 alcohol dehydration led Knözinger and coworkers[22] to infer that this was a consequence of increased substitution of C_β. Kim

et al.[59] in the above referenced temperature-programmed desorption study on TiO_2(110) single crystals noted that the temperature corresponding to the maximum rate of desorption decreased as the degree of substitution of both C_α and C_β increased, with the degree of the substitution of C_α having the stronger effect on desorption temperature. The results of the study mirror the results of our kinetic analysis. The observed trends in rate constants for mono-alcohol dehydration of C_2-C_4 alcohols presented in Table 2.13 are consistently explained by the predominance of substitution effects on C_α and weaker dependence of rate parameters on C_β substitution as also noted broadly by Venuto and Landis[60].

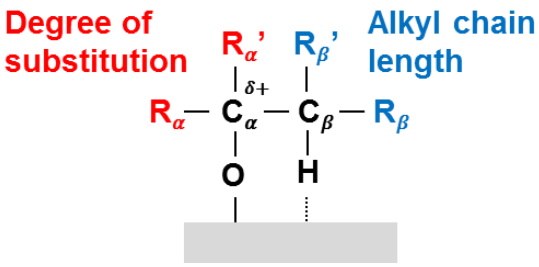

Scheme 2.4 Suggested transition state for mono-alcohol dehydration on γ-Al_2O_3[22,33,42]. C_α has positive charge and H on C_β has interaction with the catalyst surface. R_α, R_α', R_β, and R_β' can be hydrogen or alkyl group.

Olefin selectivity follows the same trend as the rate constant of mono-alcohol dehydration, except iBuOH. We surmise that this is a consequence of steric hindrance for di-alcohol dehydration of iBuOH because of the steric bulk of alkyl groups which results in low selectivity to DiBE and correspondingly to a high olefin selectivity, as indicated by the lower rate constant for the di-alcohol dehydration of iBuOH. Clayborne et al.[61] also

attributed the observed decrease in ether production in temperature programmed desorption of C_1-C_5 alcohols on γ-Al_2O_3 to steric hindrance.

2.4. Conclusion

Primary kinetic isotope effects were observed for propene and isobutene formation on γ-Al_2O_3 when feeding deuterated 1-PrOH, 2-PrOH, or iBuOH reactants implying C-H bond cleavage (such as the C_β-H bond) is involved in the rate-determining step for olefin formation which concurs with a similar observation for EtOH dehydration. The lack of a kinetic isotope for ether formation via di-alcohol dehydration implies C_α-O or Al-O bond cleavage is involved in the rate-determining step. Water inhibition was observed for both olefin and ether formation on γ-Al_2O_3. Steady state kinetic studies show that olefin synthesis rates for mono-alcohol C_3-C_4 alcohol dehydration are inhibited by the alcohol reactant at high partial pressures and low partial pressure of water in agreement with previous observations for ethene formation from EtOH. The mono-alcohol dehydration mechanism previously reported for EtOH is therefore, confirmed as valid for C_2-C_4 alcohols on γ-Al_2O_3 at low temperature conditions. The positive dependence of ether formation rates on alcohol pressure at low values and the asymptotic convergence to different rates depending on water pressure at high alcohol partial pressures implicates the involvement of either trimeric species or two sites. These kinetically indistinguishable models rigorously predict ether formation rates via di-alcohol C_2-C_4 alcohol dehydration. 2-PrOH has the highest olefin formation constant while EtOH has the lowest indicating C_α carbocation stability is the most important factor in determining olefin formation rates. In-

situ pyridine inhibition experiments show that the number of active sites for ether formation is the same irrespective of the carbon chain length and branching of the alcohol; this number is likely a function of reaction temperature. The quantitative assessment of rate and equilibrium parameters in this study enables the systematic assessment of carbon chain length and substitution as drivers for olefin selectivity in alcohol dehydration reactions that are useful both from an industrial perspective and as probe reactions for assessing the reactivity of metal oxide surfaces.

2.5. Supporting Information

2.5.1. Kinetics and mechanism of C_3-C_4 alcohol mono-alcohol dehydration at low alcohol pressure

The olefin formation rate under low alcohol pressure at 488 K showed less than negative one order dependence (<-1) on water partial pressures at high water pressure (>2 kPa) as represented in Figure 2.5 (1-PrOH partial pressure = 0.70 kPa, 2-PrOH partial pressure = 0.65 kPa, iBuOH partial pressure = 0.78 kPa, and water partial pressure = 0.33-6.3 kPa). This less than negative one order dependence on water indicates that water dimers exist and inhibit mono-alcohol dehydration at low alcohol pressures and high water pressures. The mechanism in Scheme 2.1 and Equation 2.2, therefore, explains the mono-alcohol dehydration at 488 K.

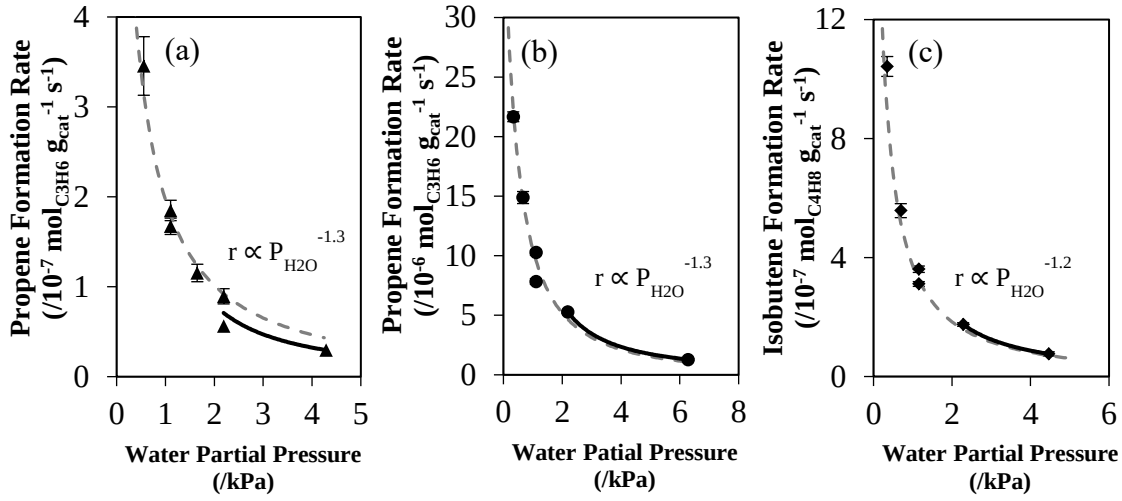

Figure 2.5 Olefin formation rate for (a) 1-PrOH, (b) 2-PrOH, and (c) iBuOH dehydration at 488K on γ-Al_2O_3 as a function of water partial pressure ((a) 0.55-4.3, (b) 0.33-6.3, and (c) 0.35-4.5 kPa) with 0.70 (▲), 0.65 (●), and 0.78 (◆) kPa alcohol co-feeds (total gas flowrate = 3.4 cm^3 s^{-1}). The dashed lines represent the model fits to Equation 2.2. Solid lines represent trendlines for high water pressure range (>2 kPa).

2.5.2. Kinetics and mechanism of ethanol mono-alcohol dehydration

The ethene formation rate when co-feeding EtOH and water at 488 K is shown in Figure 2.6 (EtOH partial pressure = 0.92-7.1 kPa; and water partial pressure = 0.41-2.3 kPa). The ethene formation rate decreased as water partial pressure increased. A positive dependence on EtOH at low EtOH partial pressures (<2 kPa) and high water partial pressures (>1.2 kPa) was observed. The reaction order in EtOH asymptotically lines out to zero at high water pressure (~2.3 kPa). These observations suggest mono-alcohol dehydration is inhibited by EtOH/water dimers on the surface. The less than negative one dependence of ethene formation rates on water partial pressure at low EtOH partial pressure (~1.1 kPa) and high water partial pressure (>1.7 kPa) as shown in Figure 2.6 (b) confirms

the existence of water dimers on the surface. The observed negative dependence of mono-alcohol dehydration rates on EtOH shows inhibition by EtOH dimers on the surface. EtOH monomers are expected to be involved in the rate-determining step of ethene synthesis. The dimer inhibition model discussed in Section 2.3.3.1 (Scheme 2.1 and Equation 2.2) describes the kinetics of EtOH mono-alcohol dehydration with the ethoxide species, EtOH/water dimers, EtOH dimers, and water dimers as dominant surface species. The parameters and the model fit of this equation are shown in Table 2.14 and Figure 2.6, respectively.

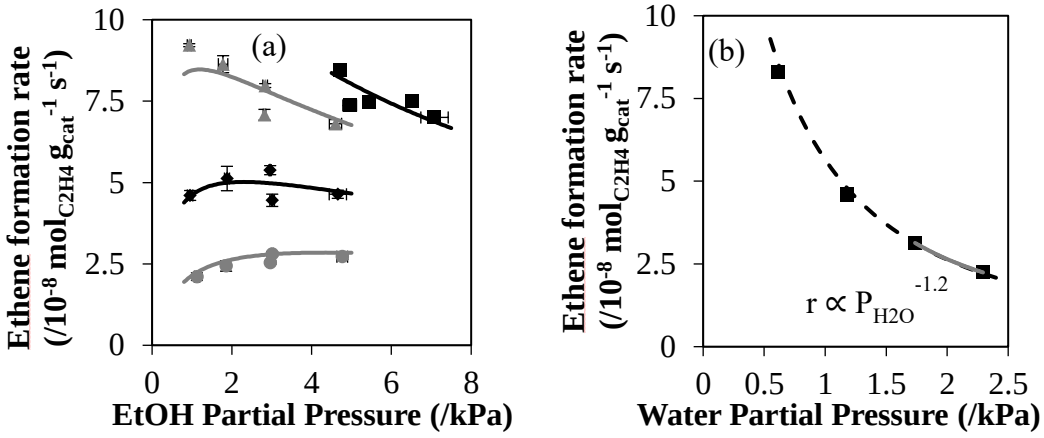

Figure 2.6 Ethene formation rate for EtOH dehydration at 488K on γ-Al_2O_3 (a) as a function of EtOH partial pressure with 0.41 (■), 0.62 (▲), 1.2 (◆), and 2.3 (●) kPa water co-feeds and (b) as a function of water partial pressure with 1.1 (■) kPa EtOH co-feeds (total gas flowrate = 3.4 cm^3 s^{-1}). The solid lines and dashed line represent the model fits to Equation 2.2 for (a) and (b), respectively. The solid line in (b) represents a trendline for high water pressure range (>1.7 kPa).

Table 2.14 Estimated kinetic parameters for mono-alcohol dehydration of EtOH on γ-Al_2O_3 at 488 K using the model presented in Equation 2.2 and data from Figure 2.6

Parameter	$k_{C_2H_4}$ ($/10^{-7}$ mol_{C2H4} g_{cat}^{-1} s^{-1})	$\frac{K'_{AW}}{K_{A1}K_d}$ ($/kPa^{-1}$)	$\frac{K_{A1}K_{A2}}{K_{A1}K_d}$ ($/kPa^{-1}$)	$\frac{K_{W1}K_{W2}}{K_{A1}K_d}$ ($/kPa^{-1}$)
Estimated Value	3.40 ± 1.03	3.48 ± 1.39	0.350 ± 0.143	1.29 ± 0.59

EtOH/water dimers and water dimers are dominant on the γ-Al_2O_3 surface compared to EtOH dimers at the conditions employed as inferred from the calculated values of adsorption parameters: $\frac{K'_{AW}}{K_{A1}K_d}$, 3.48, $\frac{K_{A1}K_{A2}}{K_{A1}K_d}$, 0.350, and $\frac{K_{W1}K_{W2}}{K_{A1}K_d}$, 1.29. The comparison of olefin rate constants with other alcohols is presented in Section 2.3.5.

2.5.3. Analysis of residual error in the kinetic models for C_3-C_4 alcohol dehydration

The proposed kinetic models in Equation 2.2 and 2.4 for olefin and ether formation reasonably fit with observed formation rates as shown in Figure 2.7. The residual errors of proposed models are randomly ordered and normally distributed as presented in Figure 2.8 and 2.9 except two points in DiPE formation (Figure 2.8 and 2.9 (e)) and one point in isobutene and DiBE formation (Figure 2.8 and 2.9 (c) and (f)) models. The deviation of these points indicates that a systematic error was present when these measurements were taken.

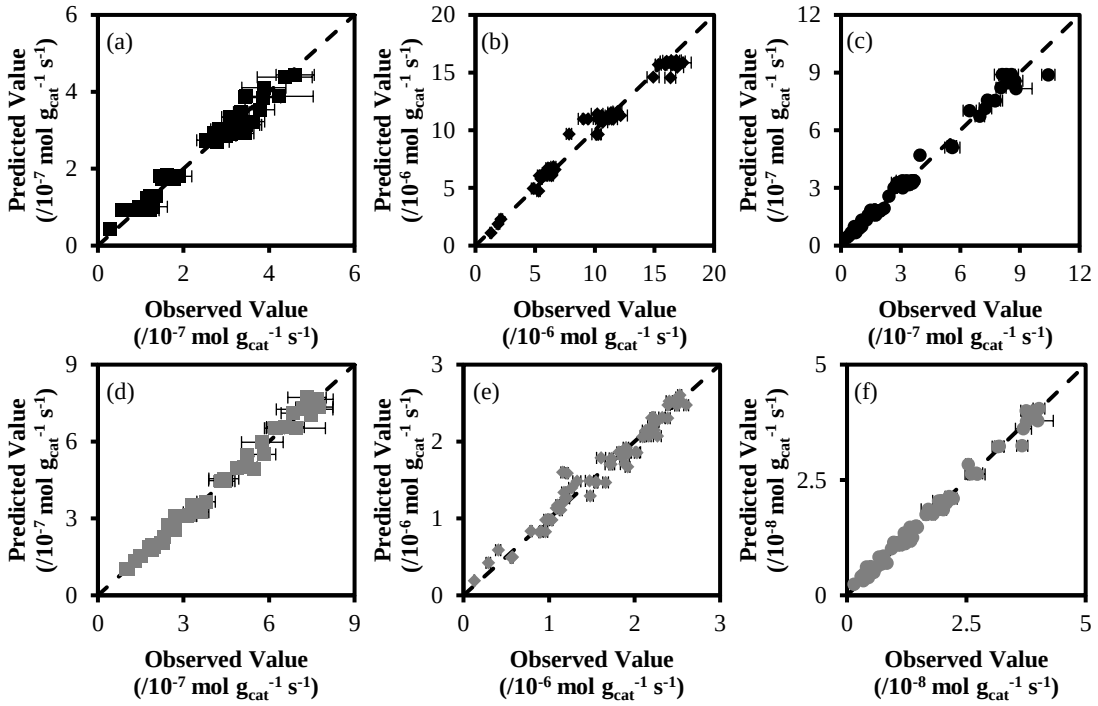

Figure 2.7 Parity plots for kinetic models for (a) propene from 1-PrOH, (b) propene from 2-PrOH, (c) isobutene, (d) DPE, (e) DiPE, and (f) DiBE formation rates in Equations 2.2 (a,b,c) and 2.4 (d,e,f) and data presented in Figures 2.1-3 at 488 K on γ-Al_2O_3. The dotted lines represent perfect prediction of the model.

The two deviant measurements in DiPE formation model were obtained under 0.6 kPa of 2-PrOH and 0.3 kPa of water. At these low alcohol and water partial pressures, the measured conversion was exceptionally high (>20 %), suggesting that the assumption that the packed bed reactor was differential may not hold for these data points and may result in a systematic error in the evaluated rates.

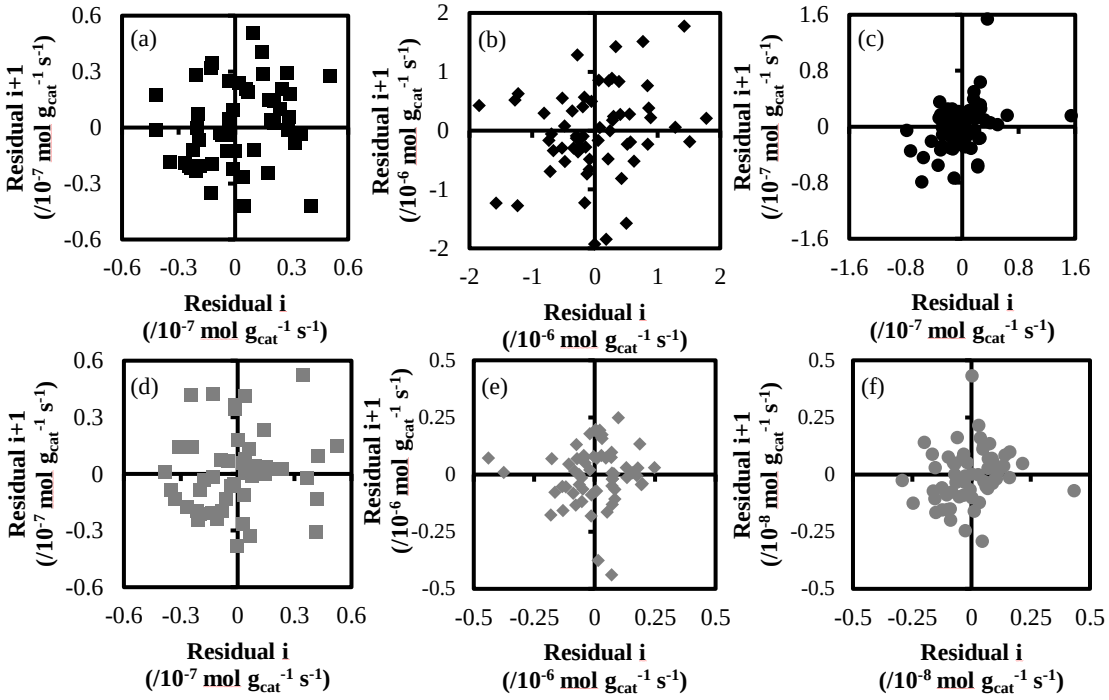

Figure 2.8 Lag plots for residual errors of kinetic models for (a) propene from 1-PrOH, (b) propene from 2-PrOH, (c) isobutene, (d) DPE, (e) DiPE, and (f) DiBE formation rates in Equations 2.2 (a,b,c) and 2.4 (d,e,f) compared to the data presented in Figures 2.1-3 at 488 K on γ-Al_2O_3.

The data points for isobutene and DiBE formation model that fell outside of a normal distribution were obtained from a single kinetic measurement at 0.8 kPa of iBuOH and 0.3 kPa of water, the lowest tested water partial pressure. At this low water partial pressure, the absolute fluctuations in water feed rate from the syringe pump correspond to a larger relative fluctuation in water feed rate than other data points. One possible explanation for the non-normal error for this measurement is that these fluctuations in water partial pressure and, thus, the dehydration rates were significantly different than the desired set-point.

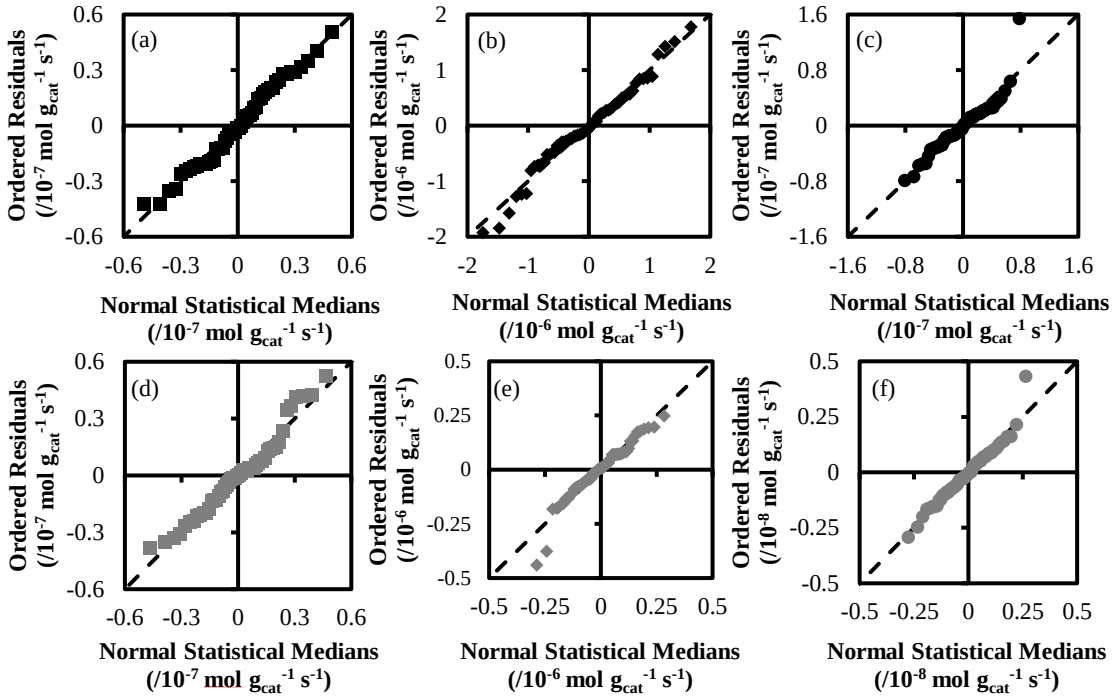

Figure 2.9 Normal probability plots for residual errors of kinetic models for (a) propene from 1-PrOH, (b) propene from 2-PrOH, (c) isobutene, (d) DPE, (e) DiPE, and (f) DiBE formation rates in Equations 2.2 (a,b,c) and 2.4 (d,e,f) relative to the data presented in Figures 2.1-3 at 488 K on γ-Al_2O_3. The dotted lines represent perfect normal distribution of the residual errors.

2.6. Acknowledgements

We appreciate financial support from The Dow Chemical Company. We also acknowledge Dr. Jeremy W. Bedard for helpful technical discussions.

3. Kinetics and mechanisms of alcohol dehydration pathways on alumina materials*

3.1. Introduction

Alumina is versatile material widely used in catalysis and adsorption[5,9,10]. Understanding the surface properties of alumina is important not only in itself but also for assessing the characteristics of other metal oxides which can be referenced from those of alumina[10]. Pursuant to this goal of developing an understanding of the surface structure, coordination, and hydroxylation of alumina materials, diffraction, electron microscopy, infrared (IR) and nuclear magnetic resonance (NMR) spectroscopies, calorimetry, and chemical titration have been extensively employed for characterization of alumina materials.

The diversity of alumina materials in terms of bulk structure is represented in the many polymorphs of alumina; these include high surface area transitional alumina materials such as γ-, δ-, θ-, η-, and χ-Al_2O_3 as well as structurally well-defined low surface area materials such as α-Al_2O_3[10]. Transitional alumina materials are usually produced from thermal treatment of alumina hydroxides or oxyhydroxides[29,62]. Electron microscopy has been used extensively to report that globular and plate-like morphologies are formed on γ-, δ-, θ-, η-, and χ-Al_2O_3[63–67] as well as to report that (100), (110), and (111) terminations are predominantly observed on γ-Al_2O_3[65,68]. Neutron and X-ray diffraction (XRD) and IR spectroscopy studies of γ-Al_2O_3 and η-Al_2O_3 have shown that they have similar bulk

*_Catal. Sci. Technol._, 2016, **6**, 6667-6678 – Reproduced by permission of The Royal Society of Chemistry

structure with defects in the bulk material as inferred from the broad peaks observed in XRD patterns[69,70]. ^{27}Al NMR spectra show that the fraction of octahedral occupancy of aluminum atoms, 0.75 and 0.65 for γ-Al_2O_3 and η-Al_2O_3, respectively, are different between the two materials[70,71]. More generally, these studies report on the diversity of surface termination and morphology existent in alumina materials which in turn has both mechanistic and kinetic consequences on alumina-catalyzed reactions as we discuss below.

A diversity of binding strengths and coordination and hydroxylation environments for sites on alumina materials has been established using probe molecule spectroscopic and computational chemistry studies. Knøzinger and co-workers early on proposed a surface structure model of alumina comprising surface hydroxyl groups and various coordination environments of aluminum atoms[35]. Specifically, they observed several IR bands in the 3500-3800 cm^{-1} stretching region attributed to OH groups and concomitantly[72] multiple IR adsorption bands (1614, 1617, and 1624 cm^{-1}) from pyridine-adsorbed on γ-Al_2O_3 samples. Ripmeester[32] made similar inferences based on chemical shifts at 110 and 138 ppm in ^{15}N-NMR spectra of pyridine-adsorbed γ-Al_2O_3. Morterra et al.[73] recorded IR spectra of η-Al_2O_3 samples exposed to CO_2 and noted vibrational bands corresponding to linear CO_2, carbonate, and bicarbonate surface species at 2370, 1800, and 1650 cm^{-1}, extending the inference of the observed site heterogeneity to other transitional alumina materials. Similar observations have also been reported based on using CO as a probe molecule, specifically, IR bands of CO adsorbed on α-, γ-, and δ-Al_2O_3 have been ascribed to 3-, 4-, and 5-fold coordinated Al^{3+} ions[74]. Along the same lines, computational chemistry based approaches have been used to suggest the diversity of surface sites on alumina materials. Sautet and

coworkers modeled the (100) and (110) surfaces of γ-Al_2O_3 with tri-, tetra-, and penta-coordinated aluminum surface atoms. Using DFT with the PW91 functional, these authors determined that the energy level of the lowest unoccupied state of surface aluminum atoms relative to vacuum varies between -2.5 and +0.1 eV, increasing with the coordination number of aluminum atoms[19]. Independently, they reported the adsorption energy of N_2 to increase with aluminum atom coordination (-41, -15, and -11 kJ mol^{-1} for three-, four-, and five-coordinated aluminum atoms, respectively)[37]. These studies suggest that sites with varying Lewis acidity exist on the surface of γ-Al_2O_3 and that less coordinated aluminum sites are more Lewis acidic.

Chemical titration has also shown a diversity of sites on alumina materials. Kwak et al.[75] employed ^{27}Al MAS NMR to study BaO-deposited γ-Al_2O_3 and observed that the intensity of the penta-coordinated Al^{3+} signal located at 23 ppm decreased proportionally as BaO loading increased while the signal for tetra- and octahedrally-coordinated Al^{3+} (60 and 0 ppm) did not decrease. The authors, therefore, concluded that BaO is a selective titrant for penta-coordinated Al^{3+}. In a subsequent study[38], they reported that the turnover frequency of methanol dehydration decreased monotonically as BaO loading on γ-Al_2O_3 increased up to 4 wt. % at which the methanol dehydration rate is negligible. Along the same lines, Phung et al.[76] reported that 1.1 atom Na^+ nm^{-2} loaded onto γ-Al_2O_3, corresponding to $1/15^{th}$ of the total surface coverage (calculated from the ionic radius of Na^+ and measured surface area, 200 m^2 g^{-1}), resulted in complete inhibition of ethanol conversion at 523 K. These reports demonstrate a method to characterize the surface of alumina materials using a chemical probe reaction combined with ex-situ titration.

Surface hydroxylation density in addition to surface termination and aluminum coordination has been reported to evolve upon thermal treatment. On both α-Al_2O_3 and γ-Al_2O_3, the heats of immersion of water increased from 400 to 1000 erg cm^{-2} and the number of surface hydroxyl groups decreased from 10^{15} to 10^{14} OH cm^{-2} as outgassing temperature of the water-exposed samples was increased from 373 to 873 K[77]. Digne et al.[19] in the above referenced calculations (DFT with PW91 functional) report that the surface hydroxyl coverage associated with the lowest surface energy drops monotonically from 13 to 0 OH nm^{-2} for the (100) facet as temperature is increased from 450 to 600 K and from 18 to 3 OH nm^{-2} for the (110) facet as temperature is increased from 400 to 1000 K. They also note that hydroxylation occurs on surface aluminum atoms changing the coordination of aluminum sites. In a subsequent publication, Sautet and coworkers[37] describe a monotonic increase in the adsorption energy of N_2 (-40 to -5 kJ mol^{-1}) on tri-coordinated Al sites with increasing surface hydroxyl group density (0-9 OH nm^{-2}) using the model proposed above. The authors also report on the basis of experimental measurements that N_2 adsorption on γ/δ-Al_2O_3 as a function of thermal pretreatment temperature (673-1273 K) has a maximum at 993 K. They used the IR band at 2355 cm^{-1} corresponding to the N-N stretching vibrational mode of N_2 adsorbed on tri-coordinated Al sites to measure the number of adsorbed N_2 molecules. These experimental observations in conjunction with the density functional theory based calculations reported by Sautet and coworkers discussed above lead them to conclude that the distribution of the coordination number of surface aluminum sites depends on the pretreatment temperature as a result of the change in the hydroxylation level of alumina on the surface. These studies elucidate the evolution of surface species

upon exposure to water and thermal treatment. In addition to the evolution of surface hydroxyl species and aluminum coordination, combined XRD and IR experiments performed by Kwak et al.[78] demonstrate that the surface structure also changes upon heating. In these experiments, the thermal treatment of γ-Al_2O_3 at 1073 K for 2 hours did not change its bulk structure as inferred from the unchanged XRD patterns of thermally-treated and untreated γ-Al_2O_3, but the thermally-treated γ-Al_2O_3 displayed ethanol temperature desorption profiles similar to θ-Al_2O_3 samples (desorption occurred at 523 K instead of 498 K for uncalcined γ-Al_2O_3). The authors posit that the surface of heated γ-Al_2O_3 evolves to that of θ-Al_2O_3 before the bulk structure changes.

Alcohol dehydration on alumina catalysts has been thoroughly studied for over fifty years[21,22,33,34,38,42,45,76,79–91]. To summarize the literature: (i) kinetic isotope and computational chemistry investigations support a dehydration mechanism and rate limiting step to be an E2-type mechanism and C_β-H bond cleavage for olefin formation, (ii) similarly, an S_N2-type mechanism with C-O bond cleavage is concluded to be the rate limiting step for ether formation, and (iii) steady state kinetic rate measurements and density functional theory based calculations have demonstrated that water inhibits both mono- and di-alcohol dehydration. Previously we reported[11,43,58,92] that mono- and di-ethanol dehydration are inhibited differently by pyridine on γ-Al_2O_3, which showed ~70% and ~30% decrease, respectively, with 3.5 kPa of ethanol, 1.3 kPa of water, and 0.05 kPa of pyridine at 623 K. The introduction of 2.2 kPa of water to a γ-Al_2O_3 sample for 1 hour prior to the reaction also resulted in ~60% and ~30% decrease in olefin and ether formation rates, respectively, from ethanol dehydration at 488 K. The dissimilar inhibition of mono-

and di-alcohol dehydration rates by both pyridine and water was also observed for other aliphatic alcohols suggesting the existence of at least two pools of sites on γ-Al_2O_3. Vlachos and co-workers[34,87] calculated activation energies of both mono- and di-ethanol dehydration on (100), (110), and (111) facets of γ-Al_2O_3 using DFT and determined activation energy barriers of ethene formation to be 37, 30, and 28 kcal/mol on (100), (110), and (111) surface facets, respectively; the calculated barriers for DEE synthesis were 34, 35, and 32 kcal/mol on (100), (110), and (111) surface facets, respectively. These calculations also suggest that the diversity of surface termination and hydroxylation on alumina materials results in sites which preferentially catalyze mono- or di-alcohol dehydration pathways.

Here, we report (i) separate pools of sites that catalyze mono- and di-alcohol dehydration also exist on η- and α-Al_2O_3 and are likely to exist on all alumina materials; (ii) the mechanistic pathways that lead to ethene and DEE in parallel dehydration reactions are identical on all alumina materials; (iii) the number of sites per surface area as assessed by in-situ pyridine chemical titration for transitional alumina materials are similar. The in-situ chemical titration protocols used in this research do not probe the structure of the active site, however, in contrast with ex-situ structural and chemical characterization probes, they allow us to probe the evolution in structure and function of alumina materials under reaction conditions.

3.2. Materials and Methods

3.2.1. Catalyst preparation and characterization

α-Al_2O_3 in powder form was synthesized by heating γ-Al_2O_3 powder (Sasol Catalox 18 HPA-150) with flowing dry air (1.7 cm^3 s^{-1} at NTP conditions, Minneapolis Oxygen) from ambient temperature to 1423 K at 0.026 K s^{-1} and held at 1423 K for 40 h. The synthesized powder was analyzed by X-ray diffraction (XRD) analysis to verify α-Al_2O_3 synthesis. The XRD analysis was conducted on a Bruker-AXS Microdiffractometer with Cu K(α) radiation (1.54 Å) in step mode with a step size of 0.04°/s (2θ in the range 10-80°). Commercially available γ-Al_2O_3 (Sasol Catalox 18 HPA-150) and η-Al_2O_3 (United Catalysts (Clariant)) powders were used. Brunauer-Emmet-Teller (BET) surface areas of α-, γ-, and η-Al_2O_3 powder were measured using N_2 adsorption/desorption at 77 K with a Micromeritics ASAP 2020.

The powders of α-, γ-, and η-Al_2O_3 were compressed and sieved to gain catalyst particles between 180 and 250 μm (60-80 mesh). The catalyst beds were formed by mixing catalysts (1.3-25.7 mg) and acid-washed quartz sand in a quartz tube packed bed reactor and were thermally treated while flowing dry air (1.7 cm^3 s^{-1} at NTP conditions) by heating from ambient temperature to 723 K at 0.015 K s^{-1} and being retained at 723 K for 4 h. The catalyst bed was cooled to reaction temperatures of 573 or 623 K in air flow and subsequently exposed to 2.2 kPa of water in helium (1.7 cm^3 s^{-1} at NTP conditions, Minneapolis Oxygen) for 1 h before the reaction.

3.2.2. Steady-state kinetic measurements of ethanol dehydration

The prepared alumina materials were used to conduct steady-state ethanol dehydration reactions under atmospheric pressure and differential conversion conditions (<10%). A tube furnace (National Electric Furnace FA120 type) and a Watlow temperature controller (96 series) were used to maintain reaction temperatures of 573 and 623 K while measuring reactor temperature with a type K thermocouple located on the external surface of the reactor. Liquid ethanol (Decon Labs, Inc., 0.4-8.7 kPa) and deionized water (0.6-2.2 kPa) were co-fed using two separate infusion syringe pumps (KDS100) and vaporized into a stream of helium (3.4-6.3 cm^3 s^{-1} at NTP conditions) and an internal standard mixture for gas chromatographic (GC) analysis comprising Ar/CH_4 (10.0% CH_4 and Ar balance, 0.15 cm^3 s^{-1} at NTP conditions, Matheson Trigas). Resistively heated gas lines keeping temperatures above 343 K were employed to avoid condensation of liquids.

The reactor effluent was analyzed using both an online GC (Agilent 6890 N, flame ionization detector with Agilent Plot-Q column) and an online mass spectrometer (MKS Cirrus 200 quadrupole, MS). Reported error bars in figures below describe 95% confidence intervals using successive GC injections under the same experimental conditions.

3.2.3. In-situ pyridine titration of catalytic sites responsible for ethanol dehydration

Ethanol (2.2 kPa) and water (1.0 kPa) with flowing He were co-fed to the catalyst bed (~10 mg) at 573 K. Pyridine (>99%, Sigma-Aldrich, 0.02-0.10 kPa) was introduced to the reactant flow (3.4 cm^3 s^{-1} at NTP conditions) after observing steady-state rates of

dehydration. The observed effluent composition was analyzed to estimate the pyridine uptake required to completely deactivate ethanol dehydration using linear extrapolation as described in Section 3.3.2.1.2.

3.2.4. Estimation of kinetic parameters

Reported kinetic parameters were optimized using Bayesian statistical estimation techniques in the Athena Visual Studio (v14.2, W.E. Steward and M. Caracotsios). The 95% marginal highest posterior density intervals were used as the reported uncertainties. The experimental measurements under the same ethanol and water pressure were defined as replicates.

3.3. Results and discussion

3.3.1. Structural characterization of alumina materials

The crystalline characteristics of alumina materials were verified using powder X-ray diffraction. Figure 3.1 shows the XRD patterns of α-, γ-, and η-Al_2O_3 as well as reference patterns for each of these materials (JCPDS 01-075-1862, JCPDS 00-001-1303, and ICDD n^0 21-0010, respectively). The close agreement between the measured diffraction patterns for the materials used in this research with the reference materials reported in the crystallographic database leads us to conclude that bulk structures of the materials used in this research closely resemble α-, γ-, and η-Al_2O_3.

The porous characteristics of the alumina materials used in this research were assessed based on N_2 adsorption isotherms per the procedure described in Section 3.2.1. The BET surface area of the materials used in this research are: 7.3, 141, and 360 $m^2\ g^{-1}$

for α-, γ-, and η-Al_2O_3, respectively; these values are in the range of those reported for similar materials (α-Al_2O_3 : <50 m^2 g^{-1}, γ-Al_2O_3 : 100-500 m^2 g^{-1}, and η -Al_2O_3 : <430 m^2 g^{-1})[10,93–96].

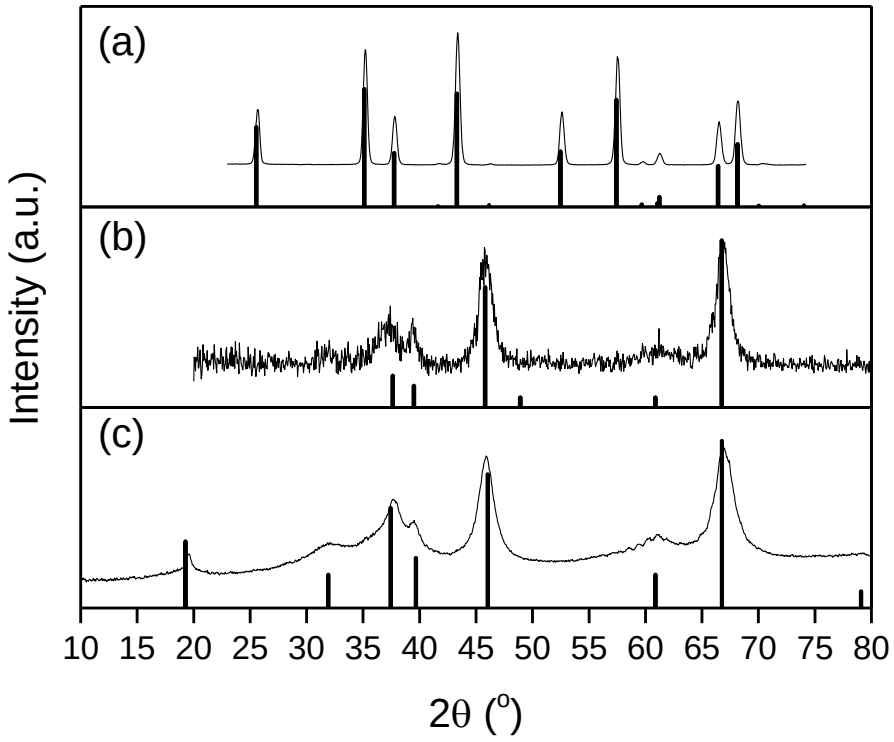

Figure 3.1 XRD patterns of (a) synthesized α-Al_2O_3 (solid line) and reference α-Al_2O_3 (bar, JCPDS 01-075-1862), (b) γ-Al_2O_3 (solid line) and reference γ-Al_2O_3 (bar, JCPDS 00-001-1303), and (c) η-Al_2O_3 (solid line) and reference η-Al_2O_3 (bar, ICDD n^0 21-0010)

Powder XRD patterns and BET surface area measurements confirm the structural characteristics of the three different alumina materials used in this research. The morphology of each alumina is also different as shown in SEM images reported in

supporting information, Figure 3.6. We focus on the different catalytic properties of alumina polymorphs resulting from the variation in their bulk and surface structures.

3.3.2. Kinetics, mechanism, and site densities of ethanol dehydration on different aluminas

The kinetics of parallel mono- and di-alcohol dehydration mechanisms were assessed by measuring rates of ethanol dehydration at different ethanol and water partial pressures under differential conversion (<10%).

3.3.2.1. Kinetics, mechanism, and site densities of mono-ethanol dehydration on different alumina materials

3.3.2.1.1. Reaction kinetics of mono-ethanol dehydration at 573 and 623 K

Ethene synthesis rates increase as ethanol pressure increases while co-feeding ethanol and water at 573 K on all alumina catalysts tested, as shown in Figure 3.2 (Ethanol partial pressure in the range 0.4-8.5 kPa and water partial pressure in the range 0.6-2.2 kPa). An increase in water partial pressure results in a decrease of the ethene formation rate on all alumina catalysts tested in this research suggesting that co-adsorption of water inhibits mono-alcohol dehydration. The inhibiting effect of water has been also reported previously for alcohol dehydration on γ-Al_2O_3, ZrO_2, and TiO_2[17,21,33,34,85,87,88]. The ethene synthesis rate asymptotically lines out at high ethanol pressure (~5 kPa), suggesting that ethanol-water dimer species exist under reaction conditions. We infer the dominating surface-adsorbed species as ethanol monomers, water monomers, and ethanol-water dimers from the observed pressure dependency of ethene formation rates on ethanol and water partial

pressure which is noted to be independent of the alumina polymorph type. Ethanol monomers are involved in the rate determining step - cleavage of the C_β-H bond[11,42,43,46]. A physisorbed molecularly intact ethanol-species reacting in an E2-type mechanism or a chemisorbed alkoxide derived from ethanol reacting via an E1-type mechanism are kinetically indistinguishable as reactive precursors to form ethene. Knözinger and Scheglila[42] proposed an E2-type mechanism for mono-alcohol dehydration on γ-Al_2O_3 involving concerted cleavage of the C_β-H and C-OH bond and recent DFT calculations have shown lower barriers for an E2-type mechanism for Lewis-acid catalyzed mono-alcohol dehydration[17,33,34,85,87–89,97]. Based on these reports, we consider an E2-type mechanism for ethene formation; however, we note that independent of the detailed mechanistic pathways, the rate expression shown in Equation 3.1 rigorously describes the measured kinetics of mono-ethanol dehydration at 573 K on α-, γ-, and η-Al_2O_3.

$$r_{ethene} = \frac{k_{ethene} P_{alcohol}}{P_{alcohol} + \frac{K_{W1}}{K_A} P_{water} + \frac{K_{AW}}{K_A} P_{alcohol} P_{water}} \quad (3.1)$$

k_{ethene} in Equation 3.1 above is the rate constant of the rate limiting step while K_A, K_{W1}, and K_{AW} are equilibrium constants for the adsorption of alcohol monomers, water monomers, and alcohol-water dimers, respectively, on the surface of alumina catalysts. Kinetic and equilibrium constants depicted in Equation 3.1 were estimated and optimized using Bayesian statistical estimation techniques in the Athena Visual Studio (v14.2, W.E. Stewart and M. Caracotsios) and tabulated in Table 3.1.

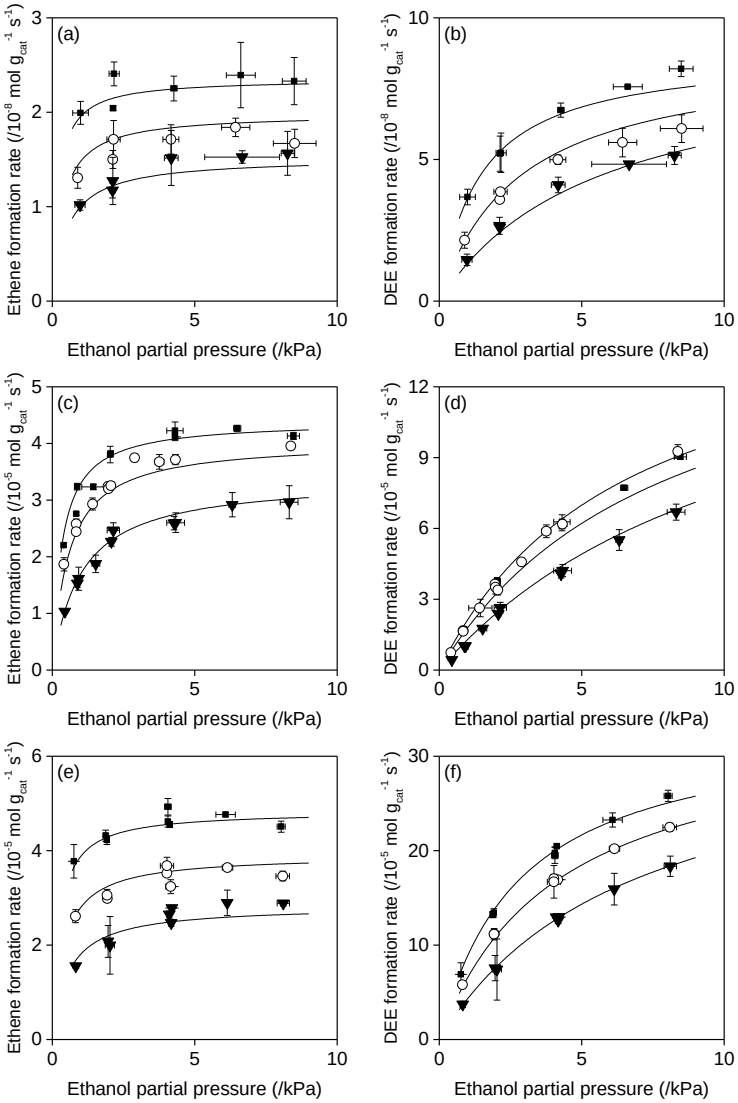

Figure 3.2 (a,c,e) Ethene and (b,d,f) DEE formation rates for ethanol dehydration at 573 K on (a),(b) 25.7 mg of α-Al_2O_3, (c),(d) 2.7 mg of γ-Al_2O_3, and (e),(f) 2.3 mg η-Al_2O_3 as a function of ethanol partial pressure with (■) 0.6 kPa, (○) 1.1 kPa, and (▼) 2.2 kPa of water partial pressure. The solid line represents the model fits to Equations 3.1 and 3.4 for (a,c,e) and (b,d,f), respectively.

Table 3.1 Estimated kinetic parameters for mono-alcohol dehydration of ethanol on α-, γ-, and η-Al_2O_3 at 573 K using the model presented in Equation 3.1 and data from Figure 3.2.

	k_{ethene} (/mol g_{cat}^{-1} s^{-1})	k_{ethene} (/10^{-7} mol m^{-2} s^{-1})	k_{ethene} (mol_{ethene} mol_{sites}^{-1} s^{-1})	$\frac{K_{W1}}{K_A}$	$\frac{K_{AW}}{K_A}$ (/kPa^{-1})
α-Al_2O_3	(2.9 ± 0.3) x 10^{-8}	0.039 ± 0.004	N/A	0.45 ± 0.25	0.41 ± 0.19
γ-Al_2O_3	(4.9 ± 0.3) x 10^{-5}	3.5 ± 0.2	1.8 ± 0.1	0.63 ± 0.11	0.20 ± 0.08
η-Al_2O_3	(6.4 ± 0.5) x 10^{-5}	1.8 ± 0.1	1.6 ± 0.1	0.58 ± 0.19	0.57 ± 0.14

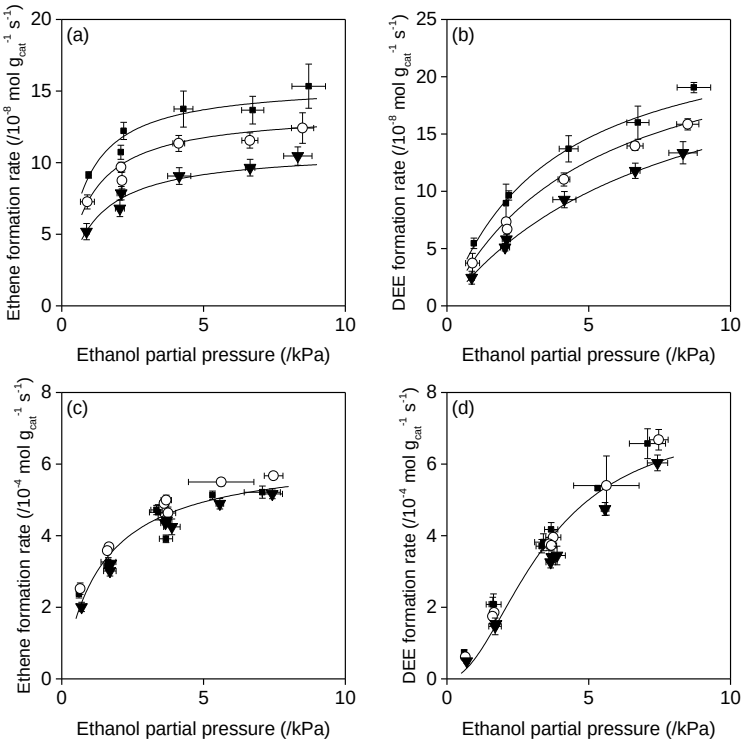

Figure 3.3 (a,c) Ethene and (b,d) DEE formation rates for ethanol dehydration at 623 K on (a),(b) 20.1 mg of α-Al_2O_3 and (c),(d) 1.9 mg of η-Al_2O_3 as a function of ethanol partial pressure with (■) 0.6 kPa, (○) 1.1 kPa, and (▼) 2.2 kPa of water partial pressure. The solid line represents the model fits to Equations 3.2, 3.4, 3.3, and 3.5 for (a), (b), (c), and (d), respectively.

Table 3.2 Estimated kinetic parameters for mono-alcohol dehydration of ethanol on α-Al_2O_3 at 623 K using the model presented in Equation 3.2 and data from Figure 3.3.

	k_{ethene} (/10^{-8} mol g_{cat}^{-1} s^{-1})	k_{ethene} (/10^{-8} mol m^{-2} s^{-1})	K_A(/kPa^{-1})	K_{W1} (/kPa^{-1})	K_{AW} (/kPa^{-2})
α-Al_2O_3	18 ± 1	2.5 ± 0.2	1.8 ± 0.9	0.88 ± 0.73	0.57± 0.16

Table 3.3 Estimated kinetic parameters for mono-alcohol dehydration of ethanol on γ- and η-Al_2O_3 at 623 K using the model presented in Equation 3.3 and data from Figure 3.3.

	k_{ethene}(/10^{-4} mol g_{cat}^{-1} s^{-1})	k_{ethene}(/10^{-6} mol m^{-2} s^{-1})	K_A(/kPa^{-1})
γ-Al_2O_3[a]	9.4 ± 3.3	6.7 ± 2.3	0.22 ± 0.17
η-Al_2O_3	6.3 ± 0.3	1.7 ± 0.1	0.73 ± 0.10

[a] From reference 58

The rates of mono-ethanol dehydration on α- and η-Al_2O_3 at 623 K with ethanol and water co-feed (Ethanol partial pressure = 0.4-8.5 kPa and water partial pressure = 0.6-2.2 kPa) are shown in Figure 3.3. Ethene synthesis rates on α-Al_2O_3 at 623 K show the same pressure dependences on ethanol and water pressure as those at 573 K; reaction rates for ethene synthesis decreased with increasing water pressure and asymptotically lined out at higher ethanol pressures. The same dominant surface-adsorbed species are involved in the mechanistic pathway for ethene formation on α-Al_2O_3 at 623 K except that a term corresponding to vacant surface sites is kinetically-relevant at 623 K as compared to 573 K because of less stable surface-adsorbed species at the higher 623 K temperature. The rate expression for ethene formation on α-Al_2O_3 is shown in Equation 3.2. The corresponding

kinetic and thermodynamic equilibrium constants estimated by Bayesian statistical estimation techniques are tabulated in Table 3.2.

$$r_{ethene} = \frac{k_{ethene} K_A P_{alcohol}}{1 + K_A P_{alcohol} + K_{W1} P_{water} + K_{AW} P_{alcohol} P_{water}} \quad (3.2)$$

The parameters in this equation have the same physical meaning as the parameters in Equation 3.1. Ethene formation rates on η-Al_2O_3 at 623 K also increase as ethanol pressure increases but are independent of water pressure similar to what was noted for ethene synthesis rates on γ-Al_2O_3 at 623 K reported in our previous work[58]. Equation 3.3 represents the rate expression for ethene synthesis on both γ- and η-Al_2O_3 with the same nomenclature of parameters as in Equations 3.1 and 3.2. The kinetic and thermodynamic parameters assessed using the model shown in Equation 3.3 are tabulated in Table 3.3.

$$r_{ethene} = \frac{k_{ethene} K_A P_{alcohol}}{1 + K_A P_{alcohol}} \quad (3.3)$$

The rate expression reported in Equations 3.1-3 is identical to what we have previously reported on γ-Al_2O_3 except for the predominant prevalence of monomeric surface-adsorbed species at 623 K and dimeric species at 488 K[11,43,58]. We can infer that dimeric surface-adsorbed species exist and are stable at 573 K but do not dominate the surface as they do at 488 K. At 623 K, dimeric surface-adsorbed species are still present on α-Al_2O_3 and are not present in kinetically-significant concentrations on γ- and η-Al_2O_3. A common rate expression describes the observed pressure dependencies and quantitatively describes the observed rates of ethene synthesis on all alumina materials across a wide range of temperatures (573-623 K for α- and η-Al_2O_3, 488-673 K for γ-

Al_2O_3). The existence and kinetic involvement of monomeric and multimeric adsorbate complexes (of alcohol and water) at different temperatures can be inferred from a mechanistic assessment of the observed pressure dependences of reaction rates and the corresponding mathematical formulation of this mechanism in the form of a reaction rate expression. Very recently, Larmier et al.[98] also proposed that coadsorbed water and alcohol molecules such as alcohol dimers, alcohol-water dimers, and alcohol dimer-water monomer trimers, influence parallel mono- and di-2-propanol dehydration pathways on γ-Al_2O_3. The authors develop a multi-scale kinetic model accounting for alcohol dehydration and ether decomposition pathways incorporating adsorption/desorption energies from DFT + D2 calculations and report that multimeric surface species on the active sites on (100) surface facet of γ-Al_2O_3 occupy greater than 10% of the macro sites on the catalytic surface under catalytic conditions. Fang et al.[85] discuss the reactions of mono- and di-ethanol with water on an Al_8O_{12} cluster as a model for γ-Al_2O_3 using correlated molecular orbital theory at the coupled cluster CCSD(T) level with DFT geometries and concluded that the addition of a second ethanol or water molecule increases the energy barrier for ethanol dehydration reactions. In conjunction with prior computational chemistry studies[34,86,87,98], the recent study by Fang et al.[85] using *ab initio* methods also suggest that multimeric surface intermediates are likely to exist at catalytic conditions relevant for ethanol dehydration on γ-Al_2O_3 and these intermediates inhibit dehydration rates. Computational chemistry studies on other metal oxides (WO_3 and MoO_3) also show the involvement of alcohol dimer species in reactions suggesting that this observation is broadly applicable to metal oxides[99,100].

The existence of analogous surface sites on all alumina catalysts can be inferred from the similarity of the observed pressure dependences and the commonality of the underlying mechanism and resulting rate expression for ethene formation. In a recent report, Hu et al.[101] noted that γ-Al_2O_3 samples treated at different temperatures (773-1373 K) result in various polymorphs of alumina (γ-, δ-, θ-, and α-Al_2O_3 and their mixtures). The number of penta-coordinated Al^{3+} ions on these samples using high field ^{27}Al MAS NMR and the amount of dissociatively adsorbed ethanol which is converted to ethene during ethanol TPD experiments correlated in a one-to-one ratio on all samples. This observation led the authors to propose that penta-coordinated Al^{3+} ions on the surface of alumina catalysts are the primary active sites for mono-ethanol dehydration. Larmier et al.[97] had previously proposed penta-coordinated aluminum on the (100) surface facet of γ-Al_2O_3 as the active site for 2-propanol dehydration by showing lower activation barriers for dehydration compared to those on tetra-coordinated aluminum on the (110) surface facet using computational chemistry. Based on an assessment of the temperature variation of the initial rate of propene synthesis and diisopropyl ether synthesis on γ- and δ-Al_2O_3 at 433-483 K, the authors also reported activation barriers to be the same on the two alumina materials within experimental error and inferred that similar active sites exist on the two alumina materials.

The different kinetic and thermodynamic parameters assessed from steady state kinetic measurements (Tables 3.1-3) on α-, γ-, and η-Al_2O_3 suggest that each alumina material has a distinct distribution of surface species originating from their distinct surface termination and morphology. The nearly five-fold variation (0.9-4.7 x 10^{-4} mol g^{-1}) in the

amount of penta-coordinated Al^{3+} ions on thermally treated γ-Al_2O_3 samples at temperatures from 773 to 1373 K from the report by Hu et al.[101] mentioned above supports this conclusion. Larmier et al.[97] also suggested that the observed lower 2-propanol conversion rate on δ-Al_2O_3 compared to γ-Al_2O_3 at 473 K is a consequence of a different ratio of (100)/(110) surface facets. The results presented in Tables 3.1-3 show that α-Al_2O_3 has a lower ethene formation rate constant normalized per surface area compared to γ- and η-Al_2O_3 demonstrating a lower surface density of ethene formation sites on α-Al_2O_3 compared to high-surface area alumina polymorphs tested in this report. In crystalline α-Al_2O_3, most aluminum ions are in six-fold coordination[10] and consequently α-Al_2O_3 materials will have a low density of five-fold-coordinated aluminum atoms suggested as active sites for ethene formation[101]. The reaction rate constants for ethene formation on γ- and η-Al_2O_3 are of the same order of magnitude suggesting that they have similar surface characteristics.

3.3.2.1.2. Site densities of mono-ethanol dehydration on different alumina materials at 573 K

The number of catalytic centers prevalent during ethanol dehydration on the different alumina materials were determined by in-situ titration of ethene synthesis rates using pyridine as a chemical probe. This analysis considers each pyridine molecule to titrate one active site, these active sites to be identical, and pyridine concentration in the bed to have a sharp front which moves with time from the beginning to the end of bed. This allows us to calculate the pyridine uptake required to completely inhibit ethene synthesis by extrapolating the linear decrease in ethene formation rate upon the initial adsorption of

pyridine (An example is shown in Figure 3.7). The site densities for ethene synthesis on γ- and η-Al_2O_3 at 573 K are tabulated in Table 3.4 (see Table 3.8 and 3.9 for data from independent titrations at different pyridine partial pressures). The two transitional alumina materials have similar site densities for ethene formation, which may result either from the similarity in their bulk and surface structure and its evolution under reaction environments or from a surface layer termination of the two materials which is similar under these conditions[10]. The site density for ethene formation on γ-Al_2O_3 at 573 K is ~0.12 sites nm^{-2}; this number is in good agreement with the density of penta-coordinated surface aluminum sites on γ-Al_2O_3, 0.22-0.26 sites nm^{-2}, measured by the high field ^{27}Al MAS NMR[101]. The rate constants normalized per active site using site densities determined by pyridine titration at 573 K are reported in Table 3.1. The results in Table 3.1 show that the rate constants normalized per site for γ- and η-Al_2O_3 are nearly identical suggesting that similar active sites exist on these two alumina materials as has also been suggested by Hu et al.[101] from TPD studies and Larmier et al.[97] from DFT + D2 studies. Similar observations regarding site densities and kinetic rate parameters were also noted for DEE synthesis on γ- and η-Al_2O_3 (Section 3.3.2.2.2).

Table 3.4 Number of catalytic sites for ethene and DEE formation from parallel ethanol dehydration on ~10 mg of γ- and η-Al_2O_3 at 573 K with 2.2 kPa of ethanol and 1.0 kPa of water partial pressure assessed using in-situ pyridine titration[a].

	Ethene		DEE	
	Pyridine Uptake ($/10^{-5}$ mol g^{-1})	Sites per surface area ($/nm^{-2}$)	Pyridine Uptake ($/10^{-5}$ mol g^{-1})	Sites per surface area ($/nm^{-2}$)
γ-Al_2O_3	2.7 ± 0.3	0.12 ± 0.01	3.2 ± 0.7	0.14 ± 0.03
η-Al_2O_3	4.0 ± 0.7	0.066 ± 0.011	5.4 ± 1.0	0.090 ± 0.017

[a] The 95% confidence intervals were determined based on independent titrations.

3.3.2.2. Kinetics, mechanism, and site densities of di-ethanol dehydration on different alumina materials

3.3.2.2.1. Reaction kinetics of di-ethanol dehydration at 573 and 623 K

DEE synthesis rates increase with increasing ethanol pressure when co-feeding ethanol and water at 573 K on α-, γ-, and η-Al_2O_3 as shown in Figure 3.2 (Ethanol partial pressure = 0.4-8.5 kPa and water partial pressure = 0.6-2.2 kPa). DEE formation rates decrease when water pressure increases suggesting that water co-adsorption on the alumina catalyst surface inhibits DEE synthesis similar to what was noted above for ethene formation. Previously, we have reported that this water inhibition arises primarily due to the existence of water-ethanol dimers[11,43]. The positive dependency of di-ethanol dehydration reaction rates on ethanol partial pressure and near-asymptotic behavior of DEE rates at higher ethanol pressures can be explained by the co-existence of surface ethanol monomers and ethanol dimers. Consistent with our prior reports for alcohol dehydration on γ-Al_2O_3, the dominant surface species are inferred to be ethanol dimers, ethanol

monomers, and ethanol-water dimers. The dominant surface species for DEE formation are common for all alumina catalysts tested in this report as noted for ethene synthesis kinetics discussed in Section 3.3.2.1.1 above. Following the proposed S_N2-type mechanism for DEE formation[34,43,44,85,87,97] and consistent with the measured pressure dependencies of DEE formation rates on water and ethanol at 573 K on all alumina catalysts, the kinetics of DEE formation are described by the rate expression in Equation 3.4.

$$r_{DEE} = \frac{k_{DEE} P_{alcohol}^2}{P_{alcohol}^2 + \frac{K_{A1}}{K_{A2}} P_{alcohol} + \frac{K_{AW}}{K_{A2}} P_{alcohol} P_{water}} \quad (3.4)$$

k_{DEE} in Equation 3.4 is the rate constant of the rate determining step of DEE formation and K_{A1}, K_{A2}, and K_{AW} represent equilibrium constants for adsorption of an alcohol monomer, alcohol dimer, and alcohol-water dimer, respectively. The non-linear parameter estimation technique discussed above was used to estimate the kinetic and equilibrium parameters in Equation 3.4 which are presented in Table 3.5.

Table 3.5 Estimated kinetic parameters for di-alcohol dehydration of ethanol on α-, γ-, and η-Al_2O_3 at 573 K using the model presented in Equation 3.4 and data from Figure 3.2.

	k'_{DEE} (/mol g_{cat}^{-1} s^{-1})	k'_{DEE} (/10^{-7} mol m^{-2} s^{-1})	k'_{DEE} (mol_{DEE} mol_{sites}^{-1} s^{-1})	$\frac{K_{A1}}{K_{A2}}$ (/kPa)	$\frac{K_{AW}}{K_{A2}}$
α-Al_2O_3	(8.8 ± 0.6) x 10^{-8}	0.12 ± 0.01	N/A	N/A or 0	2.5 ± 0.5
γ-Al_2O_3	(16 ± 2) x 10^{-5}	11 ± 1	5.0 ± 0.7	4.8 ± 1.5	2.9 ± 0.8
η-Al_2O_3	(34 ± 1) x 10^{-5}	9.4 ± 0.3	6.3 ± 0.2	1.4 ± 0.2	2.4 ± 0.2

The di-ethanol dehydration rates on α- and η-Al_2O_3 at 623 K are shown in Figure 3.3. The DEE synthesis rates on α-Al_2O_3 at 623 K increase with ethanol pressure and decrease with water pressure. The pressure dependencies and consequently the rate expression (Equation 3.4) and dominant surface species for DEE formation on α-Al_2O_3 are unchanged when comparing reaction rates at 573 K and 623 K. Kinetic and equilibrium constants for the DEE synthesis on α-Al_2O_3 at 623 K using the rate expression shown in Equation 3.4 are tabulated in Table 3.6. DEE formation rates on η-Al_2O_3 at 623 K are independent of water pressure and increase with ethanol pressure. This behavior is identical to that we had reported previously for di-ethanol dehydration rates on γ-Al_2O_3 at 623 K[58]. The rate expression for DEE synthesis on both γ- and η-Al_2O_3 at 623 K is illustrated in Equation 3.5 and the relevant kinetic and equilibrium constants are shown in Table 3.7.

$$r_{DEE} = \frac{k_{DEE} K_{A1} K_{A2} P_{alcohol}^2}{1 + K_{A1} K_{A2} P_{alcohol}^2} \quad (3.5)$$

Table 3.6 Estimated kinetic parameters for di-alcohol dehydration of ethanol on α-Al_2O_3 at 623 K using the model presented in Equation 3.4 and data from Figure 3.3.

	k'_{DEE} (/10^{-8} mol g_{cat}^{-1} s^{-1})	k'_{DEE} (/10^{-8} mol m^{-2} s^{-1})	$\frac{K_{A1}}{K_{A2}}$ (/kPa)	$\frac{K_{AW}}{K_{A2}}$
α-Al_2O_3	25 ± 1	3.5 ± 0.1	2.3 ± 0.3	2.5 ± 0.2

The only distinguishing factor between the rate expressions shown in Equations 3.4 and 3.5 is the prevalence and kinetic relevance of alcohol monomer and alcohol-water dimer species. Previously, we have discussed that the most general rate expression for di-alcohol dehydration would include monomeric, dimeric, and even trimeric terms for

alcohol and water-derived surface species[11]. Therefore, the rate expressions shown in Equations 3.4 and 3.5 represent particular manifestations of this more general rate expression and do not suggest mechanistic differences amongst the different alumina materials for alcohol dehydration pathways.

Table 3.7 Estimated kinetic parameters for di-alcohol dehydration of ethanol on γ- and η-Al_2O_3 at 623 K using the model presented in Equation 3.5 and data from Figure 3.3.

	k_{DEE} (/10^{-4} mol g_{cat}^{-1} s^{-1})	k_{DEE} (/10^{-6} mol m^{-2} s^{-1})	$K_{A1}K_{A2}$
γ-Al_2O_3[a]	6.8 ± 1.2	4.8 ± 0.9	0.021 ± 0.009
η-Al_2O_3	7.3 ± 0.4	2.0 ± 0.1	0.086 ± 0.013

[a] From reference 58

The same mechanism of DEE formation on α-, γ-, and η-Al_2O_3 implies the existence of common sites on all alumina catalysts similar to what was noted for ethene synthesis. The different kinetic and equilibrium parameters of DEE formation on alumina materials suggest a distinct site distribution on α-, γ-, and η-Al_2O_3 analogous to ethene formation. We note here that the selectivity to ethene ($\frac{r_{ethene}}{r_{ethene}+2r_{DEE}}$) varies with the polymorph of alumina. γ-Al_2O_3 shows the highest selectivity to ethene although the ethanol conversion rate is similar to η-Al_2O_3 (Figure 3.4). The different selectivity results from discrete kinetic parameters, a consequence of the distinct site distributions on the different alumina polymorphs.

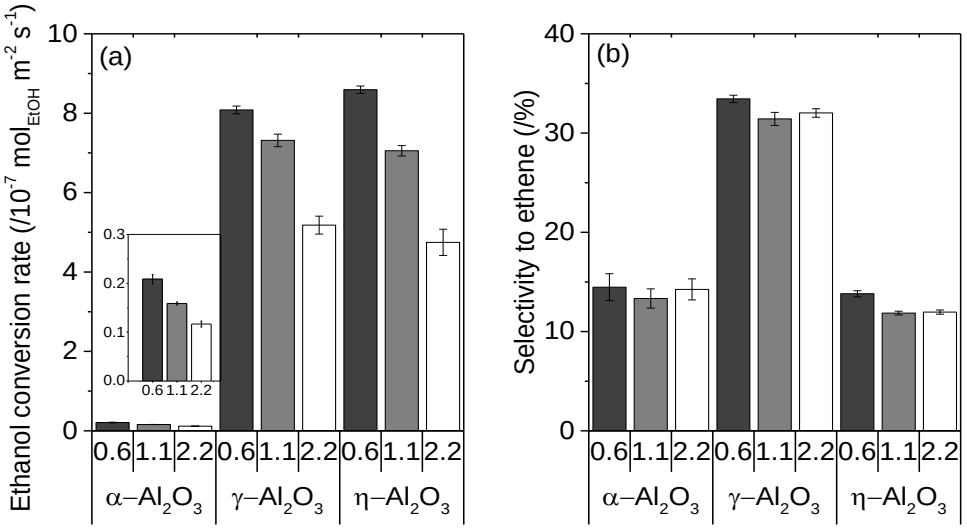

Figure 3.4 (a) Ethanol conversion rate per surface area ($r_{ethene} + 2r_{DEE}$) and (b) selectivity to ethene calculated as $(r_{ethene})/(r_{ethene} + 2r_{DEE})$ for ethanol dehydration at 573 K on α-, γ-, and η-Al_2O_3 with 2.2 kPa of ethanol and 0.6 kPa (black), 1.1 kPa (gray), and 2.2 kPa (white) of water partial pressure.

3.3.2.2.2. Site densities of di-ethanol dehydration on different alumina materials at 573 K

The site densities of DEE formation on γ- and η-Al_2O_3 at 573 K were established using in-situ pyridine titration and are shown in Table 3.4 (see Table 3.8 and 3.9 for data from independent titrations at different pyridine partial pressures). The rate constants normalized per site as determined by pyridine titration at 573 K for DEE formation are tabulated in Table 3.5. Site densities and rate constants for DEE formation are similar in magnitude for these transitional aluminas; analogous observations were made for ethene

synthesis site densities, suggesting that the surface structure of γ- and η-Al_2O_3 is similar under reaction conditions for alcohol dehydration probed in this research.

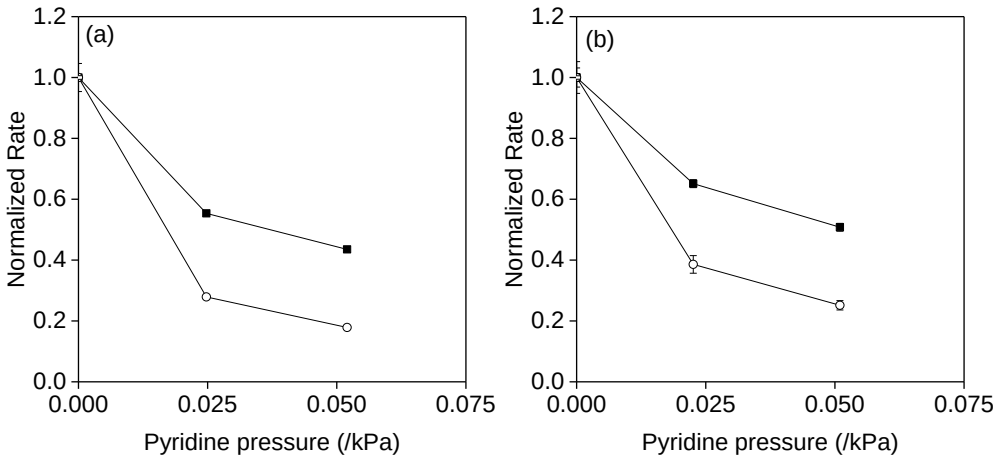

Figure 3.5 Normalized rates (rate with pyridine/rate without pyridine) of (○) ethene and (■) DEE for ethanol dehydration at 573 K on (a) 2.7 mg of γ-Al_2O_3 (10% of ethanol conversion) and (b) 2.3 mg of η-Al_2O_3 (16% of ethanol conversion) as a function of pyridine partial pressure with 2.2 kPa of ethanol and 1.0 kPa of water partial pressure. The solid lines are meant to guide the eye.

3.3.3. Site heterogeneity on alumina materials

An extensive body of structural and chemical characterization studies discussed in Section 3.1 describes the putative site heterogeneity that exists on the surface of alumina materials – specifically, the preferential hydration/dehydroxylation of specific facets on γ-Al_2O_3[19] and the existence of tri-, tetra-, and penta-coordinated sites on different alumina materials[19,37,74]. This research addresses two critical questions regarding site heterogeneity in alumina materials under reaction conditions using alcohol dehydration as a probe reaction. First, we observe the existence of at least two distinct sites for alcohol dehydration

on alumina materials as inferred from (i) the different inhibition of ethene and DEE synthesis rates by pyridine on both γ- and η-Al_2O_3 (Figure 3.5) and (ii) the ratio of the rate of olefin synthesis to the rate of ether synthesis being independent of alcohol pressure as noted for 2-propanol in our previous report[11]. Related to (i) above, a recent report from Larmier et al.[98] develops a detailed microkinetic model for mono- and di-2-propanol dehydration on γ-Al_2O_3 which incorporates pathways corresponding to ether decomposition and is utilized to predict the concentration profiles and selectivity of propene and diisopropyl ether over the entire range of 2-propanol conversion at 473 K. This work also considers the active catalytic center on the (100) facets of γ-Al_2O_3 to comprise of a macroscopic assembly of three active sites based on computational models developed by Digne et al.[18,19] A common active site is depicted as catalyzing both mono- and di-alcohol reaction pathways. The results we report in Figure 3.5 show that on both γ- and η-Al_2O_3, the rate of diethyl ether synthesis is inhibited to a lower extent by pyridine than ethene synthesis rates. The data reported in Figure 3.5 were obtained at <16% conversion for both γ- and η-Al_2O_3 and represent the net synthesis rate measured experimentally - this measurement incorporates any potential ether decomposition pathways that may occur at these reaction conditions (see Section 3.5.3.1 for additional discussion). The preferential inhibition of mono-alcohol pathways relative to di-alcohol ether formation leads us postulate the existence of more than one active site. Related to (ii) above, if a common set of active sites was involved in mono- and di-alcohol dehydration, the ratio of ether to olefin synthesis rates would be linear function of alcohol pressure

($\frac{r_{ether}}{r_{olefin}} = \frac{k_{ether}P_{alcohol}^2}{Common\ terms} / \frac{k_{olefin}P_{alcohol}}{Common\ terms} = \frac{k_{ether}}{k_{olefin}}P_{alcohol}$), however, this ratio is noted to be independent of alcohol pressure at alcohol pressures exceeding 4 kPa as reported in Figure 3.9.

Second, we report that under catalytic reaction environments for ethanol dehydration both at 573 and 623 K, the same mechanistic and kinetic description applies to all alumina materials and the site densities and catalytic rates for these sites on transitional alumina materials are very similar.

3.4. Conclusion

The kinetic and mechanistic description for parallel ethanol dehydration pathways are similar on α-, γ-, and η-Al_2O_3 materials suggesting that similar sites exist on all alumina materials under reaction conditions (573 and 623 K). An assessment of the site density on γ- and η-alumina using in-situ chemical titration with pyridine suggests that these high-surface area materials possess similar site densities and surface characteristics. Mono-alcohol dehydration rates are inhibited to a greater extent than di-alcohol dehydration rates in pyridine inhibition studies suggesting that a manifestation of the diversity of surface characteristics on alumina materials is the existence of multiple pools of catalytic sites on these materials under reaction environments.

3.5. Supporting information

3.5.1. Structural characterization of alumina materials

Scanning electron microscopy (SEM) experiments were performed using a Hitachi SU8230 field emission gun scanning electron microscope at an electron acceleration

voltage of 1.0 kV. The SEM images of α-, γ-, and η-Al_2O_3 are shown in Figure 3.6. Because α-Al_2O_3 is synthesized by heating γ-Al_2O_3 powder, particles of α-Al_2O_3 look like agglomerates of particles of γ-Al_2O_3. The crystal size of γ-Al_2O_3 is too small to distinguish in Figure 3.6 (b). The particle shape of η-Al_2O_3 is plate-like.

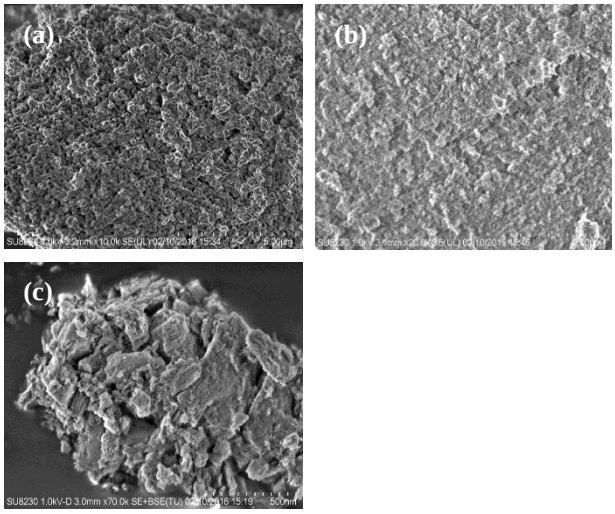

Figure 3.6 SEM images of (a) α-, (b) γ-, and (c) η-Al_2O_3

3.5.2. Site densities of ethanol dehydration on different alumina materials at 573 K from in-situ pyridine titration

In-situ pyridine titration was employed to study the site densities of ethanol dehydration on different alumina polymorphs at 573 K. Figure 3.7 is an example of in-situ pyridine titration. After the synthesis rates of ethene and diethyl ether (DEE) reach the steady state, pyridine was introduced to reactant flow. We extrapolated the initial linear decrease of ethene and DEE formation rates to determine the required amount of pyridine to completely deactivate ethene and DEE synthesis. All data sets from independent

titrations at different pyridine pressures on different alumina materials are shown in Tables 3.8 and 3.9.

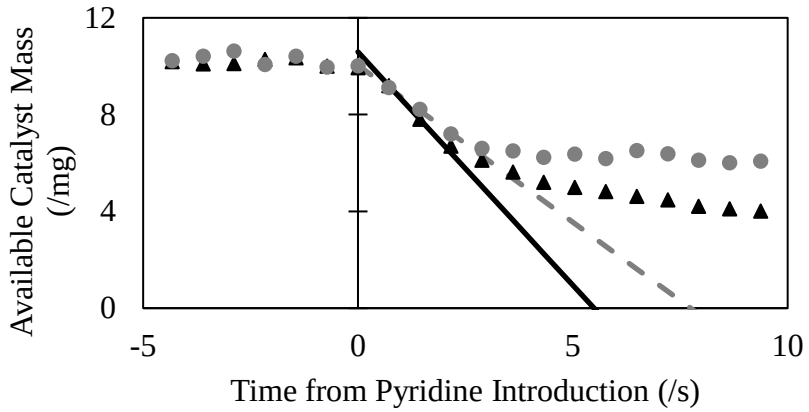

Figure 3.7 Available catalyst mass for (▲) ethene and (●) DEE formation on 10.2 mg of γ-Al_2O_3 at 573 K with 2.2 kPa of ethanol and 1.0 kPa of water partial pressure (total gas flowrate = 3.4 cm^3 s^{-1}) as a function of time from the introduction of 0.02 kPa of pyridine to reactant flow. The black solid and gray dashed lines representing ethene and DEE, respectively, show the linear extrapolation to calculate the pyridine uptake to completely inhibit ethanol dehydration.

Table 3.8 Numbers of catalytic sites for ethene and DEE formation from parallel ethanol dehydration on ~10 mg of γ-Al_2O_3 at 573 K with 2.2 kPa of ethanol and 1.0 kPa of water partial pressure assessed using in-situ pyridine titration.

Alumina materials	Pyridine partial pressure (/kPa)	Ethene		DEE	
		Pyridine uptake ($/10^{-5}$ mol g^{-1})	Sites per surface area ($/nm^{-2}$)	Pyridine uptake ($/10^{-5}$ mol g^{-1})	Sites per surface area ($/nm^{-2}$)
γ-Al_2O_3	0.02	2.3	0.099	1.9	0.082
		2.1	0.091	3.6	0.15
		1.8	0.077	2.6	0.11
		2.3	0.097	1.9	0.079
	0.05	N/A	N/A	3.1	0.13
		3.0	0.13	2.7	0.12
		3.2	0.14	3.1	0.13
		3.3	0.14	3.2	0.14
		2.8	0.12	5.9	0.25
		3.0	0.13	3.8	0.16
		3.2	0.14	3.4	0.14
		3.1	0.13	3.5	0.15

Table 3.9 Numbers of catalytic sites for ethene and DEE formation from parallel ethanol dehydration on ~10 mg of η-Al_2O_3 at 573 K with 2.2 kPa of ethanol and 1.0 kPa of water partial pressure assessed using in-situ pyridine titration.

Alumina materials	Pyridine partial pressure (/kPa)	Ethene		DEE	
		Pyridine uptake ($/10^{-5}$ mol g^{-1})	Sites per surface area ($/nm^{-2}$)	Pyridine uptake ($/10^{-5}$ mol g^{-1})	Sites per surface area ($/nm^{-2}$)
η-Al_2O_3	0.02	2.4	0.040	6.8	0.11
		3.4	0.056	5.8	0.097
		3.1	0.051	5.1	0.085
		2.3	0.038	4.3	0.072
	0.05	4.2	0.071	6.3	0.10
		6.1	0.10	4.1	0.068
		4.2	0.071	4.5	0.075
		4.6	0.077	2.8	0.047
		3.7	0.063	8.5	0.14
		4.4	0.074	7.2	0.12
		4.6	0.078	5.2	0.087
		4.5	0.076	4.1	0.068

3.5.3. Site heterogeneity on alumina materials

3.5.3.1. Inhibition of ethene and DEE synthesis rates in ethanol-pyridine co-feed studies

The reported ethene and DEE formation rates in this work are net synthesis rates of ethene and DEE. The net synthesis rates ($r_{ethene,net}$ and $r_{DEE,net}$) which we measure experimentally include the formation rates of ethene and DEE from ethanol dehydration ($r_{ethene,deh}$ and $r_{DEE,deh}$) and the DEE decomposition rate ($r_{DEE,dec}$) as shown in Equation 3.6 and 3.7.

$$r_{ethene,net} = r_{ethene,deh} + r_{DEE,dec} \quad (3.6)$$

$$r_{DEE,net} = r_{DEE,deh} - r_{DEE,dec} \quad (3.7)$$

We wish to compare $r_{ethene,deh}$ and $r_{DEE,deh}$ to examine the possibility that distinct active sites catalyze parallel ethanol dehydration reactions on alumina materials. The reaction conditions that we used in the report (573 K and 10% of ethanol conversion on γ-Al_2O_3 and 16% of ethanol conversion on η-Al_2O_3) result in low DEE pressure (0.09 and 0.17 kPa on γ-Al_2O_3 and η-Al_2O_3, respectively) at the reactor outlet, implying that the DEE decomposition rate would be negligible compared to $r_{ethene,deh}$ and $r_{DEE,deh}$, resulting $r_{ethene,net} \cong r_{ethene,deh}$ and $r_{DEE,net} \cong r_{DEE,deh}$ (see also Figure 3.8 and the discussion in the following paragraph). Therefore, the normalized rates reported in Figure 3.5 represent the change in $r_{ethene,deh}$ and $r_{DEE,deh}$ with and without pyridine. $r_{ethene,deh}$ and $r_{DEE,deh}$ are differently inhibited by pyridine, implying at least two pools of active sites exist on alumina materials as discussed in Section 3.3.3.

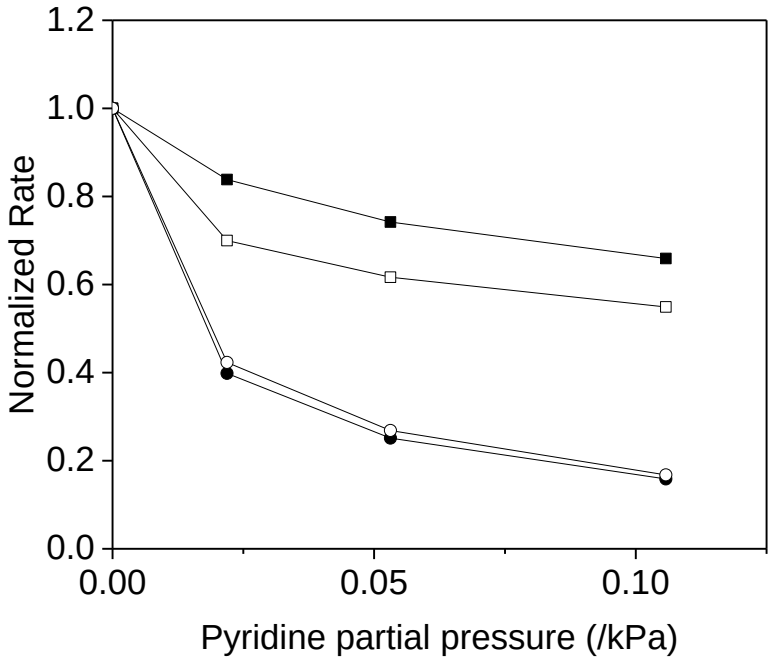

Figure 3.8 Normalized net synthesis rates (net synthesis rate with pyridine/net synthesis rate without pyridine) of (●) ethene and (■) DEE and normalized ethanol dehydration rates (net synthesis rate with pyridine/formation rate from ethanol dehydration without pyridine) of (○) ethene and (□) DEE for ethanol dehydration at 623 K on 1.1 mg of γ-Al_2O_3 (28% of ethanol conversion) as a function of pyridine partial pressure with 2.2 kPa of ethanol and 1.0 kPa of water partial pressure. Solid lines are meant to guide the eye.

Figure 3.8 shows observed normalized net synthesis rates ($\frac{r_{ethene,net,w/\ pyridine}}{r_{ethene,net,w/o\ pyridine}}$ and $\frac{r_{DEE,net,w/\ pyridine}}{r_{DEE,net,w/o\ pyridine}}$) and calculated normalized formation rates from ethanol dehydration ($\frac{r_{ethene,net,w/\ pyridine}}{r_{ethene,deh,w/o\ pyridine}}$ and $\frac{r_{DEE,net,w/\ pyridine}}{r_{DEE,deh,w/o\ pyridine}}$) of ethene and DEE at 623 K using the rate expression and kinetic and thermodynamic parameters that we have reported previously

for DEE decomposition at 623 K[92]. We calculate $r_{DEE,dec,w/o\ pyridine}$ using ethanol and DEE pressure (the highest value of DEE pressure at the outlet was used to test the limiting case scenario) and obtain $r_{ethene,deh,w/o\ pyridine}$ and $r_{DEE,deh,w/o\ pyridine}$ using Equation 3.6 and 3.7. $r_{ethene,net,w/\ pyridine}$ and $r_{DEE,net,w/\ pyridine}$ are used in the numerator for normalized formation rates from ethanol dehydration to consider the bookend scenario. The normalized formation rate of ethene from ethanol dehydration is slightly higher than the normalized synthesis rate of ethene. Conversely, the normalized formation rate of DEE from ethanol dehydration obtained after adding the rate of DEE decomposition is apparently lower than the normalized synthesis rate of DEE. The distinction between the inhibition of ethene and DEE synthesis rates by pyridine persists even after considering the bookend scenario for DEE decomposition pathways as shown in Figure 3.8 suggesting the existence of multiple active sites on alumina materials.

3.5.3.2. 2-propanol partial pressure dependence of ratio of ether to olefin synthesis rates at 488 K

The ratio of ether formation to olefin formation rates for parallel 2-propanol dehydration reactions on γ-Al_2O_3 at 488 K as a function of 2-propanol partial pressure is shown in Figure 3.9. The ether and olefin formation rates for 2-propanol dehydration are from our previous reports[11]. The ratio is noted to be not linear and independent of 2-propanol partial pressure at 2-propanol partial pressures exceeding 4 kPa, which will not be the case if the sites for mono- and di-alcohol dehydration are same as discussed in Section 3.3.3.

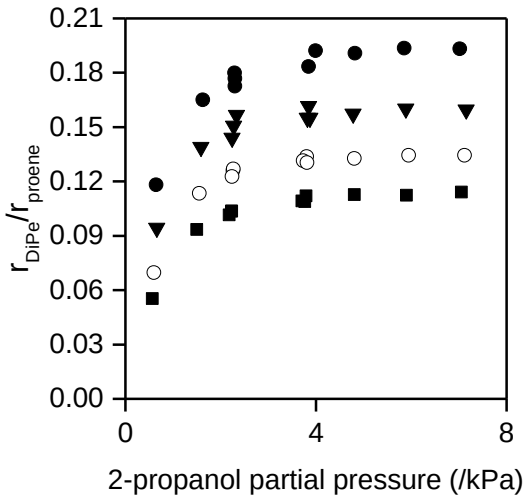

Figure 3.9 The ratio of DiPE formation rate to propene formation rate as a function of 2-propanol partial pressure with different water partial pressures (■ 0.33, ○ 0.65, ▼ 1.1, and ● 2.1 kPa) using 10 mg of γ-Al_2O_3 at 488 K (total gas flow rate = 3.4 cm^3 s^{-1}, 2-propanol conversion <10%).

3.6. Acknowledgements

We appreciate financial support from The Dow Chemical Company. We also acknowledge Dr. Donghun Kim for taking SEM images and Dr. Hsu Chiang and Joseph F. DeWilde for helpful technical discussions.

4. Kinetics, mechanisms, and site characterization of ethanol dehydration on zirconia catalyst

4.1. Introduction

Zirconia-based formulations are widely used as catalysts or catalyst supports[102,103]. The structural and chemical characteristics which determine the catalytic properties of zirconia-based materials such as structural morphology – cubic, monoclinic, or tetragonal, acid-base bifunctional properties, and redox properties depend on the preparation method; the identity of precursors ($ZrOCl_2$, $ZrCl_4$, $ZrO(NO_3)_2$, $Zr(NO_3)_4$, and others), the pH of the precursor solution, and the thermal treatment and gas environment during the conversion of a hydroxylated zirconia precursor to synthesize the oxidic formulation[27,104–107]. The diversity of surface sites on ZrO_2 could be inferred from the wide-ranging degree of Zr-coordination and hydroxylation. Infrared (IR) spectra of ZrO_2 at room temperature shows that there are terminal hydroxyl groups (3776 cm^{-1}) and multi-centered hydroxyl groups (3679 and 3668 cm^{-1}) which results in acidic and basic catalytic functions[108]. IR spectra of pyridine adsorbed on ZrO_2 at 373 K show pyridine coordinately bonded to Lewis acid sites (1600, 1485, and 1440 cm^{-1}) and, when pyridine is adsorbed at 473 and 573 K, an absorption band at 1550 cm^{-1} is observed which is assigned to a pyridinium ion bound at a Brønsted acid site [106,108–110]. IR spectra of ammonia adsorbed on ZrO_2 at 300-673 K also show the existence of Lewis and Brønsted acid sites and of Zr-NH_2 sites (3528 and 3503 cm^{-1}) along with the formation of Zr-OH groups (3733 cm^{-1}), that ammonia can covalently

bond with[109]. Hydrogen adsorption on ZrO_2 at 373-523 K gives Zr-H and Zr-OH, inferred from IR bands at 1371 and 3780 cm^{-1}, respectively[111]. IR spectra of carbon monoxide adsorbed on ZrO_2 at 670-1070 shows two bands corresponding to CO adsorption (2196 and 2184 cm^{-1}) altering according to the temperature[112]. Carbon dioxide adsorption on ZrO_2 at 298-673 K gives IR bands corresponding to HCO_3^- and bidentate carbonate (1628 and 1573 cm^{-1}), indicating the existence of basic sites[109–111,113,114]. These IR studies elucidate not only the diversity of sites but also the evolution of sites according to the temperature. Calorimetric studies using ammonia, pyridine, and carbon dioxide as titrant report the number of acidic and basic sites and the evolution of those sites with temperature based on the observed changes in the heat of adsorption of different titrants[26,106,114,115]. Piskorz and co-workers[116,117] calculated surface energies of various surface planes of monoclinic and tetragonal zirconia at 273-1173 K using DFT with PW 91 functional and concluded that the surface hydroxyl group densities decrease from fully hydroxylated to an empty surface as temperature increases to give the lowest surface energy. The surface properties of ZrO_2 depend on the environmental conditions.

Alcohol dehydration is one of the reactions catalyzed by zirconia. The product selectivity and rate of alcohol dehydration depend on the surface properties of ZrO_2, so this is a good probe reaction to study the ZrO_2 surface. The characterization of surface sites under reaction environments is also important as discussed above. The acidity of the metal and the basicity of its neighboring surface oxygen atoms decides the activity of dehydration on metal oxides[118,119]. The NH_3 uptake at 303 K is 1.7 μmol m^{-2} on 1wt% Na loaded ZrO_2 while it is 3.3 μmol m^{-2} on ZrO_2, however, the rate of mono-ethanol dehydration on 1wt%

Na loaded ZrO_2 is less than 5% of that on ZrO_2 at temperatures in the range 613-673 K[26]. From these data, the authors concluded that acid sites are required for ethene formation on ZrO_2. α-olefin selectivity for dehydration of 2-alcohols increases along with an increase in the ratio of base to acid sites calculated from the uptake of carbon dioxide as an acidic titrant and ammonia as a basic titrant[27,104,105,115,120,121]. Basic sites catalyze the E1cB mechanism - elimination reaction involving a carbanion as an intermediate - for mono-alcohol dehydration which favors α-olefins. E2 mechanism for olefin formation catalyzed by acid-base bifunctional sites also favors α-olefins. The amphoteric characteristics of ZrO_2 control the selectivity distribution and the relative strength of acid and base sites is one of the key factors in controlling selectivity. Kostestkyy et al.[17] calculated the activation energy of olefin formation through E2 elimination mechanism from C_2-C_4 alcohols on $Zr_2O_2(OH)_4$ using DFT with B3LYP functional and the reaction pathway on surface O atoms of model zirconia (173 kJ mol^{-1}) gave a lower activation energy than that computed for dehydration on surface OH groups (178 kJ mol^{-1}). This indicates that surface hydroxyl groups may also mediate reactions on zirconia surfaces.

In this study, we characterize the surface of hydrated ZrO_2 using ethanol dehydration as a probe reaction. We propose the mechanistic pathways for parallel dehydration reactions in the temperature range 548-623 K. We elucidate the change of the surface sites along with the reaction temperature. We also report the diversity of sites on zirconia. We suggest that weak acid-bases sites on ZrO_2 are the active sites for ethanol dehydration. The chemical titration studies that we report allow us to probe the identity of surface sites under reaction environments.

4.2. Materials and Methods

4.2.1. Catalyst preparation and characterization

The zirconia material used in this study was synthesized following a procedure reported by Rezaei et al[122]. Briefly, Pluronic P123 polyethylene glycol-polypropylene glycol (PEG-PPG) block copolymer (14.12g; M_n ~5800; Sigma-Aldrich) was dissolved in 95 mL deionized water at a 0.03 molar ratio of polymer to metal and $ZrO(NO_3)_2 \bullet xH_2O$ (24.20g; Alfa-Aesar 99.9% metals basis) precursor was subsequently added to the solution. The pH of this mixture was adjusted to ~11 by NH_4OH addition and the solution was heated to 353 K under rapid stirring. Thermal treatment of these mixtures in air (0.33 K s^{-1} and 0.83 cm^3 s^{-1}) to 923 K led to dry powder-form materials. X-ray diffraction patterns of the as-synthesized materials were recorded on a Bruker-AXS Microdiffractometer with Cu K(α) radiation (1.54 Å) in step mode with a step size of 0.04° per s (2θ in the range 10–70°) to verify zirconia synthesis. Brunauer–Emmet–Teller (BET) surface area of the synthesized ZrO_2 powder was measured using N_2 adsorption/desorption at 77 K with a Micromeritics ASAP 2020.

The powder of synthesized zirconia material was compressed and sieved to gain catalyst particles between 180 and 250 μm (60-80 mesh). The catalyst bed composed of ~10 mg of zirconia materials and ~0.7 g of acid-washed quartz sand as diluent in a packed bed quartz tube reactor was treated with a stream of air (1.7 cm^3 s^{-1} at NTP conditions, Minneapolis Oxygen) at 823 K for 4 h and cooled down to reaction temperature.

Subsequently, the catalyst bed was treated with 2.2 kPa of water which fed into a stream of helium (1.7 cm^3 s^{-1} at NTP conditions, Minneapolis Oxygen).

4.2.2. Steady-state kinetic measurements of ethanol dehydration

The formation rates of ethene and DEE were measured at different ethanol and water partial pressures under differential conversion (<1%) to study the kinetics of mono- and di-ethanol dehydration on ZrO_2 using prepared catalyst beds. A tube furnace (National Electric Furnace FA120 type) and a Watlow temperature controller (96 series) were used to maintain reaction temperatures of 548-623 K while measuring reactor temperature with a type K thermocouple located on the external surface of the reactor. Liquid ethanol (Decon Labs, Inc., 0.84-23 kPa) and deionized water (0.42-2.3 kPa) were co-fed and vaporized into a stream of helium (3.4 cm^3 s^{-1} at NTP conditions) and an internal standard mixture for gas chromatographic (GC) analysis comprising Ar/CH_4 (10.0% CH_4 and Ar balance, 0.15 cm^3 s^{-1} at NTP conditions, Matheson Trigas). Liquids were fed using two separate infusion syringe pumps (KDS100). Resistively heated gas lines keeping temperatures above 343 K were employed to avoid condensation of liquids.

An online GC (Agilent 6890 N, flame ionization detector with Agilent Plot-Q column) and an online mass spectrometer (MKS Cirrus 200 quadrupole, MS) were used to analyze the reactor effluent. Reported error bars in figures below represents 95% confidence intervals using successive GC injections under the same experimental conditions.

4.2.3. Estimation of kinetic parameters

Bayesian statistical estimation techniques in the Athena Visual Studio (v14.2, W.E. Steward and M. Caracotsios) were used to optimize kinetic parameters. The represented uncertainties were the 95% marginal highest posterior density intervals. The experimental conditions under the same ethanol and water pressure were defined as replicates.

4.2.4. In-situ titration of catalytic sites responsible for ethanol dehydration

Ethanol (2.2 kPa) and water (1.0 kPa) with flowing He (3.4 cm^3 s^{-1} at NTP conditions) were co-fed into the catalyst bed (308.8 mg) at 573 K. Liquid pyridine (>99%, Sigma-Aldrich, 0.1-0.2 kPa) or CO_2 (2.5-5.0 kPa) was introduced to reactant flow after seeing steady-state rates of dehydration to measure inhibition by base or acid titrant.

4.3. Results and Discussion

4.3.1. Structural characterization of the zirconia material

The crystalline structure of synthesized zirconia material was analyzed using powder X-ray diffraction. The XRD pattern (Figure 4.1) shows that the synthesized zirconia material is a mixture of monoclinic and tetragonal phases. The broaden peaks suggest that nanocrystalline domains exist in the synthesized material. The porous characteristics of the zirconia material were studied using N_2 adsorption and the measured BET surface area was 81 m^2/g.

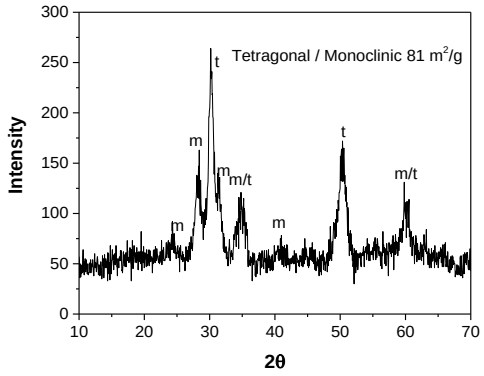

Figure 4.1 XRD pattern of polymer-templated ZrO_2 and identification of each peak to monoclinic (m) or tetragonal (t) phase.

4.3.2. Kinetics and mechanism of ethanol dehydration on zirconia material

The synthesis rates of ethene increase as ethanol pressure increases when co-feeding ethanol and water at 548-623 K on the ZrO_2 catalyst, which is shown in Figure 4.2 (ethanol partial pressure in the range 0.84-23 kPa and water partial pressure in the range 0.42-2.3 kPa). There are three kinetically indistinguishable mechanisms to form ethene, an E2-type mechanism with physisorbed molecular ethanol species, an E1-type mechanism with chemisorbed alkoxide derived from ethanol, and an E1cB mechanism. Alcohol monomer is involved in the rate determining step of these mechanisms. The mechanism prevalent is postulated to depend on the preparation method of ZrO_2. ZrO_2 catalysts prepared under basic conditions have basic sites strong enough to deprotonate C_β, and propagate the E1cB mechanism, which involves a carbanion-like intermediate and preferentially forms α-olefins (>80% selectivity) from the dehydration of 2-ols[27,102,105,123]. ZrO_2 catalysts prepared under neutral or acidic conditions have amphoteric characteristics and catalyze alcohol

dehydration reaction via an E2-type mechanism preferentially forming α-olefins with a mixture of other olefins from the dehydration of 2-ols because strong basic sites related to the E1cB mechanism are protonated[120,124]. Acidity strong enough to catalyze the dehydration of alcohols via E1 elimination can be achieved by doping sulfate group on ZrO_2[105,121]. Kostestkyy et al.[17] showed that the E2-type mechanism has a lower activation energy barrier than the E1-type mechanism for alcohol dehydration on ZrO_2 based on DFT calculations, and proposed that the cleavage of the C_β-H bond of ethanol monomer species is the rate limiting step for mono-alcohol dehydration on ZrO_2. They calculated the activation energy on $Zr_2O_2(OH)_4$ clusters, hydroxylated ZrO_2, which may be similar to the ZrO_2 catalyst we used because we treated the catalyst with water before reaction. We consider an E2-type mechanism for ethene formation on ZrO_2 based on these reports, however, we note that the reaction rate expression is independent of the detailed mechanistic pathways. Ethene formation rates decrease when water partial pressure increases, suggesting that ethene formation is inhibited by co-adsorption of water. Ethene synthesis rates asymptotically line out with increasing ethanol pressure suggesting that there are ethanol-water dimer species on the surface under reaction conditions. The observed pressure dependencies of the rate of mono-alcohol dehydration on ethanol and water partial pressure indicate ethanol monomers, water monomers, and ethanol-water dimers are dominating surface species. The dependencies were unchanged in the temperature range 548-623 K, which indicates that dominating surface species do not change in the temperature range studied. The rate expression shown in Equation 4.1 explains the measured formation rates of ethene.

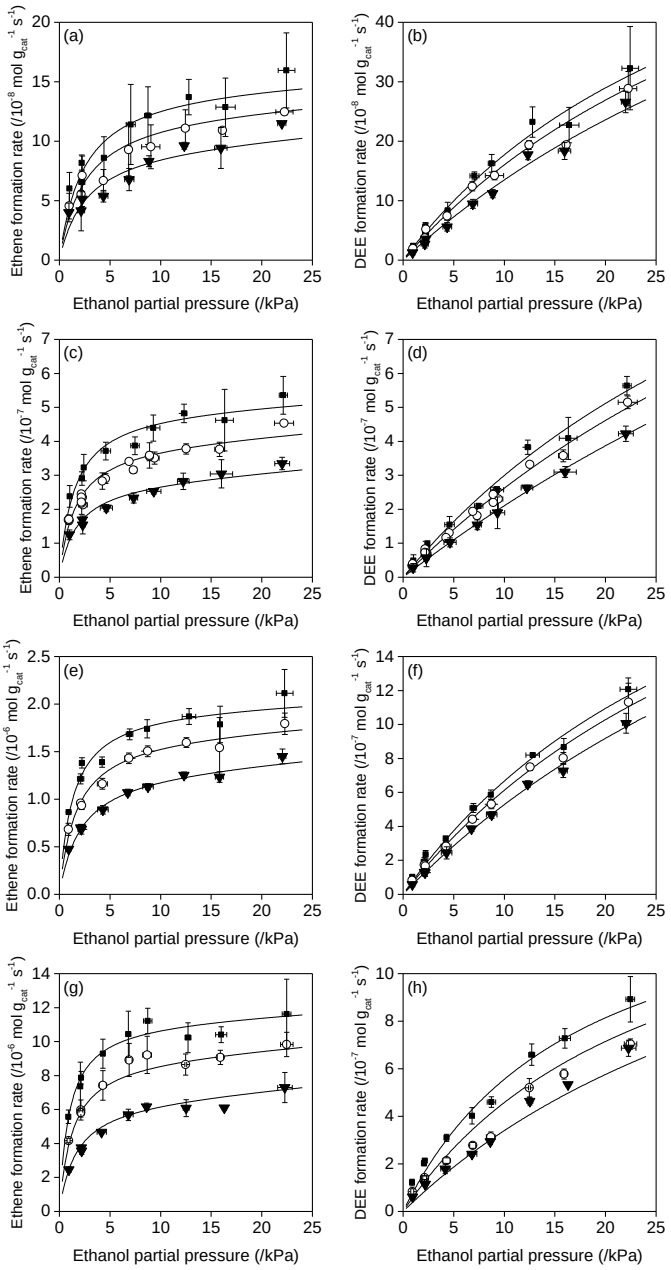

Figure 4.2 (a, c, e, g) Ethene and (b, d, f, h) DEE formation rates for ethanol dehydration at (a), (b) 548 K, (c), (d) 573 K, (e), (f) 598 K, and (g), (h) 623 K on ZrO_2 as a function of ethanol partial pressure with (■) 0.05 ml/hr, (○) 0.1 ml/hr, and (▼) 0.2 ml/hr of water co-feed. The solid line represents the model fits to Equations 4.1 and 4.2 for (a, c, e, g) and (b, d, f, h), respectively.

$$r_{ethene} = \frac{k_{ethene} K_A P_{alcohol}}{1 + K_A P_{alcohol} + K_{W1} P_{water} + K_{AW} P_{alcohol} P_{water}} \quad (4.1)$$

k_{ethene} in Equation 4.1 is the rate constant of the rate determining step and K_A, K_{W1}, and K_{AW} are equilibrium constants for adsorption of alcohol monomers, water monomers, and alcohol-water dimers, respectively, on the surface of zirconia catalysts. Kinetic and equilibrium constants in Equation 4.1 are estimated using Bayesian statistical estimation techniques in the Athena Visual Studio (v14.2, W. E. Stewart and M. Caracotsios) and tabulated in Table 4.1.

Table 4.1 Estimated kinetic parameters for mono-alcohol dehydration of ethanol on ZrO_2 at 548, 573, 598, and 623 K using the model presented in Equation 4.1 and data from Figure 4.2

Temperature	k_{ethene} (/mol g_{cat}^{-1} s^{-1})	K_A (/kPa^{-1})	K_{W1} (/kPa^{-1})	K_{AW} (/kPa^{-2})
548 K	(1.82 ± 0.23) x 10^{-7}	0.456 ± 0.232	0.545 ± 0.632	0.170 ± 0.059
573 K	(6.69 ± 0.44) x 10^{-7}	0.808 ± 0.312	1.01 ± 0.685	0.486 ± 0.136
598 K	(2.38 ± 0.12) x 10^{-6}	1.21 ± 0.50	1.63 ± 1.02	0.429 ± 0.129
623 K	(1.47 ± 0.09) x 10^{-5}	2.36 ± 1.82	3.49 ± 3.44	1.36 ± 0.84

We studied the kinetics and mechanism of diethyl ether (DEE) formation in di-alcohol dehydration on ZrO_2.The formation rates of DEE versus ethanol and water partial pressures are shown in Figure 4.2. We consider an S_N2-type mechanism for DEE formation with the involvement of an alcohol dimer in the rate limiting step. The positive dependence of DEE synthesis rates on ethanol pressure indicates the existence of ethanol monomer

species. The inhibition by water may be caused by ethanol-water dimers. The dominating surface species inferred from the observed pressure dependencies of di-alcohol dehydration on ethanol and water partial pressure are alcohol monomer, alcohol dimer, and alcohol-water dimer surface species. The dependencies were unchanged in the temperature range 548-623 K, similar to the observation noted for ethene formation. The rate expression for DEE formation is described in Equation 4.2.

$$r_{DEE} = \frac{k_{DEE} P_{alcohol}^2}{P_{alcohol}^2 + \frac{K_{A1}}{K_{A2}} P_{alcohol} + \frac{K_{AW}}{K_{A2}} P_{alcohol} P_{water}} \quad (4.2)$$

k_{DEE} in Equation 4.2 is the rate constant of the rate determining step and K_{A1}, K_{A2}, and K_{AW} are equilibrium constants for adsorption of alcohol monomers, alcohol dimers, and alcohol-water dimers, respectively, on the surface of zirconia catalysts. Kinetic and equilibrium constants in Equation 4.2 were estimated using Bayesian statistical estimation techniques in the Athena Visual Studio (v14.2, W. E. Stewart and M. Caracotsios) and tabulated in Table 4.2.

Table 4.2 Estimated kinetic parameters for di-alcohol dehydration of ethanol on ZrO_2 at 548, 573, 598, and 623 K using the model presented in Equation 4.2 and data from Figure 4.2

Temperature	k_{DEE} (/mol g_{cat} s^{-1})	K_{A1}/K_{A2} (/kPa)	K_{AW}/K_{A2}
548 K	(7.57 ± 1.06) x 10^{-7}	28.2 ± 6.4	9.28 ± 2.05
573 K	(1.60 ± 0.20) x 10^{-6}	35.7 ± 6.8	15.7 ± 2.5
598 K	(2.92 ± 0.28) x 10^{-6}	29.9 ± 4.6	7.99± 1.30
623 K	(1.43 ± 0.15) x 10^{-6}	10.2 ± 2.0	11.4 ± 2.9

As shown in Table 4.1 and 4.2, the DEE formation rate constants increase as temperature increases from 548 to 598 K but decrease at 623 K, which may imply that the surface properties of zirconia evolve under reaction conditions at 623 K. This decrease is irrelevant to the decrease in the number of adsorbed surface species because the number of surface species is related to adsorption equilibrium constants in the rate expressions we proposed. The estimated equilibrium constants do not show the characteristics of ideal adsorption of dominating surface species, the decrease of the constants as temperature increases. These indicates different surface characteristics at each temperature, causing different heat of adsorption or available number of adsorption sites. Although the dominating surface species do not change in temperature range 548-623 K, kinetic and equilibrium parameters for adsorbed species should be estimated at each temperature. Arrhenius equation and Van't Hoff equation should be used only if surface properties are unchanged in the relevant temperature range. Digne et al.[19] modeled the (100) and (110) surfaces of γ-Al_2O_3 with tri-, tetra-, and penta-coordinated aluminum surface atoms using DFT with PW 91 functional and reported that the surface hydroxyl coverage at the lowest surface energy decreases from 13 to 0 OH nm^{-2} for the (100) facet while temperature increases from 450 to 600 K and from 18 to 3 OH nm^{-2} for the (110) facet while temperature increases from 400 to 1000 K. They also noted that the hydroxylation of surface atoms changes the coordination of surface aluminum atoms. Similar studies about ZrO_2 discussed in Section 4.1[116,117] also show a decrease in the surface hydroxyl group density as temperature increases from 273-1173 K to give the lowest surface energy of ZrO_2. These computational calculations implicate a dependency of surface properties of metal oxide

materials on the environmental conditions particularly temperature and the presence of water. The evolution of surface characteristics of ZrO_2 materials is reflected in the anomalous increase in the rate constant for diethyl ether formation with temperature as shown in Table 4.2 and by the irrelevant changes in adsorption equilibrium constants with temperature as shown in Tables 4.1 and 4.2.

The rate expression and mechanism that we propose for ethanol dehydration on ZrO_2 are same as what we proposed for ethanol dehydration on alumina materials[11,12,43,58]. The mechanistic assessment of observed pressure dependencies of reaction rates elucidates the existence and kinetic involvement of multimeric surface species on ZrO_2 suggesting that this observation may be a common characteristic of metal oxides as it is reported for other metal oxides (Al_2O_3, WO_3, and MoO_3)[85,98–100].

4.3.3. Site heterogeneity on zirconia material

The kinetic studies on ZrO_2 show the site heterogeneity on ZrO_2. The relative ratio of DEE and ethene formation rate of ethanol dehydration should show linear relationship if two parallel reactions occur on the same sites ($\frac{r_{ether}}{r_{olefin}} = \frac{k_{ether}P_{alcohol}^2}{Common\ terms} \Big/ \frac{k_{olefin}P_{alcohol}}{Common\ terms} = \frac{k_{ether}}{k_{olefin}}P_{alcohol}$). The ratio on ZrO_2 does not show a linear relationship with ethanol partial pressure as shown in Figure 4.3, although it is not as clear as 2-propanol dehydration on γ-Al_2O_3 at 488 K, shown in Figure 3.9. Chemical titration also shows the site heterogeneity. Pyridine inhibits di-alcohol dehydration more than mono-alcohol dehydration at 573 K on ZrO_2 as shown in Figure 4.4. The different inhibition of mono- and di-alcohol dehydration by pyridine indicates that sites for two parallel dehydration reactions are distinct. We

propose that there are at least two kinds of sites on zirconia under reaction conditions, which supports the diversity of sites on zirconia materials.

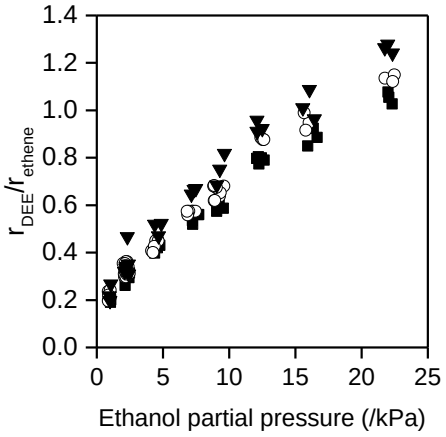

Figure 4.3 The ratio of DEE formation rate to ethene formation rate as a function of ethanol partial pressure with different water flow rates (■ 0.05 ml/hr, ○ 0.1 ml/hr, and ▼ 0.2 ml/hr) using 9.7 mg of ZrO_2 at 573 K.

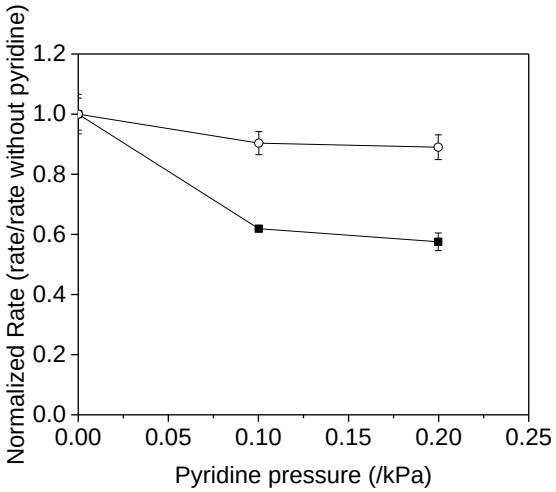

Figure 4.4 Normalized rates (rate with pyridine/rate without pyridine) of (○) ethene and (■) DEE for ethanol dehydration at 573 K on 308.8 mg of ZrO_2 as a function of pyridine partial pressure with 2.2 kPa of ethanol and 1.0 kPa of water partial pressure. The solid lines are meant to guide the eye.

4.3.4. Characterization of sites for ethanol dehydration on zirconia

Reaction rates of ethanol dehydration on ZrO_2 (~10^{-7} mol g_{cat}^{-1} s^{-1}) are two orders of magnitude lower than rates on γ-Al_2O_3 (~10^{-5} mol g_{cat}^{-1} s^{-1}). This is much lower than the difference in surface area of two materials, 81 m^2 g^{-1} for ZrO_2 and 141 m^2 g^{-1} for γ-Al_2O_3. The lower reaction rate suggests that either there are fewer active sites for ethanol dehydration on ZrO_2 or that these sites catalyze dehydration rates at a lower rate than on γ-Al_2O_3. As shown in Figure 4.4, pyridine did not inhibit the parallel ethanol dehydration reactions on ZrO_2 as much as that on γ-Al_2O_3 (normalized rates at 0.1 kPa of pyridine partial pressure were ~0.15 for ethene and ~0.4 for DEE at 573 K with ~10 mg of γ-Al_2O_3)[12]. Less pyridine inhibition indicates that ZrO_2 has weaker acid sites than γ-Al_2O_3. Simultaneous thermogravimetric analysis and temperature programmed desorption (TPD-TGA) experiments performed with 1-propanol in the temperature range 300-800 K on ZrO_2 gave a higher alkene formation activation energy (171 kJ mol^{-1}) calculated using the Redhead equation than on γ-Al_2O_3 (141 kJ mol^{-1})[17,33]. The authors calculated barriers of propene formation from 1-propanol through an E2 mechanism on ZrO_2 and γ-Al_2O_3 clusters using DFT with B3LYP functional and observed the same trend as the TPD-TGA experiments. This also indicates weaker acidity of ZrO_2 than γ-Al_2O_3. We could not estimate the number of sites of ethene formation on ZrO_2 from in-situ titration because pyridine inhibition of ethene synthesis rates resulted in rate differences before and after pyridine introduction into the influent that were hard to quantify. Chokkaram and Davis measured the conversion of 2-octanol on t-ZrO_2 at 593 K and reported that the addition of

0.5 and 5wt% of pyridine to 2-octanol reactant stream did not change the conversion of 2-octanol[105]. They concluded that the site responsible for 2-octanol dehydration on t-ZrO_2 is not strong Lewis or Brønsted acid sites. FT-IR studies of the ZrO_2 surface and of ammonia and pyridine adsorbed on ZrO_2 and calorimetric studies of uptake of ammonia and pyridine showed the existence of Lewis and Brønsted acid sites and their evolution according to the temperature[26,103,106,108–110,114,115,125,126]. Our study allows us to postulate that weak acid sites are relevant to the ethanol dehydration reaction on ZrO_2.

Pyridine inhibits DEE formation more than ethene formation on ZrO_2, a trend opposite to what we observed on Al_2O_3, suggesting that the sites on ZrO_2 are distinct from those on Al_2O_3. ZrO_2 catalyst shows higher selectivity to ethene ($\frac{r_{ethene}}{r_{ethene}+2r_{DEE}}$) at 573 K with 2.2 kPa of ethanol and 1.1 kPa of water partial pressure than γ-Al_2O_3, which has the highest selectivity to ethene among α, γ, and η-Al_2O_3 (50% for ZrO_2 and 30% for γ-Al_2O_3). This also supports the different site identity between zirconia and alumina materials. Turek et al.[127] observed that di-isopropyl ether is not produced from 2-propanol conversion on 2 g of ZrO_2 at 480 and 500 K unlike γ-Al_2O_3. They calculated the average distance between Al^{3+} ions on the surface (2.907 Å) and Zr^{4+} ions on the surface (4.053 Å for t-ZrO_2 and 3.638 Å for m-ZrO_2) and concluded that intermolecular dehydration of 2-propanol could not happen on ZrO_2 because of the distance between neighboring Lewis acidic metal atoms. 1-octene is the main product of the conversion of 2-octanol on ZrO_2 while a mixture of 1-octene and cis-2-octene is produced on γ-Al_2O_3[128]. The authors suggested that the basicity of the oxygen anion on ZrO_2, whose cation radii is larger than 0.7 Å, led to the production

of 1-octene while steric effects for 2-octanol reactions result in the production of cis-2-octene on γ-Al_2O_3, which has a smaller cation radius. Only the IR spectra of alumina at 300 K has frequencies for bridging OH (3724 and 3684 cm^{-1}) and hydrogen-bonded OH groups (3582 cm^{-1}) while no such bands appear in the spectra of zirconia[108]. In the same study, the IR spectra of adsorbed pyridine on alumina at 300 K shows stronger interaction with Lewis acid sites (1622 cm^{-1}) than zirconia (1602 cm^{-1}) as inferred from the higher frequency of the IR band characterizing the interaction of pyridine with Lewis acid sites on alumina compared to that on zirconia.

In independent experiments, no inhibition by CO_2 for ethanol dehydration was noted suggesting that basic sites on ZrO_2 were either not involved in the catalysis or were not inhibited by CO_2 at these conditions. IR studies of CO_2 adsorbed on ZrO_2 and calorimetry studies of uptake of CO_2 shows the existence of basic sites on ZrO_2 [102,103,106,109–111,113–115,126]. We infer that basic sites on the ZrO_2 catalyst can be protonated under water existence, leaving only weak basic sites.

4.4. Conclusion

We emphasize here the necessity of surface characterization under reaction environments to study the properties of catalyst for specific reaction by investigation of kinetics, mechanisms, and site characterization of zirconia materials using ethanol dehydration as probe reaction. We report that ethanol dehydration reactions on ZrO_2 show same kinetics and mechanism involving multimers at 548-623 K. We suggest evolution of surface sites under reaction environments inferred from the kinetic and equilibrium

parameters of rate expressions at 548-623 K. We propose site diversity of ZrO_2 as noted previously for alumina materials from the non-linear relationship between the ratio of DEE to ethene formation rates as a function of ethanol pressure and from in-situ chemical titration using pyridine.

4.5. Acknowledgements

We appreciate financial support from The Dow Chemical Company. We also acknowledge Dr. Mark Bachrach for synthesizing zirconia materials and Dr. Hsu Chiang for helpful technical discussions.

5. Kinetics and mechanisms of ethanol dehydration on chlorine-doped alumina formulations

5.1. Introduction

Thermal stability, high surface area, and tunable acid-base properties make gamma-alumina (γ-Al_2O_3) a versatile catalyst[5,9,10]. The surface properties of γ-Al_2O_3 can be modified by surface dopants such as halogen atoms[129]. The absorption of halogen atoms such as chlorine or fluorine on the surface of γ-Al_2O_3 alters the surface acidity of γ-Al_2O_3 and these formulations are used industrially in reforming, isomerization, cracking, and alkylation reactions[20,129–137]. The chlorination of γ-Al_2O_3 is done by thermal treatment of γ-Al_2O_3 with chlorine sources such as HCl, $AlCl_3$, Cl_2, CCl_4, and $CHCl_3$[131,138–143]. A comparison of infrared (IR) spectra of chlorinated γ-Al_2O_3 (Cl/γ-Al_2O_3) and unchlorinated γ-Al_2O_3 showed that the bands over 3700 cm^{-1} corresponding to basic surface hydroxyl groups disappeared, suggesting that chlorine atoms substitute surface hydroxyl groups and basic hydroxyl groups are more labile[20,129,131,138,139,141,144–146]. IR spectra of pyridine adsorbed on γ-Al_2O_3 and Cl/γ-Al_2O_3 showed bands for pyridine coordinated to Lewis acid sites (~1618 cm^{-1} and ~1455 cm^{-1}) and a shift to higher frequency on Cl/γ-Al_2O_3 compared to the unchlorinated sample suggesting that stronger Lewis acid sites exist on the Cl/γ-Al_2O_3 sample[138,139]. An IR band corresponding to protonated pyridinium species is observed on the Cl/γ-Al_2O_3 sample suggesting the existence of Brønsted acid sites[20,138,139]. Guillaume and co-workers[140] recorded ^{31}P magic angle spinning (MAS) nuclear magnetic

resonance (NMR) spectra of trimethylphosphine (TMP) adsorbed on γ-Al_2O_3 and 1.1wt% Cl/γ-Al_2O_3 relative to the H_3PO_4 reference and quantified the amount of TMP adsorbed on Brønsted acid sites from the peak at -5 ppm and Lewis acid sites from the area of the peaks at -50, 20-30, and 50-70 ppm. The authors changed evacuation temperature (298-623 K) after TMP adsorption in an effort to quantify acid sites of varying strength and noted that chlorination of γ-Al_2O_3 increases the number of strong Brønsted (0.01 to 0.03 sites nm^{-2}) and Lewis acid sites (0.06 to 0.19 sites nm^{-2}) and reduces the number of weak Lewis acid sites (0.45 to 0.29 sites nm^{-2}). Digne et al.[20] calculated surface energies of Cl/γ-Al_2O_3 under different reaction environments – the pressure of water (0.001 and 1 bar), the pressure of hydrochloric acid (10^{-6} to 1000 bar), and temperature (400-1000 K) – using density functional theory (DFT) using the PW 91 functional. They concluded that surface hydroxyl group and surface chlorine atom densities decrease from fully covered to an empty surface as temperature increases and that chlorine atoms persist on the surface only under high pressure of HCl (>10 bar) to give the lowest surface energy. The density of surface chlorine atoms increases as water pressure decreases. These observations strongly suggest that the surface properties of Cl/γ-Al_2O_3 depend on the temperature and presence of hydroxyl- and chlorine-containing species in the gas environment.

In this study, we characterize the surface of Cl/γ-Al_2O_3 using ethanol dehydration as a probe reaction and compare and contrast the rate and selectivity of parallel dehydration pathways on unchlorinated and chlorinated samples to infer the mechanistic and kinetic effects induced by chlorination. We report a diversity of sites on Cl/γ-Al_2O_3 similar to that noted previously for γ-Al_2O_3[11,12,43,58,92]. We also report that the addition of chlorine

increases the activity of γ-Al_2O_3 for ethanol dehydration and that the effects of Cl-addition are saturated at a Cl-loading of ~2wt%.

5.2. Materials and methods

5.2.1. Catalyst preparation and characterization

The Cl/γ-Al_2O_3 material used in this study was synthesized using $AlCl_3$ as a chlorine source and following a procedure reported by Melchor et al[139]. Briefly, γ-Al_2O_3 powder (Sasol Catalox 18 HPA-150, BET surface area 141 m^2 g^{-1}, pore volume 0.790 cm^3 g^{-1}) in a packed bed quartz tube reactor was treated with a stream of air (1.7 cm^3 s^{-1} at NTP conditions, Minneapolis Oxygen) at 723 K for 4 h and cooled to ambient temperature. The reactor was flushed with helium (1.7 cm^3 s^{-1} at NTP conditions, Minneapolis Oxygen) and subsequently it was isolated in a fashion so as to prevent exposure to air or moisture. The reactor was transferred into a glovebox filled with argon. $AlCl_3$ (Anhydrous, 99.999% trace metal basis, Acros Organics; 9 mg to 306.9 mg of γ-Al_2O_3 for 2wt% Cl/γ-Al_2O_3 and 40.7 mg to 304.8 mg of γ-Al_2O_3 for 11wt% Cl/γ-Al_2O_3) was added to the reactor contents and mixed. The reactor was retrieved from the glovebox and the reactor contents were thermally treated under helium (1.7 cm^3 s^{-1} at NTP conditions) at 393 K (the temperature was ramped from ambient to 393 K over a period of one hour and the temperature was held at 393 K for 3 h); subsequently the temperature was ramped to 573 K over a duration of two hours and held at 573 K for a duration of three hours. The reactor contents were cooled down to ambient temperature and the synthesized Cl/γ-Al_2O_3 was stored in the glovebox.

About 0.7 g of acid-washed quartz sand loaded in a packed bed quartz tube reactor was treated in a stream of air (1.7 cm^3 s^{-1} at NTP conditions) at 723 K for 4 h and cooled down to reaction temperature. The reactor was flushed with helium (1.7 cm^3 s^{-1} at NTP conditions) and transferred into the glovebox. About 15 mg of the synthesized Cl/γ-Al_2O_3 was transferred into the reactor with the acid-washed quartz sand (~0.7 g) and the contents were mixed. The catalyst bed comprising the Cl/γ-Al_2O_3 (~15 mg) and the acid-washed quartz sand (~0.7 g) was treated with a stream of helium (1.7 cm^3 s^{-1} at NTP conditions) at 723 K for 4 h and cooled down to the reaction temperature, 488 K. The catalyst bed for γ-Al_2O_3 was prepared by mixing ~0.7 g of sand and ~ 15 mg of γ-Al_2O_3 outside the glovebox and thermally treating this mixture with a stream of air (1.7 cm^3 s^{-1} at NTP conditions) at 723 K and cooling the sample to 488 K.

5.2.2. Steady-state kinetic measurements of ethanol dehydration

The formation rates of ethene and DEE were measured at different ethanol partial pressures (0.84-23 kPa) at ethanol chemical conversion ranging from 3 to 24% to study the kinetics of mono- and di-ethanol dehydration on γ-Al_2O_3 and Cl/γ-Al_2O_3. A tube furnace (National Electric Furnace FA120 type) and a Watlow temperature controller (96 series) were used to maintain the reaction temperature, 488 K, while measuring reactor temperature with a type K thermocouple located on the external surface of the reactor. Liquid ethanol (Decon Labs, Inc., 0.84-23 kPa) was fed and vaporized into a stream of helium (3.4 cm^3 s^{-1} at NTP conditions) and an internal standard mixture for gas chromatographic (GC) analysis comprising Ar/CH_4 (10.0% CH_4 and Ar balance, 0.15 cm^3

s^{-1} at NTP conditions, Matheson Trigas). Liquids were fed using an infusion syringe pump (KDS100). Resistively heated gas lines keeping temperatures above 343 K were employed to avoid condensation of liquids.

An online GC (Agilent 6890 N, flame ionization detector with Agilent Plot-Q column) was used to analyze the reactor effluent. Reported error bars in figures below represent 95% confidence intervals using successive GC injections under the same experimental conditions.

5.2.3. Estimation of parameters

Bayesian statistical estimation techniques in the Athena Visual Studio (v14.2, W.E. Steward and M. Caracotsios) were used to optimize kinetic parameters. The represented uncertainties were the 95% marginal highest posterior density intervals. The experimental conditions under the same ethanol pressure were defined as replicates.

5.3. Results and Discussion

5.3.1. Kinetics and mechanism of ethanol dehydration on chlorinated gamma-alumina

The synthesis rate of ethene decreases when ethanol pressure increases at 488 K on γ-Al_2O_3 and Cl/γ-Al_2O_3, as shown in Figure 5.1 (ethanol partial pressure in the range 0.8-23 kPa). Computational chemistry studies suggest that ethanol monomers on the surface undergo E2-type elimination during the rate limiting step for ethene formation - the cleavage of C_β-H bond[17,33,34,86,87]. The negative dependence of ethene formation rates on ethanol partial pressure suggest that ethanol dimers inhibit mono-alcohol dehydration and

that ethanol monomers and dimers are the dominating surface species. The rate expression shown in Equation 5.1 accurately describes the ethanol pressure dependence of ethene formation rates and is the same equation as we report in our previous study for mono-alcohol dehydration on γ-Al_2O_3[11,43] for the special case of water pressure being zero or negligible compared to ethanol pressure.

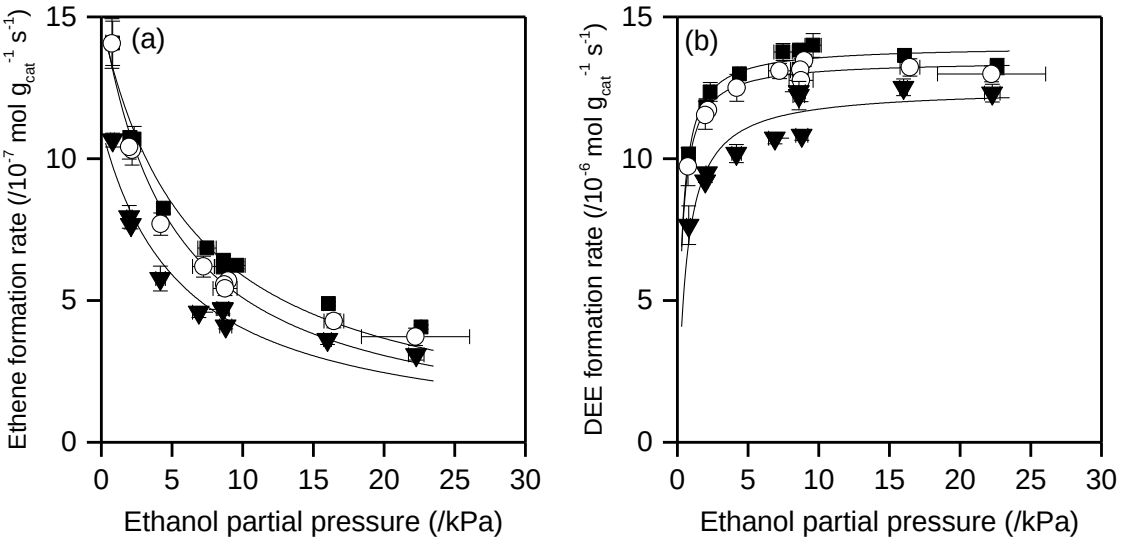

Figure 5.1 (a) Ethene and (b) DEE formation rate for ethanol dehydration at 488K on 11wt% Cl/γ-Al_2O_3 (■), 2wt% Cl/γ-Al_2O_3 (○), and γ-Al_2O_3 (▼) as a function of ethanol partial pressure (total gas flowrate = 3.4 cm^3 s^{-1}). The solid line represents the model fits to Equation 5.1 and 5.2 for (a) and (b), respectively.

$$r_{ethene} = \frac{k_{ethene} P_{alcohol}}{P_{alcohol} + \frac{K_{A2}}{K_{A1}} P_{alcohol}^2} \quad (5.1)$$

k_{ethene} in Equation 5.1 is the rate constant of the rate limiting step and K_{A1} and K_{A2} are equilibrium constants for adsorption of alcohol monomers and alcohol dimers, respectively, on the surface of γ-Al_2O_3 and Cl/γ-Al_2O_3. Kinetic and equilibrium constants

in Equation 5.1 were estimated using Bayesian statistical estimation techniques in the Athena Visual Studio (v14.2, W. E. Stewart and M. Caracotsios) and are tabulated in Table 5.1.

Table 5.1 Estimated kinetic parameters for mono-alcohol dehydration of ethanol on γ-Al_2O_3, 2wt% Cl/γ-Al_2O_3, and 11wt% Cl/γ-Al_2O_3 at 488 K using the model presented in Equation 5.1 and data from Figure 5.1

Parameter	$k_{C_2H_4}$(/10^{-6} mol_{C2H4} g_{cat}^{-1} s^{-1})			$\frac{K_{A2}}{K_{A1}}$		
Estimated Value	γ-Al_2O_3	2wt% Cl/γ-Al_2O_3	11wt% Cl/γ-Al_2O_3	γ-Al_2O_3	2wt% Cl/γ-Al_2O_3	11wt% Cl/γ-Al_2O_3
	1.11 ± 0.08	1.52 ± 0.08	1.48 ± 0.07	0.18 ± 0.03	0.20 ± 0.03	0.15 ± 0.02

DEE formation rates increase with ethanol pressure increases at 488 K on γ-Al_2O_3 and Cl/γ-Al_2O_3, as shown in Figure 5.1 (ethanol partial pressure in the range 0.8-23 kPa). The involvement of ethanol dimer surface species in the rate determining step via an S_N2-type mechanism is assumed based on reports in the computational chemistry literature[17,33,34,86,87]. The positive dependence of DEE synthesis rates on ethanol pressure at low ethanol pressure suggests the existence of ethanol monomers on the surface. A rate expression describing the observed pressure dependence of DEE formation rates on ethanol partial pressure is shown in Equation 5.2. This equation is identical to one we have previously reported for di-alcohol dehydration pathways on γ-Al_2O_3 except that the denominator term corresponding to water-derived mono- and multimeric species is omitted because of water pressures being low throughout the catalyst bed relative to the ethanol pressure.[11,43].

$$r_{DEE} = \frac{k_{DEE} P_{alcohol}^2}{P_{alcohol}^2 + \frac{K_{A1}}{K_{A2}} P_{alcohol}} \quad (5.2)$$

k_{DEE} in Equation 5.2 is the rate constant of the rate limiting step and K_{A1} and K_{A2} are equilibrium constants for adsorption of alcohol monomers and alcohol dimers, respectively, on the surface of γ-Al_2O_3 and Cl/γ-Al_2O_3. Kinetic and equilibrium constants in Equation 5.2 were estimated using Bayesian statistical estimation techniques in the Athena Visual Studio (v14.2, W. E. Stewart and M. Caracotsios) and are tabulated in Table 5.2.

Table 5.2 Estimated kinetic parameters for di-alcohol dehydration of ethanol on γ-Al_2O_3, 2wt% Cl/γ-Al_2O_3, and 11wt% Cl/γ-Al_2O_3 at 488 K using the model presented in Equation 5.2 and data from Figure 5.1

Parameter	k_{DEE}(/10^{-5} mol_{DEE} g_{cat}^{-1} s^{-1})			$\frac{K_{A1}}{K_{A2}}$		
Estimated Value	γ-Al_2O_3	2wt% Cl/γ-Al_2O_3	11wt% Cl/γ-Al_2O_3	γ-Al_2O_3	2wt% Cl/γ-Al_2O_3	11wt% Cl/γ-Al_2O_3
	1.25 ± 0.04	1.35 ± 0.01	1.40 ± 0.02	0.62 ± 0.13	0.30 ± 0.03	0.31 ± 0.04

The rate expressions for mono- and di-alcohol dehydration are identical for γ-Al_2O_3, 2wt% Cl/γ-Al_2O_3, and 11wt% Cl/γ-Al_2O_3. The dominating surface species do not change in the presence of chlorine on the surface. The reaction rates increase as the chlorine content increases but the difference between 2wt% and 11wt% Cl/γ-Al_2O_3 is insignificant. Reaction rate constants were evaluated from a parametric fit of the experimental data to the rate expressions shown in Equations 5.1 and 5.2. The rate constants for mono- and di-

alcohol dehydration show the same trend with Cl-loading as the reaction rate (Tables 5.1 and 5.2). These observations suggest that chlorine atoms on the surface enhance the reactivity of γ-Al_2O_3 without changing the dominant adsorbed species and that the effects of Cl-addition are saturated at a loading of ~ 2wt%. Digne et al.[20] synthesized 0.85, 1.14, and 1.43wt% Cl/γ-Al_2O_3 using HCl as the chlorine source and compared the IR spectra of Cl-loaded samples with that of γ-Al_2O_3. The bands located at 3794 and 3775 cm^{-1}, corresponding to basic hydroxyl groups, disappeared when chlorine was introduced. The bands in the 3700-3600 cm^{-1} region ascribed to acidic hydroxyl groups were broadened as the chlorine content increased. The authors proposed that chlorine atoms substitute basic hydroxyl groups while acidic hydroxyl groups remain and that chlorine adatoms weaken the hydrogen-bonding network among hydroxyl groups. The authors calculated the pyridine adsorption energy on acidic surface hydroxyl groups of γ-Al_2O_3 and Cl/γ-Al_2O_3 using DFT to be -15 kJ mol^{-1} for γ-Al_2O_3 and -50 kJ mol^{-1} for Cl/γ-Al_2O_3. They suggest that weakened hydrogen bonding makes the proton of hydroxyl groups more accessible and reactive. The IR spectra of 0.85, 1.14, and 1.43wt% Cl/γ-Al_2O_3 were similar indicating that the surface of γ-Al_2O_3 is saturated at Cl-loadings as low as 0.85wt%, which supports our observation that rates for ethanol dehydration are invariant at Cl-loadings in excess of 2 wt%. Melchor et al.[139] synthesized Cl/γ-Al_2O_3 using CCl_4 and $AlCl_3$ as chlorine sources. Pyridine was adsorbed on γ-Al_2O_3 and Cl/γ-Al_2O_3 materials at room temperature and desorption was performed under vacuum at temperatures from 423 to 923 K while IR and gravimetric studies were used for structural and chemical characterization. The authors noted that the intensity of the 1455 cm^{-1} band ascribed to pyridine adsorbed at Lewis acid

sites and the amount of desorbed pyridine followed Beer's law. The total number of Lewis acid sites and the number of strong Lewis acid sites were deduced from the intensity of the 1455 cm^{-1} band after desorption at 423 and 623 K, respectively. Both Cl/γ-Al_2O_3 materials showed an increase in the total number of Lewis acid sites and the number of strong acid sites compared to γ-Al_2O_3 – 0.6 and 0.27 sites per nm^{-2} for γ-Al_2O_3, 1.5 and 0.6 sites per nm^{-2} for Cl/γ-Al_2O_3 synthesized using CCl_4, and 1.23 and 1.04 sites per nm^{-2} for Cl/γ-Al_2O_3 synthesized using $AlCl_3$. The increase in the number of strong Lewis acid sites upon the addition of chlorine was higher than the increase in the total number of Lewis acid sites. Cl/γ-Al_2O_3 materials were also noted to catalyze butane isomerization reactions at lower temperatures (563 K) than γ-Al_2O_3 (659 K). These observations led the authors to conclude that the strength of Lewis acidity also increased upon chlorine-doping. The increase in ethanol dehydration rates upon the addition of Cl leads us to posit that the Cl/γ-Al_2O_3 material may have stronger Lewis acid sites than γ-Al_2O_3 under alcohol dehydration reaction conditions. The number of sites for dehydration can be estimated using in-situ pyridine titration however, the ~30% increase in reaction rate on Cl/γ-Al_2O_3 may not result in a discernable change in the number of sites measured using chemical titration.

5.3.2. Site heterogeneity on chlorinated gamma-alumina

The relative ratio of di-ethanol to mono-ethanol dehydration rates from kinetic studies on γ-Al_2O_3 and Cl/γ-Al_2O_3 evidences the site heterogeneity of these materials. This ratio does not show a linear relationship with ethanol partial pressure (Figure 5.2). If the two parallel reactions were to occur on the same sites ($\frac{r_{ether}}{r_{olefin}} =$

$\frac{k_{ether}P_{alcohol}^2}{Common\ terms}/\frac{k_{olefin}P_{alcohol}}{Common\ terms} = \frac{k_{ether}}{k_{olefin}}P_{alcohol}$), the ratio of DEE to ethene synthesis rates of ethanol dehydration should show a linear relationship. The curvature observed when plotting the ratio of DEE to ethene synthesis rates against the ethanol pressure (Figure 5.2) leads us to postulate that these parallel reactions occur on distinct sites although the same dominant surface species exist on the distinct sites.

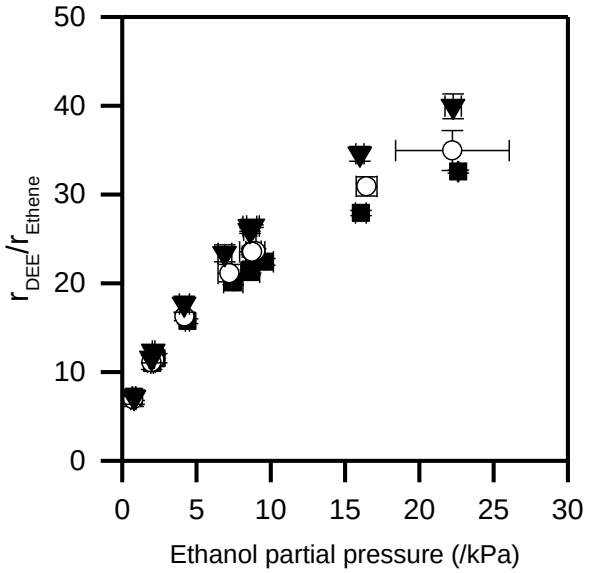

Figure 5.2 The ratio of DEE formation rate to ethene formation rate as a function of ethanol partial pressure using ~15 mg of 11wt% Cl/γ-Al_2O_3 (■), 2wt% Cl/γ-Al_2O_3 (○), and γ-Al_2O_3 (▼) at 488K.

5.4. Conclusion

We demonstrate that the chlorination of γ-Al_2O_3 increases the strength of Lewis acid sites present on the alumina sample under ethanol dehydration reaction environments. No change in catalytic properties is evident at loadings in excess of 2wt% chlorine loadings

suggesting that the surface of γ-Al_2O_3 is saturated at these loadings under ethanol dehydration reaction conditions. We postulate that the diversity of sites previously evidenced for parallel dehydration reactions on unchlorinated γ-Al_2O_3 samples is likely prevalent on Cl/γ-Al_2O_3 samples as well.

5.5. Acknowledgements

We appreciate financial support from The Dow Chemical Company. We also acknowledge Dr. Hsu Chiang for helpful technical discussions.

6. Conclusion and recommendation

In this research, I investigated kinetics, mechanisms, and site requirements of alcohol dehydration reactions on metal oxide catalysts – alumina polymorphs (alpha, gamma, and eta), zirconia, and chlorinated alumina – with the objective of comparing and contrasting the functional reactivity of these materials with reported results from structural and chemical characterization that highlight the distinct metal coordination and hydroxylation environments in these materials. The rate expressions and proposed reaction mechanisms of parallel alcohol dehydration pathways including the inhibition by surface multimer species were common to all metal oxides studied in this research. Kinetic studies and chemical titration experiments reveal the distinct site requirements for the two parallel dehydration reactions. The in-situ titration protocols developed in this research do not reveal the exact surface structure of the active site however, these methods provide a more exact upper bound for the number of active sites under reaction conditions compared to experiments done in absence of the reactants.

Olefin selectivity increased with alkyl chain length and increasing substitution on the alpha carbon. We also note that higher reaction temperatures result in higher olefin selectivity. Zirconia shows higher olefin selectivity (~50%) but a lower reaction rate (~10^{-7} mol g_{cat}^{-1} s^{-1} at 573 K) compared to amorphous alumina materials (~30% and ~10^{-5} mol g_{cat}^{-1} s^{-1} at 573 K for gamma alumina) at identical reaction conditions. The kinetic and mechanistic studies in this work elucidate that alcohol dehydration on γ-alumina at high reaction temperatures (>673 K) and nearly complete chemical conversion would achieve

the selective conversion of alcohols to olefins because secondary pathways decompose the ether product to olefins under these reaction conditions.

My research also demonstrates that the presence of water in the reactant stream leads to a change in the functional reactivity of alumina materials – likely due to a change in the hydroxylation state of aluminum. Water also inhibits dehydration reactions by competitive adsorption with the alcohol reactant. These concepts are broadly applicable to other oxide materials and to other molecules containing hydroxyl-groups.

In summary, my work has elucidated the diversity of surface sites and the evolution of these active centers under reaction conditions on a class of acidic and amphoteric oxide materials. The characterization methods used in this research including probe molecule reactions and chemical titration represent a protocol for the functional characterization of the reactivity of amorphous materials and will likely have methodological impact in this area.

Bibliography

1 H. Kung, *Stud. Surf. Sci. Catal.*, 1989, **47**.

2 M. Breysse, J. L. Portefaix and M. Vrinat, *Catal. Today*, 1991, **10**, 489–505.

3 M. B. Gawande, R. K. Pandey and R. V. Jayaram, *Catal. Sci. Technol.*, 2012, **2**, 1113.

4 B. Grzybowska-Swierkosz, *Mater. Chem. Phys.*, 1987, **17**, 121–144.

5 I. Chorkendorff and J. W. Niemantsverdriet, *Catalyst Supports: Alumina*, Wiley-VCH, Weinheim, Germany, 2007.

6 H. Hattori, *Chem. Rev.*, 1995, **95**, 537–558.

7 Y. Ono, *J. Catal.*, 2003, **216**, 406–415.

8 A. G. Panov and J. J. Fripiat, *J. Catal.*, 1998, **178**, 188–197.

9 J. E. Kogel, N. C. Trivedi, J. M. Barker and S. T. Krukowsk, Eds., *Industrial Minerals & Rocks*, Society for Mining, Metallurgy, and Exploration, Englewood, CO, USA, 7th edn., 2006.

10 G. Busca, *Adv. Catal.*, 2014, **57**, 319–404.

11 M. Kang, J. F. DeWilde and A. Bhan, *ACS Catal.*, 2015, **5**, 602–612.

12 M. Kang and A. Bhan, *Catal. Sci. Technol.*, 2016, **6**, 6667–6678.

13 S. D. Jackson and J. S. J. Hargreaves, Eds., *Metal Oxide Catalysis*, Wiley-VCH, Weinheim, Germany, 2009.

14 N. Guo, S. Caratzoulas, D. J. Doren, S. I. Sandler and D. G. Vlachos, *Energy Environ. Sci.*, 2012, **5**, 6703–6716.

15 G. Huber, S. Iborra and A. Corma, *Chem. Rev.*, 2006, **106**, 4044–4098.

16 R. J. J. Nel and A. de Klerk, *Ind. Eng. Chem. Res.*, 2009, **48**, 5230–5238.

17 P. Kostestkyy, J. Yu, R. J. Gorte and G. Mpourmpakis, *Catal. Sci. Technol.*, 2014, **4**, 3861–3869.

18 M. Digne, P. Sautet, P. Raybaud, P. Euzen and H. Toulhoat, *J. Catal.*, 2002, **211**, 1–5.

19 M. Digne, P. Sautet, P. Raybaud, P. Euzen and H. Toulhoat, *J. Catal.*, 2004, **226**, 54–68.

20 M. Digne, P. Raybaud, P. Sautet, D. Guillaume and H. Toulhoat, *J. Am. Chem. Soc.*, 2008, **130**, 11030–11039.

21 H. Knözinger, *Angew. Chem. Int. Ed.*, 1968, **7**, 791–805.

22 H. Knözinger, H. Bühl and K. Kochloefl, *J. Catal.*, 1972, **68**, 57–68.

23 B. H. Davis, *J. Org. Chem.*, 1972, **37**, 1240–1244.

24 B. H. Davis and W. S. Brey, *J. Catal.*, 1972, **25**, 81–92.

25 B. H. Davis, *J. Catal.*, 1978, **52**, 176–185.

26 J. T. Kozlowski and R. J. Davis, *J. Energy Chem.*, 2013, **22**, 58–64.

27 B. H. Davis and P. Ganesan, *Ind. Eng. Chem. Process Des. Dev.*, 1979, **18**, 191–198.

28 B. H. Davis, *J. Catal.*, 1983, **79**, 58–69.

29 B. C. Lippens and J. H. de Boer, *Acta Cryst.*, 1964, **17**, 1312–1321.

30 S. Golay, R. Doepper and A. Renken, *Chem. Eng. Sci.*, 1999, **54**, 4469–4474.

31 E. Parry, *J. Catal.*, 1963, **379**, 371–379.

32 J. Ripmeester, *J. Am. Chem. Soc.*, 1983, **105**, 2925–2927.

33 S. Roy, G. Mpourmpakis, D. Hong, D. Vlachos, A. Bhan and R. Gorte, *ACS Catal.*, 2012, **2**, 1846–1853.

34 M. A. Christiansen, G. Mpourmpakis and D. G. Vlachos, *ACS Catal.*, 2013, **3**, 1965–1975.

35 H. Knözinger and P. Ratnasamy, *Catal. Rev. Sci. Eng.*, 1978, **17**, 31–70.

36 H. A. Dabbagh, M. Zamani and B. H. Davis, *J. Mol. Catal. A Chem.*, 2010, **333**, 54–68.

37 R. Wischert, P. Laurent, C. Copéret, F. Delbecq and P. Sautet, *J. Am. Chem. Soc.*, 2012, **134**, 14430–14449.

38 J. H. Kwak, D. Mei, C. H. F. Peden, R. Rousseau and J. Szanyi, *Catal. Letters*, 2011, **141**, 649–655.

39 S. Golay, R. Doepper and A. Renken, *Appl. Catal. A Gen.*, 1998, **172**, 97–106.

40 S. Cai and K. Sohlberg, *J. Mol. Catal. A Chem.*, 2003, **193**, 157–164.

41 J. H. Kwak, R. Rousseau, D. Mei, C. H. F. Peden and J. Szanyi, *ChemCatChem*, 2011, **3**, 1557–1561.

42 H. Knözinger and A. Scheglila, *J. Catal.*, 1970, **17**, 252–263.

43 J. F. DeWilde, H. Chiang, D. A. Hickman, C. R. Ho and A. Bhan, *ACS Catal.*, 2013, **3**, 798–807.

44 B. Shi and B. Davis, *J. Catal.*, 1995, **157**, 359–367.

45 H. Knözinger, H. Bühl and E. Ress, *J. Catal.*, 1968, **12**, 121–128.

46 B. Shi, H. Dabbagh and B. Davis, *Top. Catal.*, 2002, **18**, 259–264.

47 H. Pines and W. Haag, *J. Am. Chem. Soc.*, 1961, **83**, 2847–2852.

48 J. Macht, M. J. Janik, M. Neurock and E. Iglesia, *Angew. Chem. Int. Ed.*, 2007, **46**, 7864–78688.

49 R. G. Greenler, *J. Chem. Phys.*, 1962, **37**, 2094–2100.

50 A. Gabrienko, S. Arzumanov, A. Toktarev and A. Stepanov, *J. Phys. Chem. C*, 2012, **116**, 21430–21438.

51 M. Rep, A. E. Palomares, G. Eder-Mirth, J. G. van Ommen, N. Rösch and J. A. Lercher, *J. Phys. Chem. B*, 2000, **104**, 8624–8630.

52 R. Schenkel, A. Jentys, S. F. Parker and J. A. Lercher, *J. Phys. Chem. B*, 2004, **108**, 15013–15026.

53 C. Wang, P. Bai, J. I. Siepmann and A. E. Clark, *J. Phys. Chem. C*, 2014, **118**, 19723–19732.

54 J. Jain and C. Pillai, *J. Catal.*, 1967, **9**, 322–330.

55 J. Bedard, H. Chiang and A. Bhan, *J. Catal.*, 2012, **290**, 210–219.

56 H. Chiang and A. Bhan, *J. Catal.*, 2010, **271**, 251–261.

57 K. L. Joshi, G. Psofogiannakis, A. C. T. van Duin and S. Raman, *Phys. Chem. Chem. Phys.*, 2014, **16**, 18433–18441.

58 J. F. DeWilde, C. J. Czopinski and A. Bhan, *ACS Catal.*, 2014, **4**, 4425–4433.

59 Y. K. Kim, B. D. Kay, J. M. White and Z. Dohnálek, *Catal. Letters*, 2007, **119**, 1–4.

60 P. B. Venuto and P. S. Landis, *Adv. Catal.*, 1968, **18**, 259–371.

61 P. Clayborne, T. Nelson and T. DeVore, *Appl. Catal. A Gen.*, 2004, **257**, 225–233.

62 I. Levin and D. Brandon, *J. Am. Ceram. Soc.*, 1998, **81**, 1995–2012.

63 P. S. Santos, H. S. Santos and S. P. Toledo, *Mater. Res.*, 2000, **3**, 104–114.

64 Y. Sakashita, Y. Araki and H. Shimada, *Appl. Catal. A Gen.*, 2001, **215**, 101–110.

65 L. Marchese, S. Bordiga, S. Coluccia, G. Martra and A. Zecchina, *J. Chem. Soc. Faraday Trans.*, 1993, **89**, 3483–3489.

66 L. Kovarik, M. Bowden, A. Genc, J. Szanyi, C. H. F. Peden and J. H. Kwak, *J. Phys. Chem. C*, 2014, **118**, 18051–18058.

67 L. Kovarik, M. Bowden, D. Shi, N. M. Washton, A. Andersen, J. Z. Hu, J. Lee, J. Szanyi, J. H. Kwak and C. H. F. Peden, *Chem. Mater.*, 2015, **27**, 7042–7049.

68 L. Kovarik, A. Genc, C. Wang, A. Qiu, C. H. F. Peden, J. Szanyi and J. H. Kwak, *J. Phys. Chem. C*, 2013, **117**, 179–186.

69 R.-S. Zhou and R. L. Snyder, *Acta Cryst. B*, 1991, **47**, 617–630.

70 C. Pecharromán, I. Sobrados, J. E. Iglesias, T. González-Carreño and J. Sanz, *J. Phys. Chem. B*, 1999, **103**, 6160–6170.

71 C. S. John, N. C. M. Alma and G. R. Hays, *Appl. Catal.*, 1983, **6**, 341–346.

72 H. Stolz and H. Knözinger, *Kolloid-Zeitschrift und Zeitschrift für Polym.*, 1971, **243**, 71–76.

73 C. Morterra, A. Zecchina, S. Coluccia and A. Chiorino, *J. Chem. Soc. Faraday Trans. 1*, 1977, **73**, 1544–1560.

74 E. N. Gribov, O. Zavorotynska, G. Agostini, J. G. Vitillo, G. Ricchiarde, G. Spoto and A. Zecchina, *Phys. Chem. Chem. Phys.*, 2010, **12**, 6474–6482.

75 J. H. Kwak, J. Z. Hu, D. H. Kim, J. Szanyi and C. H. F. Peden, *J. Catal.*, 2007, **251**,

189–194.

76 T. K. Phung, C. Herrera, M. Á. Larrubia, M. García-Diéguez, E. Finocchio, L. J. Alemany and G. Busca, *Appl. Catal. A Gen.*, 2014, **483**, 41–51.

77 B. A. Hendriksen, D. R. Pearce and R. Rudham, *J. Catal.*, 1972, **24**, 82–87.

78 J. H. Kwak, C. H. F. Peden and J. Szanyi, *J. Phys. Chem. C*, 2011, **115**, 12575–12579.

79 L. de Mourgues, F. Peyron, Y. Trambouze and M. Prettre, *J. Catal.*, 1967, **125**, 117–125.

80 J. H. de Boer, R. B. Fahim, B. G. Linsen, W. J. Visseren and W. F. N. M. de Vleesschauwer, *J. Catal.*, 1967, **7**, 163–172.

81 C. R. Narayanan, S. Srinivasan, A. K. Datye, R. Gorte and A. Biaglow, *J. Catal.*, 1992, **138**, 659–674.

82 T. K. Phung, A. Lagazzo, M. Á. Rivero Crespo, V. Sánchez Escribano and G. Busca, *J. Catal.*, 2014, **311**, 102–113.

83 T. K. Phung and G. Busca, *Chem. Eng. J.*, 2015, **272**, 92–101.

84 T. K. Phung, L. Proietti Hernández, A. Lagazzo and G. Busca, *Appl. Catal. A Gen.*, 2015, **493**, 77–89.

85 Z. Fang, Y. Wang and D. A. Dixon, *J. Phys. Chem. C*, 2015, **119**, 23413–23421.

86 G. R. Jenness, M. A. Christiansen, S. Caratzoulas, D. G. Vlachos and R. J. Gorte, *J. Phys. Chem. C*, 2014, **118**, 12899–12907.

87 M. A. Christiansen, G. Mpourmpakis and D. G. Vlachos, *J. Catal.*, 2015, **323**, 121–131.

88 P. Kostestkyy and G. Mpourmpakis, *Catal. Sci. Technol.*, 2015, **5**, 4547–4555.

89 P. Kostestkyy, J. P. Maheswari and G. Mpourmpakis, *J. Phys. Chem. C*, 2015, **119**, 16139–16147.

90 D. M. Sung, Y. H. Kim, E. D. Park and J. E. Yie, *Res. Chem. Intermed.*, 2010, **36**, 653–660.

91 H.-N. Chiang, S. Nachimuthu, Y.-C. Cheng, N. P. Damayanti and J.-C. Jiang, *Appl. Surf. Sci.*, 2016, **363**, 636–643.

92 J. F. DeWilde and A. Bhan, *Appl. Catal. A Gen.*, 2015, **502**, 361–369.

93 B. D. Flockhart, J. A. N. Scott and R. C. Pink, *Trans. Faraday Soc.*, 1966, **62**, 730–740.

94 J. M. McHale, A. Auroux, J. Perrota and A. Navrotsky, *Science*, 1997, **277**, 788–791.

95 Z. Zhang and T. J. Pinnavaia, *Angew. Chem. Int. Ed.*, 2008, **47**, 7501–7504.

96 D. S. Maciver, H. H. Tobin and R. T. Barth, *J. Catal.*, 1963, **2**, 485–497.

97 K. Larmier, C. Chizallet, N. Cadran, S. Maury, J. Abboud, A. F. Lamic-Humblot, E. Marceau and H. Lauron-Pernot, *ACS Catal.*, 2015, **5**, 4423–4437.

98 K. Larmier, A. Nicolle, C. Chizallet, N. Cadran, S. Maury, A.-F. Lamic-Humblot, E. Marceau and H. Lauron-Pernot, *ACS Catal.*, 2016, **6**, 1905–1920.

99 Z. Li, Z. Fang, M. S. Kelley, B. D. Kay, R. Rousseau, Z. Dohnalek and D. A. Dixon, *J. Phys. Chem. C*, 2014, **118**, 4869–4877.

100 R. Rousseau, D. A. Dixon, B. D. Kay and Z. Dohnálek, *Chem. Soc. Rev.*, 2014, **43**, 7664–7680.

101 J. Z. Hu, S. Xu, J. H. Kwak, M. Y. Hu, C. Wan, Z. Zhao, J. Szanyi, X. Bao, X. Han, Y. Wang and C. H. F. Peden, *J. Catal.*, 2016, **336**, 85–93.

102 K. Tanabe and T. Yamaguchi, *Catal. Today*, 1994, **20**, 185–198.

103 T. Yamaguchi, *Catal. Today*, 1994, **20**, 199–217.

104 A. Auroux, P. Artizzu, I. Ferino, V. Solinas, G. Leofanti, M. Padovan, G. Messina and R. Mansani, *J. Chem. Soc. Faraday Trans.*, 1995, **91**, 3263–3267.

105 S. Chokkaram and B. H. Davis, *J. Mol. Catal. A Chem.*, 1997, **118**, 89–99.

106 Y. Nakano, T. Iizuka, H. Hattori and K. Tanabe, *J. Catal.*, 1979, **57**, 1–10.

107 M. Yoshimura, *Am. Ceram. Soc. Bull.*, 1988, 67.

108 M. I. Zaki, M. a. Hasan, F. a. Al-Sagheer and L. Pasupulety, *Colloids Surfaces A Physicochem. Eng. Asp.*, 2001, **190**, 261–274.

109 W. Hertl, *Langmuir*, 1989, **5**, 96–100.

110 M. Bensitel, O. Saur, J. C. Lavalley and G. Mabilon, *Mater. Chem. Phys.*, 1987, **17**, 249–258.

111 J. Kondo, H. Abe, Y. Sakata, K.-I. Maruya, K. Domen and T. Onishi, *J. Chem. Soc. Faraday Trans. 1 Phys. Chem. Condens. Phases*, 1988, **84**, 511–519.

112 V. Bolis, C. Morterra, M. Volante, L. Orio and B. Fubini, *Langrnuir*, 1990, **6**, 695–701.

113 M. Bensitel, V. Moraver, J. Lamotte, O. Saur and J.-C. Lavalley, *Spectrochim. Acta Part A Mol. Spectrosc.*, 1987, **43**, 1487–1491.

114 V. Bolis, G. Magnacca, G. Cerrato and C. Morterra, *Top. Catal.*, 2002, **19**, 259–269.

115 V. Solinas, E. Rombi, I. Ferino, M. G. Cutrufello, G. Colón and J. A. Navío, *J. Mol.*

Catal. A Chem., 2003, **204**–**205**, 629–635.

116 W. Piskorz, J. Gryboś, F. Zasada, S. Cristol, J. F. Paul, A. Adamski and Z. Sojka, *J. Phys. Chem. C*, 2011, **115**, 24274–24286.

117 W. Piskorz, J. Gryboś, F. Zasada, P. Zapała, S. Cristol, J. F. Paul and Z. Sojka, *J. Phys. Chem. C*, 2012, **116**, 19307–19320.

118 E. Iglesia, D. G. Barton, J. A. Biscardi, M. J. L. Gines and S. L. Soled, *Catal. Today*, 1997, **38**, 339–360.

119 H. Metiu, S. Chrétien, Z. Hu, B. Li and X. Sun, *J. Phys. Chem. C*, 2012, **116**, 10439–10450.

120 H. A. Dabbagh and M. Zamani, *Appl. Catal. A Gen.*, 2011, **404**, 141–148.

121 Y.-S. Hsu, Y.-L. Wang and A.-N. Ko, *J. Chinese Chem. Soc.*, 2009, **56**, 314–322.

122 M. Rezaei, S. M. Alavi, S. Sahebdelfar and Z. F. Yan, *Powder Technol.*, 2006, **168**, 59–63.

123 T. Yamaguchi, H. Sasaki and K. Tanabe, *Chem. Lett.*, 1973, **2**, 1017–1018.

124 A. Auroux, P. Artizzu, I. Ferino, V. Solinas, G. Leofanti, M. Padovan, G. Messina and R. Mansani, *J. Chem. Soc. Faraday Trans.*, 1995, **91**, 3263–3267.

125 K. Tanabe, *Mater. Chem. Phys.*, 1985, **13**, 347–364.

126 M. G. Cutrufello, I. Ferino, R. Monaci, E. Rombi and V. Solinas, *Top. Catal.*, 2002, **19**, 225–240.

127 W. Turek, J. Haber and A. Krowiak, *Appl. Surf. Sci.*, 2005, **252**, 823–827.

128 H. A. Dabbagh, C. G. Hughes and B. H. Davis, *J. Catal.*, 1992, **133**, 445–460.

129 H. Vigué, P. Quintard, T. Merle-Méjean and V. Lorenzelli, *J. Eur. Ceram. Soc.*,

1998, **18**, 305–309.

130 G. Clet, J. M. Goupil, G. Szabo and D. Cornet, *J. Mol. Catal. A Chem.*, 1999, **148**, 253–264.

131 D. Guillaume, S. Gautier, F. Alario and J. M. Devès, *Oil Gas Sci. Technol.*, 1999, **54**, 537–545.

132 Y. Ono, *Catal. Today*, 2003, **81**, 3–16.

133 D. Cornet, J. Goupil, G. Szabo, J. Poirier and G. Clet, *Appl. Catal. A Gen.*, 1996, **141**, 193–205.

134 P. Bernard and M. Primet, *J. Chem. Soc. Faraday Trans.*, 1990, **86**, 567–570.

135 E. Garbowski, J.-P. Candy and M. Primet, *J. Chem. Soc., Faraday Trans. 1*, 1983, **79**, 835–844.

136 I. Coleto, R. Roldán, C. Jiménez-Sanchidrián, J. P. Gómez and F. J. Romero-Salguero, *Fuel*, 2007, **86**, 1000–1007.

137 F. J. Gracia, J. T. Miller, A. J. Kropf and E. E. Wolf, *J. Catal.*, 2002, **209**, 341–354.

138 A. Ayame, G. Sawada, H. Sato, G. Zhang, T. Ohta and T. Izumizawa, *Appl. Catal.*, 1989, **48**, 25–35.

139 A. Melchor, E. Garbowski, M.-V. Mathieu and M. Primet, *J. Chem. Soc., Faraday Trans. 1*, 1986, **82**, 1893–1901.

140 D. Guillaume, S. Gautier, I. Despujol, F. Alario and P. Beccat, *Catal. Letters*, 1997, **43**, 213–218.

141 A. Krzywicki and M. Marczewski, *J. Chem. Soc. Faraday Trans. 1 Phys. Chem. Condens. Phases*, 1980, **76**, 1311–1322.

142 A. Krzywicki, M. Marczewski, R. Modzelewski, K. Pelszik and S. Malinowski, *React. Kinet. Catal. Lett.*, 1980, **13**, 1–6.

143 J. Thomson, G. Webb and J. M. Winield, *J. Mol. Catal.*, 1991, **67**, 117–126.

144 T. A. Gordymova and A. A. Davydov, *React. Kinet. Catal. Lett.*, 1983, **23**, 233–238.

145 M. Tanaka and S. Ogasawara, *J. Catal.*, 1970, **16**, 157–163.

146 A. R. McInroy, D. T. Lundie, J. M. Winfield, C. C. Dudman, P. Jones, S. F. Parker and D. Lennon, *Catal. Today*, 2006, **114**, 403–411.

Appendix A

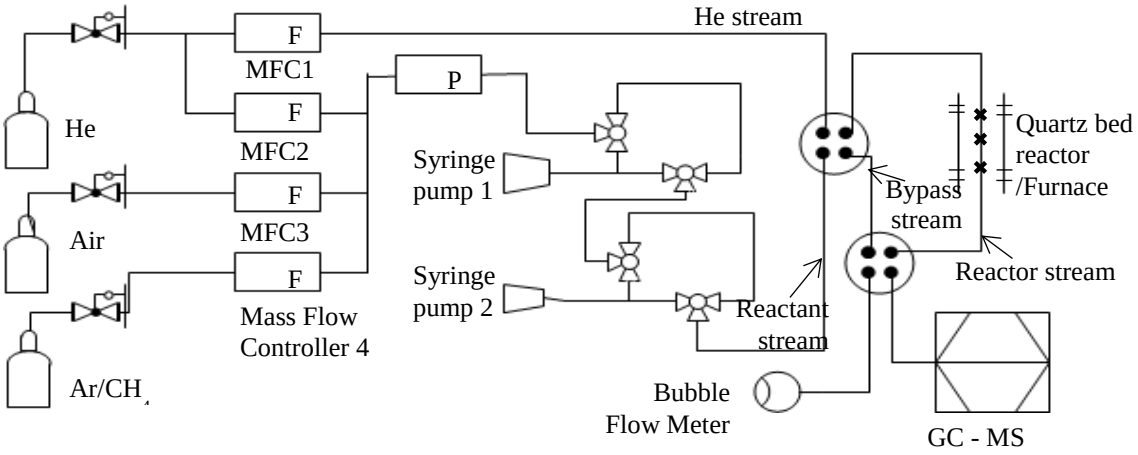

Scheme A. 1 Scheme of the reactor system used in the catalytic experiments